NASA/CR—2002-211909

Efficient Reformulation of the Thermoelastic Higher-Order Theory for FGMs

Yogesh Bansal and Marek-Jerzy Pindera
University of Virginia, Charlottesville, Virginia

November 2002

The NASA STI Program Office . . . in Profile

Since its founding, NASA has been dedicated to the advancement of aeronautics and space science. The NASA Scientific and Technical Information (STI) Program Office plays a key part in helping NASA maintain this important role.

The NASA STI Program Office is operated by Langley Research Center, the Lead Center for NASA's scientific and technical information. The NASA STI Program Office provides access to the NASA STI Database, the largest collection of aeronautical and space science STI in the world. The Program Office is also NASA's institutional mechanism for disseminating the results of its research and development activities. These results are published by NASA in the NASA STI Report Series, which includes the following report types:

- TECHNICAL PUBLICATION. Reports of completed research or a major significant phase of research that present the results of NASA programs and include extensive data or theoretical analysis. Includes compilations of significant scientific and technical data and information deemed to be of continuing reference value. NASA's counterpart of peer-reviewed formal professional papers but has less stringent limitations on manuscript length and extent of graphic presentations.

- TECHNICAL MEMORANDUM. Scientific and technical findings that are preliminary or of specialized interest, e.g., quick release reports, working papers, and bibliographies that contain minimal annotation. Does not contain extensive analysis.

- CONTRACTOR REPORT. Scientific and technical findings by NASA-sponsored contractors and grantees.

- CONFERENCE PUBLICATION. Collected papers from scientific and technical conferences, symposia, seminars, or other meetings sponsored or cosponsored by NASA.

- SPECIAL PUBLICATION. Scientific, technical, or historical information from NASA programs, projects, and missions, often concerned with subjects having substantial public interest.

- TECHNICAL TRANSLATION. English-language translations of foreign scientific and technical material pertinent to NASA's mission.

Specialized services that complement the STI Program Office's diverse offerings include creating custom thesauri, building customized databases, organizing and publishing research results . . . even providing videos.

For more information about the NASA STI Program Office, see the following:

- Access the NASA STI Program Home Page at ***http://www.sti.nasa.gov***

- E-mail your question via the Internet to help@sti.nasa.gov

- Fax your question to the NASA Access Help Desk at 301–621–0134

- Telephone the NASA Access Help Desk at 301–621–0390

- Write to:
  NASA Access Help Desk
  NASA Center for AeroSpace Information
  7121 Standard Drive
  Hanover, MD 21076

NASA/CR—2002-211909

Efficient Reformulation of the Thermoelastic Higher-Order Theory for FGMs

Yogesh Bansal and Marek-Jerzy Pindera
University of Virginia, Charlottesville, Virginia

Prepared under Grant NAG3–2524

National Aeronautics and
Space Administration

Glenn Research Center

November 2002

Acknowledgments

This research was conducted under funding through the NASA Glenn Grant NAG3–2524. The NASA technical monitor for this project was Dr. Steven M. Arnold whose support and encouragement for the undertaken investigation the authors gratefully acknowledge.

Available from

NASA Center for Aerospace Information
7121 Standard Drive
Hanover, MD 21076

National Technical Information Service
5285 Port Royal Road
Springfield, VA 22100

Available electronically at http://gltrs.grc.nasa.gov

Efficient Reformulation of the Thermoelastic Higher-Order Theory for FGMs

Yogesh Bansal and Marek-Jerzy Pindera
University of Virginia
Charlottesville, Virginia 22903

Abstract

Functionally graded materials (FGMs) are characterized by spatially variable microstructures which are introduced to satisfy given performance requirements. The microstructural gradation gives rise to continuously or discretely changing material properties which complicate FGM analysis. Various techniques have been developed during the past several decades for analyzing traditional composites and many of these have been adapted for the analysis of FGMs. Most of the available techniques use the so-called uncoupled approach in order to analyze graded structures. These techniques ignore the effect of microstructural gradation by employing specific spatial material property variations that are either assumed or obtained by local homogenization. The higher-order theory for functionally graded materials (HOTFGM) is a coupled approach developed by Aboudi et al. (1999) which takes the effect of microstructural gradation into consideration and does not ignore the local-global interaction of the spatially variable inclusion phase(s). Despite its demonstrated utility, however, the original formulation of the higher-order theory is computationally intensive. Herein, an efficient reformulation of the original higher-order theory for two-dimensional elastic problems is developed and validated. The use of the local-global conductivity and local-global stiffness matrix approach is made in order to reduce the number of equations involved. In this approach, surface-averaged quantities are the primary variables which replace volume-averaged quantities employed in the original formulation. The reformulation decreases the size of the global conductivity and stiffness matrices by approximately sixty percent. Various thermal, mechanical, and combined thermomechanical problems are analyzed in order to validate the accuracy of the reformulated theory through comparison with analytical and finite-element solutions. The presented results illustrate the efficiency of the reformulation and its advantages in analyzing functionally graded materials.

1 Introduction

Functionally graded materials (FGMs) are a new generation of composites wherein the microstructural details are spatially varied through nonuniform distribution of the reinforcement phase(s), by using reinforcement with different properties, sizes and shapes, as well as by interchanging the roles of reinforcement and matrix phases in a continuous manner. The result is a microstructure that produces continuously changing thermal and mechanical properties at the macroscopic or continuum level. This new concept of engineering the material's microstructure marks a new paradigm in both the materials science and mechanics of materials areas since it allows to fully integrate both the material and structural considerations into the final design of structural components.

Although the area of FGMs is not very old, an enormous amount of research has already taken place and the field continues to expand rapidly. Many papers on different aspects of FGMs have been published in the past decade in regular journals, special issues of journals devoted to FGMs, conference proceedings, and monographs, cf. Pindera et al. (1994a, 1995a, 1997a), Needleman and Suresh (1996), IIschner and Cherradi (1994), Shiota and Miyamoto (1997), and Suresh and Mortensen (1998). Therefore, a comprehensive review of the different research activities is outside the scope of this report. In keeping with the focus of the undertaken study, an overview is provided below of the different approaches employed to model the thermomechanical response of FGMs.

The analysis of functionally graded materials is a difficult task because of the arbitrary variation of material microstructure. In order to analyze the response of functionally graded materials under given loading conditions, two distinct approaches have been used to date. The first is the uncoupled micro-macrostructural approach. In this approach, FGMs are analyzed directly at the continuum level, which allows to reduce a given boundary value problem to a system of differential equations with variable coefficients. These variable coefficients represent macroscopic material property variations expressed as functions of position that are obtained by local homogenization of the microstructure or sometimes taken to have specific functional forms. In some cases, the material properties are assumed to be piecewise uniform through appropriate microstructural discretization, and then the governing differential equations are solved for each layer subject to interfacial continuity and boundary conditions.

There are various micromechanical models that have been used for homogenizing the microstructure of functionally graded materials. These micromechanical models include Voigt and Reuss estimates, Mori-Tanaka method, Composite Cylinder Assemblage (CCA) model, Method of Cells, etc., and have been described in detail by Aboudi (1991). The uncoupled analysis of functionally graded materials involves the determination of effective (macroscopic) properties at a continuum point based on the chosen micromechanics model, a step called local homogenization, which are then used in the overall analysis of the structure to determine the macroscopic field quantities. This two-step procedure essentially neglects the interaction between non-uniformly distributed inclusions and decouples the locally produced effects of microstructural variation. This can often lead to potentially erroneous results, especially when the size of the inclusion phase is large with respect to the overall dimensions of the composite, the field gradients are high, or when the number of inclusions is small. Hence, these models can only be used in limited circumstances such as when the size of the inclusion phase is very small in comparison to the overall size of the analyzed structural component and the total number of inclusions is large, Pindera et al. (1995).

Using the uncoupled approach, various researchers have developed different analytical techniques for studying particular types of problems in functionally graded materials. In general, these techniques include either a specific type of loading, a specific geometry or specific variation of material properties. The type of problems studied involve thermal barrier coating and joint problems, crack problems, and design and optimization problems. Representative papers in these areas are discussed below.

One of the most important applications of functionally graded materials is in the field of thermal barrier coatings. Internal stresses can be reduced and fracture toughness enhanced with appropriate spatial variation of ceramic and metallic phases. Approaches employed to study temperature fields and resulting stresses in thermal barrier coatings depend on whether elastic or inelastic analyses are conducted, as discussed recently in an extensive review paper by Noda (1999). In the case of inelastic effects, approaches range from one-dimensional finite-difference analyses, Kokini and Choules (1995), to two-dimensional or axisymmetric finite-element analyses based on layer-wise discretization of the coating's microstructure with piece-wise varying properties, Jian et al. (1995), Delfosse et al. (1997). The properties of the individual layers are typically obtained using either simple

rule-of-mixtures or Mori-Tanaka estimates. In the absence of inelastic effects, analytical techniques and their numerical implementations have been employed with the property variation described by continuous functions. For instance, Jeon et al. (1997) discuss an axisymmetric thermoelastic solution for an inhomogeneous material by introducing a thermoelastic displacement potential function. Sutradhar et al. (2001) use the Green's function approach in a boundary element setting in order to study the 3-D transient heat conduction in functionally graded materials with exponential thermal conductivity variation.

Analysis of graded joints has also received considerable attention due to the large interlaminar stresses that may arise along a bi-material interface at the free edge. For example, Drake et al. (1993) and Williamson et al. (1993) employed the finite-element method to study the residual stresses that develop at graded ceramic-metal interfaces joining cylindrical bodies made of metallic and ceramic components. The gradation was modeled using a series of perfectly bonded cylindrical layers, with each layer having slightly different properties. The authors' results demonstrated the importance of plasticity effects in the analysis of graded and non-graded interfaces. The authors also showed that, in some cases, optimization of the microstructure of graded layers is required to achieve reduction in certain critical stress components that control interfacial failure. Along similar lines, Suresh et al. (1994) studied the response of elastoplastic bimaterial strips subjected to cyclic temperature variations. The authors showed that plastic flow along the material interface at the free edge can be modified substantially by altering the constraints at the strip edge.

Functionally graded microstructures can be very useful in enhancing material's fracture resistance through the mechanism of crack blunting and crack-path deflection. In fact, the enhanced fracture toughness of graded coatings is due to the local material heterogeneity. In order to keep the problem tractable, local material heterogeneity is replaced by spatially varying homogenized properties, reducing the problem of a crack in an heterogeneous material to an inhomogeneous medium crack problem. Crack problems in inhomogeneous materials have been studied by a number of people since the 1960's. However, systematic studies of this class of crack problems were initiated in the early 1980's by Erdogan and co-workers, cf., Delale and Erdogan (1983), Erdogan (1985), Erdogan et al. (1991), and subsequently extended to functionally graded materials. In applications involving TBCs, different types of cracks may arise, including cracks perpendicular and parallel to the coating's surface and at the free edge between the substrate and the graded or layered coating. These different scenarios have been discussed by Erdogan (1995), Kadioglu and Erdogan (1995), Erdogan and Wu (1996), Schulze and Erdogan (1998), Lee and Erdogan (1998), and Jin and Paulino (2001). Additional solutions to crack problems in the presence of thermal and mechanical loading have been provided by Noda and Jin (1993) who discuss thermal stress intensity factors for a FGM strip using Fourier transforms, showing the efficiency of suitable material selection in reducing these intensity factors. Crack problems in viscoelastic functionally graded materials have recently been addressed by Paulino and Jin (2001).

The ultimate objective in designing a structure for practical applications is not just the ability to analyze a given heterogeneous component, but the identification of an optimum design which produces the best stress distribution for the given application. Various researchers have provided analytical solutions for specific types of problems which are useful in optimizing the design of graded structures. These analytical solutions also serve as benchmark solutions for the validation and verification of finite-element and other approximate techniques which have been developed or are being developed for the analysis of functionally graded materials. For instance, Salzar and Barton (1994) incorporated the analytical solution for the axisymmetric elastoplastic response of a multilayered cylinder, developed by Pindera et al. (1993), into a commercial optimization code to minimize residual stresses in metal-matrix composites using graded interfaces. Horgan and Chan (1998, 1999) developed solutions for problems involving pressurized hollow cylinders, rotating disks,

and bars under torsion with continuously graded isotropic linearly elastic materials. Ootao et al. (1998) discuss the optimization of material gradation for a hollow circular cylinder under thermal loading. They use the concept of a laminated composite cylinder with piece-wise homogenous and uniform material properties together with the neural network approach in order to determine an optimum design. Nadeau and Ferrari (1999) discuss microstructural optimization of a functionally graded transversely isotropic layer. Noda (1999) identifies optimal composition profiles to reduce thermal stresses in FGMs using perturbation methods.

The second approach employed in the analysis of functionally graded materials is the coupled approach. In this approach, the effects of microstructural variation and the interaction between nonuniformly distributed inclusions are explicitly taken into account in the course of solving the governing differential equations. This in turn, makes possible the analysis of heterogeneous materials with different microstructural scales, in contrast to the uncoupled approach which is limited to materials with very fine microstructures.

The higher-order theory for functionally graded materials (HOTFGM) is an approximate coupled approach based on a particular volume discretization of the material's microstructure and an averaging approach in the solution of the governing field equations in each subvolume. This theory has been developed in a sequence of papers dating back to 1993, Aboudi et al. (1993), in order to circumvent the limitations of the uncoupled approach. Summaries of the different stages of the higher-order theory's development have been provided by Pindera et al. (1995b; 1998), and most recently in a comprehensive article by Aboudi et al. (1999). As discussed in this review article, the theory has been employed to analyze a number of technologically important problems ranging from thermally-induced free-edge interlaminar stresses in cross-ply laminates, optimization of fiber spacing in laminates subjected to thermal gradients, and thermal barrier coatings. The focus of these applications was the demonstration of microstructural coupling effects in functionally graded materials as a function of the microstructural length scale, and when these effects can be neglected, as well as the demonstration of the utility of functionally graded microstructures in enhancing the performance of plate-like structural components subjected to through-thickness thermal gradients. Specifically, the higher-order theory has been applied to the following technologically important problems:

- Investigation of the effect of microstructure on thermal and stress fields in MMC plates and cylinders
- Investigation of the use of functionally graded architectures in reducing edge effects in MMC plates
- Optimization of functionally graded microstructures in MMC plates and cylinders
- Development of guidelines for the design of special coatings in exhaust nozzle applications under NASA/Pratt & Whitney Space Act Agreement
- Investigation of microstructural effects in functionally graded TBCs

The results obtained so far have demonstrated that this theory is an accurate, cf. Pindera and Dunn (1997), and easily implementable tool in the analysis and design of FGMs. Furthermore, comparison of the results obtained from the standard micromechanics approach with those of HOTFGM has demonstrated the need for a theory like HOTFGM, which explicitly couples the micro (local) and macro (global) effects in the analysis, Pindera et al. (1994b; 1995c).

The recent developments of HOTFGM include extension to cylindrical ccordinates to enable analysis, design, and optimization of structural components found in aircraft engine applications, Pindera and Aboudi (2000).

1.1 Objectives and Outline of the Completed Investigation

As demonstrated through its applications, the higher-order theory is an accurate and useful approach for the analysis of functionally graded materials which takes the micro-macrostructural coupling into account and does not neglect the effects of microstructural variation. However, the higher-order theory is computationally intensive in those cases which require detailed volume discretization in order to mimic realistic microstructural details in certain types of functionally graded materials or to capture very high thermal and stress gradients. Such detailed modeling leads to a large number of equations whose solution becomes computationally prohibitively expensive and sometimes impossible to execute due to the large computer storage requirements.

This report describes an efficient reformulation of the higher-order theory which leads to a significant reduction in the number of equations required in a problem's solution. This reformulation is accomplished by making use of the so-called local-global conductivity and stiffness matrix approaches employed in conjunction with a simplied manner of volume discretization developed by Zhong and Pindera (2002). The simplified volume discretization provides the basis for the reformulation by enabling the derivation of closed-form relations between surface-average heat fluxes and tractions and the corresponding temperatures and displacements associated with a generic subvolume. Therefore, volume-averaged quantities employed in the original higher-order theory are replaced by surface-averaged quantities as the fundamental unknowns in order to employ the local-global conductivity and stiffness matrix approaches in the reformulation.

The original two-dimensional formulation of HOTFGM is described briefly in Section 2. The motivation for efficient reformulation of the higher-order theory and the reformulation approach are then discussed in Section 3. Section 4 describes the effect of mesh discretization on the field variables for selected loading conditions and also provides validation of the reformulated higher-order theory by considering several test cases, including the classic Eshelby problem of a circular inclusion in an infinite matrix subjected to uniform far-field loading. The results are compared with the analytical solution and a finite-element solution obtained using ANSYS. Section 5 demonstrates the usefulness of the higher-order theory in the analysis of functionally graded materials by considering a thermal barrier coating application. Section 6 summarizes the present accomplishments and provides suggestions for future work which should be pursued in this area.

2 Higher-Order Theory: Original Formulation

The version of the higher-order theory for materials functionally graded in two directions, or HOTFGM-2D, is based on a geometric model of a heterogeneous composite graded in the $x_2 - x_3$ plane which occupies the region $0 \leq x_2 \leq H$, and $0 \leq x_3 \leq L$, Fig. 1. The microstructural pattern is represented by discretizing the cross-section of the heterogeneous composite into N_q and N_r generic cells in the intervals $0 \leq x_2 \leq H$, and $0 \leq x_3 \leq L$, respectively. The indices q and r ($q = 1, 2, ..., N_q$ and $r = 1, 2, ..., N_r$), identify the generic cells in the $x_2 - x_3$ plane. The generic cell (q, r) consists of four subcells designated by $(\beta\gamma)$, where each index β, γ takes a value 1 or 2 which indicates the relative position of the given subcell within the generic cell along the x_2 and x_3 axis, respectively. The thermomechanical properties of the material within a subcell are assumed to be constant. The composite is assumed to be infinite in the x_1 direction, whereas the dimensions of the generic cell along the functionally graded directions x_2 and x_3 are $h_1^{(q)}$, $h_2^{(q)}$, and $l_1^{(r)}$, $l_2^{(r)}$, and can vary arbitrarily such that

$$H = \sum_{q=1}^{N_q} (h_1^{(q)} + h_2^{(q)}) \qquad L = \sum_{r=1}^{N_r} (l_1^{(r)} + l_2^{(r)}) \tag{1}$$

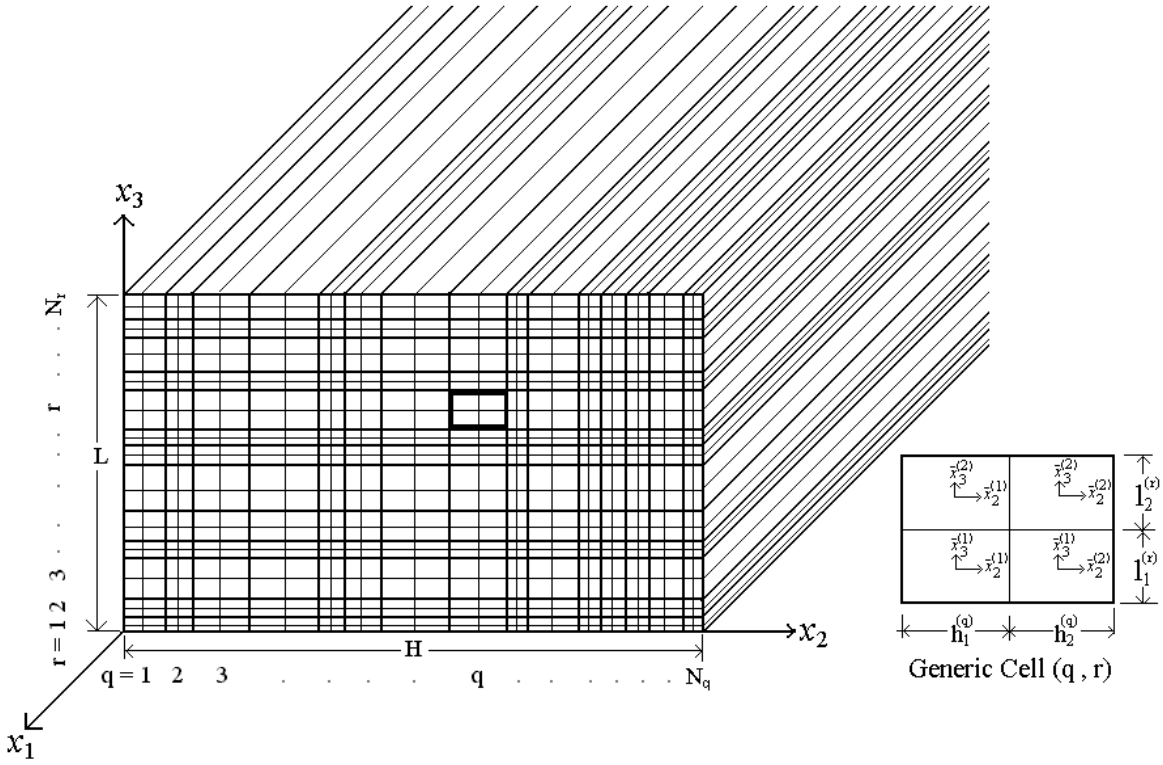

Fig. 1. HOTFGM-2D representation of a composite functionally graded in the x_2 and x_3 directions with uniform microstructure in the x_1 direction.

The composite is subjected to combined thermomechanical loading on its bounding surfaces in the $x_2 - x_3$ plane given in terms of temperature or heat flux, and surface displacements and/or tractions. Further, the strain $\bar{\varepsilon}_{11}$ ($\bar{\varepsilon}_{11} = 0$, for plane strain) is uniform in the x_1 direction. Given the applied thermomechanical loading, an approximate solution for the temperature and displacement fields is constructed. The solution strategy involves volumetric averaging of the field equations together with the imposition of boundary and continuity conditions in an average sense between the sub-volumes used to characterize the material's microstructure. As described in Subsections 2.1 and 2.2, the temperature and in-plane displacement fields in each subcell of a generic cell are approximated using a quadratic expansion in the local coordinates $\bar{x}_2^{(\beta)}$, $\bar{x}_3^{(\gamma)}$ placed at the subcell's centroid. This temperature and displacement field representation is sufficient to capture the local effects created by the thermomechanical field gradients and the microstructure of the graded material with finite dimensions in the functionally graded directions.

2.1 Thermal Analysis

The thermal boundary conditions specified in terms of temperature or heat flux distribution on the bounding surface in the $x_2 - x_3$ plane are assumed to be steady-state. The temperature distribution in the subcell $(\beta\gamma)$ of the $(q,r)^{th}$ generic cell measured with respect to a reference temperature T_{ref}, is denoted by $T^{(\beta\gamma)}$. This temperature field is approximated by a second-order expansion in the local coordinates $\bar{x}_2^{(\beta)}$, $\bar{x}_3^{(\gamma)}$ as follows:

$$T^{(\beta\gamma)} = T_{(00)}^{(\beta\gamma)} + \bar{x}_2^{(\beta)} T_{(10)}^{(\beta\gamma)} + \bar{x}_3^{(\gamma)} T_{(01)}^{(\beta\gamma)} + \frac{1}{2}(3\bar{x}_2^{(\beta)2} - \frac{h_\beta^{(q)2}}{4}) T_{(20)}^{(\beta\gamma)} + \frac{1}{2}(3\bar{x}_3^{(\gamma)2} - \frac{l_\gamma^{(r)2}}{4}) T_{(02)}^{(\beta\gamma)} \qquad (2)$$

where $T^{(\beta\gamma)}_{(00)}$ is the volume-averaged temperature in the subcell $(\beta\gamma)$, and $T^{(\beta\gamma)}_{(mn)}$ $(m, n = 0, 1,$ or 2 with $m + n \leqq 2)$ are the higher-order coefficients which provide a better approximation of the temperature field throughout the subcell.

For a generic cell with four subcells containing arbitrarily specified materials, five unknowns (i.e., $T^{(\beta\gamma)}_{(00)}$, ..., $T^{(\beta\gamma)}_{(02)}$) are associated with each subcell, producing twenty unknowns for each generic cell. This results in $20N_qN_r$ unknown quantities for a composite with N_r rows and N_q columns of generic cells. These unknowns are determined by first satisfying the zeroth, first and second moment of the heat conduction equation in each subcell in volumetric sense. Subsequently, continuity of heat flux and temperature is imposed in an average sense at the interfaces separating adjacent subcells, as well as neighboring cells, followed by the boundary conditions.

2.1.1 Heat conduction equation

Under steady-state thermal boundary conditions in the $x_2 - x_3$ plane, the heat flux field in the material occupying the subcell $(\beta\gamma)$ of the $(q, r)^{th}$ generic cell, in the region $\left|\bar{x}_2^{(\beta)}\right| \leq \frac{1}{2}h_\beta^{(q)}$, $\left|\bar{x}_3^{(\gamma)}\right| \leq \frac{1}{2}l_\gamma^{(r)}$, must satisfy the steady-state heat conduction equation given by

$$\frac{\partial q_2^{(\beta\gamma)}}{\partial \bar{x}_2^{(\beta)}} + \frac{\partial q_3^{(\beta\gamma)}}{\partial \bar{x}_3^{(\gamma)}} = 0, \ (\beta, \gamma = 1, 2) \tag{3}$$

The heat flux components $q_i^{(\beta\gamma)}$ at any point passing through a subcell $(\beta\gamma)$ are derived from the temperature field according to the Fourier's law of heat conduction given by

$$q_i^{(\beta\gamma)} = -k_i^{(\beta\gamma)} \frac{\partial T^{(\beta\gamma)}}{\partial \bar{x}_i^{(\cdot)}}, \ (i = 2, 3; \ no \ sum) \tag{4}$$

where $k_i^{(\beta\gamma)}$ are the heat conductivity coefficients of the material in the subcell $(\beta\gamma)$ assumed to be orthotropic, and no summation is implied by repeated Greek letters in the above and henceforth.

In order to satisfy the above steady-state heat conduction equation in a volumetric sense, the following volume-averaged quantities are defined in the higher-order theory

$$Q^{(\beta\gamma)}_{i(m,n)} = \frac{1}{A^{(q,r)}_{(\beta\gamma)}} \int_{-h_\beta^{(q)}/2}^{h_\beta^{(q)}/2} \int_{-l_\gamma^{(r)}/2}^{l_\gamma^{(r)}/2} (\bar{x}_2^{(\beta)})^m (\bar{x}_3^{(\gamma)})^n q_i^{(\beta\gamma)} d\bar{x}_2^{(\beta)} d\bar{x}_3^{(\gamma)} \tag{5}$$

where $A^{(q,r)}_{(\beta\gamma)} = h_\beta^{(q)} l_\gamma^{(r)}$ is the area of the subcell $(\beta\gamma)$ in the $(q, r)^{th}$ generic cell. $Q^{(\beta\gamma)}_{i(0,0)}$ is the average value of the heat flux component $q_i^{(\beta\gamma)}$ in the subcell $(\beta\gamma)$, whereas for the other values of m and n Eq. (5) defines higher-order heat fluxes. Satisfaction of the heat conduction equation given by Eq. (3) results in the following four conditions in terms of the volume-averaged flux quantities

$$\left[Q^{(\beta\gamma)}_{2(1,0)}/h_\beta^2 + Q^{(\beta\gamma)}_{3(0,1)}/l_\gamma^2 \right]^{(q,r)} = 0 \tag{6}$$

Equation (6) can be expressed in terms of the coefficients $T^{(\beta\gamma)}_{(mn)}$ by evaluating the flux quantities defined in Eq. (5). Substituting Eq. (4) into Eq. (5), and performing the required volume integration yields the following non-vanishing zeroth-order and first-order heat fluxes in terms of

the coefficients $T^{(\beta\gamma)}_{(mn)}$

$$Q^{(\beta\gamma)}_{2(0,0)} = -k^{(\beta\gamma)}_2 T^{(\beta\gamma)}_{(10)} \tag{7}$$

$$Q^{(\beta\gamma)}_{2(1,0)} = -k^{(\beta\gamma)}_2 \frac{h^{(q)2}_\beta}{4} T^{(\beta\gamma)}_{(20)} \tag{8}$$

$$Q^{(\beta\gamma)}_{3(0,0)} = -k^{(\beta\gamma)}_3 T^{(\beta\gamma)}_{(01)} \tag{9}$$

$$Q^{(\beta\gamma)}_{3(0,1)} = -k^{(\beta\gamma)}_3 \frac{l^{(r)2}_\gamma}{4} T^{(\beta\gamma)}_{(02)} \tag{10}$$

2.1.2 Heat flux continuity conditions

The heat flux continuity at the interfaces separating adjacent subcells within the generic cell (q, r) is imposed in an integral sense as follows

$$\frac{1}{l^{(r)}_\gamma}\int_{-l^{(r)}_\gamma/2}^{l^{(r)}_\gamma/2}\left[q^{(1\gamma)}_2(\frac{h^{(q)}_1}{2},\bar{x}^{(\gamma)}_3)\right]^{(q,r)} d\bar{x}^{(\gamma)}_3 = \frac{1}{l^{(r)}_\gamma}\int_{-l^{(r)}_\gamma/2}^{l^{(r)}_\gamma/2}\left[q^{(2\gamma)}_2(-\frac{h^{(q)}_2}{2},\bar{x}^{(\gamma)}_3)\right]^{(q,r)} d\bar{x}^{(\gamma)}_3 \tag{11}$$

$$\frac{1}{h^{(q)}_\beta}\int_{-h^{(q)}_\beta/2}^{h^{(q)}_\beta/2}\left[q^{(\beta1)}_3(\bar{x}^{(\beta)}_2,\frac{l^{(r)}_1}{2})\right]^{(q,r)} d\bar{x}^{(\beta)}_2 = \frac{1}{h^{(q)}_\beta}\int_{-h^{(q)}_\beta/2}^{h^{(q)}_\beta/2}\left[q^{(\beta2)}_3(\bar{x}^{(\beta)}_2,-\frac{l^{(r)}_2}{2})\right]^{(q,r)} d\bar{x}^{(\beta)}_2 \tag{12}$$

Similarly, the heat flux continuity at the interfaces between generic cells is satisfied in an integral sense by requiring that

$$\frac{1}{l^{(r)}_\gamma}\int_{-l^{(r)}_\gamma/2}^{l^{(r)}_\gamma/2}\left[q^{(1\gamma)}_2(-\frac{h^{(q+1)}_1}{2},\bar{x}^{(\gamma)}_3)\right]^{(q+1,r)} d\bar{x}^{(\gamma)}_3 = \frac{1}{l^{(r)}_\gamma}\int_{-l^{(r)}_\gamma/2}^{l^{(r)}_\gamma/2}\left[q^{(2\gamma)}_2(\frac{h^{(q)}_2}{2},\bar{x}^{(\gamma)}_3)\right]^{(q,r)} d\bar{x}^{(\gamma)}_3 \tag{13}$$

$$\frac{1}{h^{(q)}_\beta}\int_{-h^{(q)}_\beta/2}^{h^{(q)}_\beta/2}\left[q^{(\beta1)}_3(\bar{x}^{(\beta)}_2,-\frac{l^{(r+1)}_1}{2})\right]^{(q,r+1)} d\bar{x}^{(\beta)}_2 = \frac{1}{h^{(q)}_\beta}\int_{-h^{(q)}_\beta/2}^{h^{(q)}_\beta/2}\left[q^{(\beta2)}_3(\bar{x}^{(\beta)}_2,\frac{l^{(r)}_2}{2})\right]^{(q,r)} d\bar{x}^{(\beta)}_2 \tag{14}$$

Satisfaction of the above heat flux continuity conditions $(11)-(14)$ results in the following eight equations in terms of the volume-averaged flux quantities

$$\left[-12Q^{(1\gamma)}_{2(1,0)}/h_1 + Q^{(2\gamma)}_{2(0,0)} - 6Q^{(2\gamma)}_{2(1,0)}/h_2\right]^{(q,r)} - \left[Q^{(2\gamma)}_{2(0,0)} + 6Q^{(2\gamma)}_{2(1,0)}/h_2\right]^{(q-1,r)} = 0 \tag{15}$$

$$\left[-Q^{(1\gamma)}_{2(0,0)} + \frac{1}{2}Q^{(2\gamma)}_{2(0,0)} - 3Q^{(2\gamma)}_{2(1,0)}/h_2\right]^{(q,r)} + \frac{1}{2}\left[Q^{(2\gamma)}_{2(0,0)} + 6Q^{(2\gamma)}_{2(1,0)}/h_2\right]^{(q-1,r)} = 0 \tag{16}$$

$$\left[-12Q^{(\beta1)}_{3(0,1)}/l_1 + Q^{(\beta2)}_{3(0,0)} - 6Q^{(\beta2)}_{3(0,1)}/l_2\right]^{(q,r)} - \left[Q^{(\beta2)}_{3(0,0)} + 6Q^{(\beta2)}_{3(0,1)}/l_2\right]^{(q,r-1)} = 0 \tag{17}$$

$$\left[-Q^{(\beta1)}_{3(0,0)} + \frac{1}{2}Q^{(\beta2)}_{3(0,0)} - 3Q^{(\beta2)}_{3(0,1)}/l_2\right]^{(q,r)} + \frac{1}{2}\left[Q^{(\beta2)}_{3(0,0)} + 6Q^{(\beta2)}_{3(0,1)}/l_2\right]^{(q,r-1)} = 0 \tag{18}$$

Equations (6) and $(15)-(18)$ have been obtained in terms of the volume-averaged flux quantities after some complex algebraic manipulations. For detailed derivation of these equations, refer to Aboudi et al. (1996) . These equations can now be expressed explicitly in terms of the microvariables $T^{(\beta\gamma)}_{(mn)}$ with the use of Eqs. $(7)-(10)$.

2.1.3 Temperature continuity conditions

The temperature continuity at the interfaces separating adjacent subcells within the generic cell (q, r) is imposed in an integral sense as follows

$$\frac{1}{l_\gamma^{(r)}}\int_{-l_\gamma^{(r)}/2}^{l_\gamma^{(r)}/2}\left[T^{(1\gamma)}(\frac{h_1^{(q)}}{2},\bar{x}_3^{(\gamma)})\right]^{(q,r)}d\bar{x}_3^{(\gamma)} = \frac{1}{l_\gamma^{(r)}}\int_{-l_\gamma^{(r)}/2}^{l_\gamma^{(r)}/2}\left[T^{(2\gamma)}(-\frac{h_2^{(q)}}{2},\bar{x}_3^{(\gamma)})\right]^{(q,r)}d\bar{x}_3^{(\gamma)} \tag{19}$$

$$\frac{1}{h_\beta^{(q)}}\int_{-h_\beta^{(q)}/2}^{h_\beta^{(q)}/2}\left[T^{(\beta 1)}(\bar{x}_2^{(\beta)},\frac{l_1^{(r)}}{2})\right]^{(q,r)}d\bar{x}_2^{(\beta)} = \frac{1}{h_\beta^{(q)}}\int_{-h_\beta^{(q)}/2}^{h_\beta^{(q)}/2}\left[T^{(\beta 2)}(\bar{x}_2^{(\beta)},-\frac{l_2^{(r)}}{2})\right]^{(q,r)}d\bar{x}_2^{(\beta)} \tag{20}$$

Similarly, the temperature continuity at the interfaces between generic cells is satisfied in an integral sense by requiring that

$$\frac{1}{l_\gamma^{(r)}}\int_{-l_\gamma^{(r)}/2}^{l_\gamma^{(r)}/2}\left[T^{(1\gamma)}(-\frac{h_1^{(q+1)}}{2},\bar{x}_3^{(\gamma)})\right]^{(q+1,r)}d\bar{x}_3^{(\gamma)} = \frac{1}{l_\gamma^{(r)}}\int_{-l_\gamma^{(r)}/2}^{l_\gamma^{(r)}/2}\left[T^{(2\gamma)}(\frac{h_2^{(q)}}{2},\bar{x}_3^{(\gamma)})\right]^{(q,r)}d\bar{x}_3^{(\gamma)} \tag{21}$$

$$\frac{1}{h_\beta^{(q)}}\int_{-h_\beta^{(q)}/2}^{h_\beta^{(q)}/2}\left[T^{(\beta 1)}(\bar{x}_2^{(\beta)},-\frac{l_1^{(r+1)}}{2})\right]^{(q,r+1)}d\bar{x}_2^{(\beta)} = \frac{1}{h_\beta^{(q)}}\int_{-h_\beta^{(q)}/2}^{h_\beta^{(q)}/2}\left[T^{(\beta 2)}(\bar{x}_2^{(\beta)},\frac{l_2^{(r)}}{2})\right]^{(q,r)}d\bar{x}_2^{(\beta)} \tag{22}$$

Satisfaction of the above thermal continuity conditions results in the following eight equations given explicitly in terms of the microvariables $T_{(mn)}^{(\beta\gamma)}$

$$\left[T_{(00)}^{(1\gamma)}+\frac{1}{2}h_1T_{(10)}^{(1\gamma)}+\frac{1}{4}h_1^2T_{(20)}^{(1\gamma)}\right]^{(q,r)} = \left[T_{(00)}^{(2\gamma)}-\frac{1}{2}h_2T_{(10)}^{(2\gamma)}+\frac{1}{4}h_2^2T_{(20)}^{(2\gamma)}\right]^{(q,r)} \tag{23}$$

$$\left[T_{(00)}^{(2\gamma)}+\frac{1}{2}h_2T_{(10)}^{(2\gamma)}+\frac{1}{4}h_2^2T_{(20)}^{(2\gamma)}\right]^{(q,r)} = \left[T_{(00)}^{(1\gamma)}-\frac{1}{2}h_1T_{(10)}^{(1\gamma)}+\frac{1}{4}h_1^2T_{(20)}^{(1\gamma)}\right]^{(q+1,r)} \tag{24}$$

$$\left[T_{(00)}^{(\beta 1)}+\frac{1}{2}l_1T_{(01)}^{(\beta 1)}+\frac{1}{4}l_1^2T_{(02)}^{(\beta 1)}\right]^{(q,r)} = \left[T_{(00)}^{(\beta 2)}-\frac{1}{2}h_2T_{(01)}^{(\beta 2)}+\frac{1}{4}l_2^2T_{(02)}^{(\beta 2)}\right]^{(q,r)} \tag{25}$$

$$\left[T_{(00)}^{(\beta 2)}+\frac{1}{2}l_2T_{(01)}^{(\beta 2)}+\frac{1}{4}l_2^2T_{(02)}^{(\beta 2)}\right]^{(q,r)} = \left[T_{(00)}^{(\beta 1)}-\frac{1}{2}l_1T_{(01)}^{(\beta 1)}+\frac{1}{4}l_1^2T_{(02)}^{(\beta 1)}\right]^{(q,r+1)} \tag{26}$$

2.1.4 Boundary conditions

Some of the heat flux and temperature continuity conditions described above are not valid for cells located on the boundaries defined by the indices $q = 1, N_q$, and $r = 1, N_r$. For the set of boundary cells with $q = 1$, heat flux continuity between the given generic cell and preceding generic cell, Eqs. $(15) - (16)$, is not applicable. Similarly for $q = N_q$, temperature continuity between the given generic cell and following generic cell, Eq. (24), is not applicable. These conditions are replaced by the continuity of heat flux between adjacent subcells within the generic cell $(1, r)$, and in case of thermal boundary conditions by

$$\frac{1}{l_\gamma^{(r)}}\int_{-l_\gamma^{(r)}/2}^{l_\gamma^{(r)}/2}\left[T^{(1\gamma)}(-\frac{h_1^{(1)}}{2},\bar{x}_3^{(\gamma)})\right]^{(1,r)}d\bar{x}_3^{(\gamma)} = T_{left}^{(r)}(x_3) \tag{27}$$

$$\frac{1}{l_\gamma^{(r)}}\int_{-l_\gamma^{(r)}/2}^{l_\gamma^{(r)}/2}\left[T^{(1\gamma)}(\frac{h_2^{(N_q)}}{2},\bar{x}_3^{(\gamma)})\right]^{(N_q,r)}d\bar{x}_3^{(\gamma)} = T_{right}^{(r)}(x_3) \tag{28}$$

where $T^{(r)}_{left}(x_3)$, and $T^{(r)}_{right}(x_3)$ are the piece-wise uniform applied temperatures on the external boundaries in the $x_2 - x_3$ plane. Similar reasoning holds for generic cells $(q,1)$, and (q,N_r). If the temperatures are defined at the top and bottom surfaces for instance, the applied boundary conditions are given by

$$\frac{1}{h^{(q)}_\beta}\int_{-h^{(q)}_\beta/2}^{h^{(q)}_\beta/2}\left[T^{(\beta 1)}(\bar{x}^{(\beta)}_2,-\frac{l^{(1)}_1}{2})\right]^{(q,1)} d\bar{x}^{(\beta)}_2 = T^{(q)}_{bottom}(x_2) \quad (29)$$

$$\frac{1}{h^{(q)}_\beta}\int_{-h^{(q)}_\beta/2}^{h^{(q)}_\beta/2}\left[T^{(\beta 1)}(\bar{x}^{(\beta)}_2,\frac{l^{(N_r)}_2}{2})\right]^{(q,N_r)} d\bar{x}^{(\beta)}_2 = T^{(q)}_{top}(x_2) \quad (30)$$

If the heat flux at any of the boundaries is defined instead of the applied temperature, Eqs. $(27)-(30)$ are modified accordingly.

2.1.5 Solution for $T^{(\beta\gamma)}_{(mn)}$

To obtain a solution for the $20N_qN_r$ unknown coefficients ($T^{(\beta\gamma)}_{(mn)}$ in each $(\beta\gamma)$ subcell), $20N_qN_r$ equations are required. These equations are assembled using the governing field equations, Eq. (6), heat flux continuity conditions, Eqs. $(15)-(18)$, and the temperature continuity conditions, Eqs. $(23)-(26)$, together with the imposed boundary conditions on the external boundaries of the composite, Eqs. $(27)-(30)$. The final system of equations obtained is symbolically written as

$$\boldsymbol{\kappa}\ \mathbf{T} = \mathbf{t} \quad (31)$$

In the above equation, $\boldsymbol{\kappa}$ is the structural thermal conductivity matrix which contains information on the geometry and thermal conductivities of the individual subcells $(\beta\gamma)$ in the N_qN_r cells. The thermal coefficient vector $\mathbf{T}$ contains the unknown coefficients that describe the temperature field in each subcell, i.e.,

$$\mathbf{T} = [\mathbf{T}^{(11)}_{11},...,\mathbf{T}^{(22)}_{N_qN_r}]$$

where

$$\mathbf{T}^{(\beta\gamma)}_{qr} = [T_{(00)},T_{(10)},T_{(01)},T_{(20)},T_{(02)}]^{(\beta\gamma)}_{qr}$$

The thermal force vector $\mathbf{t}$ contains information on the boundary conditions.

2.2 Mechanical Analysis

The next step is to find the displacement and stress fields in the heterogeneous composite due to the temperature field obtained in Subsection 2.1, and/or mechanical loading at the external boundaries applied in a manner which is consistent with the global equilibrium requirements. Towards this end, the displacement field in the subcell $(\beta\gamma)$ of the $(q,r)^{th}$ generic cell is approximated by a second-order expansion in the local coordinates $\bar{x}^{(\beta)}_2$ and $\bar{x}^{(\gamma)}_3$ as follows:

$$u^{(\beta\gamma)}_1 = x_1\bar{\varepsilon}_{11} \quad (32)$$

$$u^{(\beta\gamma)}_2 = W^{(\beta\gamma)}_{2(00)} + \bar{x}^{(\beta)}_2 W^{(\beta\gamma)}_{2(10)} + \bar{x}^{(\gamma)}_3 W^{(\beta\gamma)}_{2(01)} + \frac{1}{2}(3\bar{x}^{(\beta)2}_2 - \frac{h^{(q)2}_\beta}{4})W^{(\beta\gamma)}_{2(20)} + \frac{1}{2}(3\bar{x}^{(\gamma)2}_3 - \frac{l^{(r)2}_\gamma}{4})W^{(\beta\gamma)}_{2(02)} \quad (33)$$

$$u^{(\beta\gamma)}_3 = W^{(\beta\gamma)}_{3(00)} + \bar{x}^{(\beta)}_2 W^{(\beta\gamma)}_{3(10)} + \bar{x}^{(\gamma)}_3 W^{(\beta\gamma)}_{3(01)} + \frac{1}{2}(3\bar{x}^{(\beta)2}_2 - \frac{h^{(q)2}_\beta}{4})W^{(\beta\gamma)}_{3(20)} + \frac{1}{2}(3\bar{x}^{(\gamma)2}_3 - \frac{l^{(r)2}_\gamma}{4})W^{(\beta\gamma)}_{3(02)} \quad (34)$$

where $W_{i(00)}^{(\beta\gamma)}$ are the volume-averaged displacements in the subcell $(\beta\gamma)$, and $W_{i(mn)}^{(\beta\gamma)}$ $(i = 2, 3)$ are the higher-order quantities which determine the displacement and stress field at specific locations within the subcell. Note that, in Eq. (32), x_1 is associated with the global coordinate system fixed to the edges of the composite plate and not the local coordinate system associated with each subcell. Also note that there are no product terms of the form $\bar{x}_2^{(\beta)}\bar{x}_3^{(\gamma)}$ appearing in the above displacement field approximation due to the employed volumetric and surface-averaging procedure technique. The quantity $\bar{\varepsilon}_{11}$ is the uniform strain in the x_1 direction which is zero for plane strain analysis. For generalized plane strain, $\bar{\varepsilon}_{11}$ is determined from the condition

$$\sum_{r=1}^{N_\gamma}\sum_{q=1}^{N_\beta}\left(\sum_{\beta=1}^{2}\sum_{\gamma=1}^{2}\int_{-h_\beta^{(q)}/2}^{h_\beta^{(q)}/2}\int_{-l_\gamma^{(r)}/2}^{l_\gamma^{(r)}/2}\sigma_{ij}^{(\beta\gamma)}d\bar{x}_2^{(\beta)}d\bar{x}_3^{(\gamma)}\right) = 0 \tag{35}$$

The other 10 unknown coefficients $W_{i(mn)}^{(\beta\gamma)}$ associated with each subcell $(\beta\gamma)$ of the $(q,r)^{th}$ generic cell are determined from the conditions analogous to those employed in the thermal problem. Here, the heat conduction equation is replaced by the two equilibrium equations, and the conditions involving continuity of heat fluxes and temperature at the interfaces are replaced by the continuity of tractions and displacements.

2.2.1 Equilibrium equations

The stress field in the subcell $(\beta\gamma)$ of the $(q,r)^{th}$ generic cell generated by the given temperature field and the applied mechanical loading must satisfy the equilibrium equations

$$\frac{\partial\sigma_{2j}^{(\beta\gamma)}}{\partial\bar{x}_2^{(\beta)}} + \frac{\partial\sigma_{3j}^{(\beta\gamma)}}{\partial\bar{x}_3^{(\gamma)}} = 0,\ (j = 2, 3) \tag{36}$$

For an orthotropic elastic material occupying the subcell $(\beta\gamma)$ of the $(q,r)^{th}$ generic cell, the stress components are related to the strain components through the familiar Hooke's law

$$\sigma_{ij}^{(\beta\gamma)} = C_{ijkl}^{(\beta\gamma)}\varepsilon_{kl}^{(\beta\gamma)} - \sigma_{ij}^{T(\beta\gamma)} \tag{37}$$

where C_{ijkl} are the stiffness tensor elements of the material in the subcell $(\beta\gamma)$, $\varepsilon_{ij}^{(\beta\gamma)}$ are the elastic strain components, and $\sigma_{ij}^{T(\alpha\beta\gamma)}$ are the components of the so-called thermal stress given by

$$\sigma_{ij}^{T(\beta\gamma)} = \Gamma_{ij}^{(\beta\gamma)}T^{(\beta\gamma)} \tag{38}$$

where $\Gamma_{ij}^{(\beta\gamma)}$ is the product of the stiffness tensor components and thermal expansion coefficients. $T^{(\beta\gamma)}$ represents the temperature change at a particular location in the subcell.

The components of the strain tensor in the individual subcells are obtained from the following strain-displacement relations

$$\varepsilon_{ij}^{(\beta\gamma)} = \frac{1}{2}\left(\frac{\partial u_j^{(\beta\gamma)}}{\partial\bar{x}_i^{(\cdot)}} + \frac{\partial u_i^{(\beta\gamma)}}{\partial\bar{x}_j^{(\cdot)}}\right) \tag{39}$$

As in the thermal formulation case, in order to satisfy the equilibrium equations in an average sense the following volume-averaged stress quantities are defined in the higher-order theory

$$S_{ij(m,n)}^{(\beta\gamma)} = \frac{1}{A_{(\beta\gamma)}^{(q,r)}}\int_{-h_\beta^{(q)}/2}^{h_\beta^{(q)}/2}\int_{-l_\gamma^{(r)}/2}^{l_\gamma^{(r)}/2}(\bar{x}_2^{(\beta)})^m(\bar{x}_3^{(\gamma)})^n\sigma_{ij}^{(\beta\gamma)}d\bar{x}_2^{(\beta)}d\bar{x}_3^{(\gamma)} \tag{40}$$

where $S^{(\beta\gamma)}_{ij(0,0)}$ is the average value of the stress component $\sigma^{(\beta\gamma)}_{ij}$ in the subcell, whereas for other values of m and n Eq. (40) defines higher-order stresses that are needed to describe the governing field equations of the higher-order continuum. Satisfaction of the equilibrium equation (36) results in the following eight equations in terms of the volume-averaged stress quantities

$$\left[S^{(\beta\gamma)}_{2j(1,0)}/h^2_\beta + S^{(\beta\gamma)}_{3j(0,1)}/l^2_\gamma\right]^{(q,r)} = 0 \tag{41}$$

Equation (41) can be expressed in terms of the coefficients $W^{(\beta\gamma)}_{i(mn)}$ by evaluating the stress quantities defined in Eq. (40). Substituting Eqs. (37), (38), and (39) in Eq. (40), making use of the displacement field representation, Eqs. (32) − (34), and performing the required volume integration yields the following non-vanishing zeroth and first-order stress components in terms of the coefficients $W^{(\beta\gamma)}_{i(mn)}$

$$\begin{aligned}
S^{(\beta\gamma)}_{22(0,0)} &= C^{(\beta\gamma)}_{22}W^{(\beta\gamma)}_{2(10)} + C^{(\beta\gamma)}_{23}W^{(\beta\gamma)}_{3(01)} - \Gamma^{(\beta\gamma)}_{22}T^{(\beta\gamma)}_{(00)} && (42)\\
S^{(\beta\gamma)}_{22(1,0)} &= \frac{1}{4}h^{(q)2}_\beta C^{(\beta\gamma)}_{22}W^{(\beta\gamma)}_{2(20)} - \frac{1}{12}h^{(q)2}_\beta \Gamma^{(\beta\gamma)}_{22}T^{(\beta\gamma)}_{(10)} && (43)\\
S^{(\beta\gamma)}_{22(0,1)} &= \frac{1}{4}l^{(r)2}_\gamma C^{(\beta\gamma)}_{23}W^{(\beta\gamma)}_{2(02)} - \frac{1}{12}l^{(r)2}_\gamma \Gamma^{(\beta\gamma)}_{22}T^{(\beta\gamma)}_{(01)} && (44)\\
S^{(\beta\gamma)}_{33(0,0)} &= C^{(\beta\gamma)}_{23}W^{(\beta\gamma)}_{2(10)} + C^{(\beta\gamma)}_{33}W^{(\beta\gamma)}_{3(01)} - \Gamma^{(\beta\gamma)}_{33}T^{(\beta\gamma)}_{(00)} && (45)\\
S^{(\beta\gamma)}_{33(1,0)} &= \frac{1}{4}h^{(q)2}_\beta C^{(\beta\gamma)}_{23}W^{(\beta\gamma)}_{2(20)} - \frac{1}{12}h^{(q)2}_\beta \Gamma^{(\beta\gamma)}_{33}T^{(\beta\gamma)}_{(10)} && (46)\\
S^{(\beta\gamma)}_{33(0,1)} &= \frac{1}{4}l^{(r)2}_\gamma C^{(\beta\gamma)}_{33}W^{(\beta\gamma)}_{2(02)} - \frac{1}{12}l^{(r)2}_\gamma \Gamma^{(\beta\gamma)}_{33}T^{(\beta\gamma)}_{(01)} && (47)\\
S^{(\beta\gamma)}_{23(0,0)} &= C^{(\beta\gamma)}_{44}(W^{(\beta\gamma)}_{2(01)} + W^{(\beta\gamma)}_{3(10)}) && (48)\\
S^{(\beta\gamma)}_{23(1,0)} &= \frac{1}{4}h^{(q)2}_\beta C^{(\beta\gamma)}_{44}W^{(\beta\gamma)}_{3(20)} && (49)\\
S^{(\beta\gamma)}_{23(0,1)} &= \frac{1}{4}l^{(r)2}_\gamma C^{(\beta\gamma)}_{44}W^{(\beta\gamma)}_{2(02)} && (50)
\end{aligned}$$

2.2.2 Traction continuity conditions

The traction continuity at the interfaces separating adjacent subcells within the generic cell (q, r) is imposed in an integral sense as follows

$$\frac{1}{l^{(r)}_\gamma}\int_{-l^{(r)}_\gamma/2}^{l^{(r)}_\gamma/2}\left[\sigma^{(1\gamma)}_{2j}(\frac{h^{(q)}_1}{2},\bar{x}^{(\gamma)}_3)\right]^{(q,r)} d\bar{x}^{(\gamma)}_3 = \frac{1}{l^{(r)}_\gamma}\int_{-l^{(r)}_\gamma/2}^{l^{(r)}_\gamma/2}\left[\sigma^{(2\gamma)}_{2j}(-\frac{h^{(q)}_2}{2},\bar{x}^{(\gamma)}_3)\right]^{(q,r)} d\bar{x}^{(\gamma)}_3 \tag{51}$$

$$\frac{1}{h^{(q)}_\beta}\int_{-h^{(q)}_\beta/2}^{h^{(q)}_\beta/2}\left[\sigma^{(\beta 1)}_{i3}(\bar{x}^{(\beta)}_2,\frac{l^{(r)}_1}{2})\right]^{(q,r)} d\bar{x}^{(\beta)}_2 = \frac{1}{h^{(q)}_\beta}\int_{-h^{(q)}_\beta/2}^{h^{(q)}_\beta/2}\left[\sigma^{(\beta 2)}_{i3}(\bar{x}^{(\beta)}_2,-\frac{l^{(r)}_2}{2})\right]^{(q,r)} d\bar{x}^{(\beta)}_2 \tag{52}$$

where $i, j = 2, 3$. Similarly, the traction continuity at the interfaces between generic cells is satisfied in an integral sense by requiring that

$$\frac{1}{l^{(r)}_\gamma}\int_{-l^{(r)}_\gamma/2}^{l^{(r)}_\gamma/2}\left[\sigma^{(1\gamma)}_{2j}(-\frac{h^{(q+1)}_1}{2},\bar{x}^{(\gamma)}_3)\right]^{(q+1,r)} d\bar{x}^{(\gamma)}_3 = \frac{1}{l^{(r)}_\gamma}\int_{-l^{(r)}_\gamma/2}^{l^{(r)}_\gamma/2}\left[\sigma^{(2\gamma)}_{2j}(\frac{h^{(q)}_2}{2},\bar{x}^{(\gamma)}_3)\right]^{(q,r)} d\bar{x}^{(\gamma)}_3 \tag{53}$$

$$\frac{1}{h_\beta^{(q)}}\int_{-h_\beta^{(q)}/2}^{h_\beta^{(q)}/2}\left[\sigma_{i3}^{(\beta 1)}(\bar{x}_2^{(\beta)},-\frac{l_1^{(r+1)}}{2})\right]^{(q,r+1)}d\bar{x}_2^{(\beta)}=\frac{1}{h_\beta^{(q)}}\int_{-h_\beta^{(q)}/2}^{h_\beta^{(q)}/2}\left[\sigma_{i3}^{(\beta 2)}(\bar{x}_2^{(\beta)},\frac{l_2^{(r)}}{2})\right]^{(q,r)}d\bar{x}_2^{(\beta)} \tag{54}$$

where $i,j=2,3$. Satisfaction of the above traction continuity conditions $(51)-(54)$ results in the following sixteen equations in terms of the volume-averaged stress quantities

$$\left[-12S_{2j(1,0)}^{(1\gamma)}/h_1+S_{2j(0,0)}^{(2\gamma)}-6S_{2j(1,0)}^{(2\gamma)}/h_2\right]^{(q,r)}-\left[S_{2j(0,0)}^{(2\gamma)}+6S_{2j(1,0)}^{(2\gamma)}/h_2\right]^{(q-1,r)}=0 \tag{55}$$

$$\left[-S_{2j(0,0)}^{(1\gamma)}+\frac{1}{2}S_{2j(0,0)}^{(2\gamma)}-3S_{2j(1,0)}^{(2\gamma)}/h_2\right]^{(q,r)}+\frac{1}{2}\left[S_{2j(0,0)}^{(2\gamma)}+6S_{2j(1,0)}^{(2\gamma)}/h_2\right]^{(q-1,r)}=0 \tag{56}$$

$$\left[-12S_{3j(0,1)}^{(\beta 1)}/l_1+S_{3j(0,0)}^{(\beta 2)}-6S_{3j(0,1)}^{(\beta 2)}/l_2\right]^{(q,r)}-\left[S_{3j(0,0)}^{(\beta 2)}+6S_{3j(0,1)}^{(\beta 2)}/l_2\right]^{(q,r-1)}=0 \tag{57}$$

$$\left[-S_{3j(0,0)}^{(\beta 1)}+\frac{1}{2}S_{3j(0,0)}^{(\beta 2)}-3S_{3j(0,1)}^{(\beta 2)}/l_2\right]^{(q,r)}+\frac{1}{2}\left[S_{3j(0,0)}^{(\beta 2)}+6S_{3j(0,1)}^{(\beta 2)}/l_2\right]^{(q,r-1)}=0 \tag{58}$$

where $j=2,3$. Equations (41) and $(55)-(58)$ have been obtained in terms of the volume-averaged stress quantities after some complex algebraic manipulations. For detailed derivation of these equations, refer to Aboudi et al. (1996). These equations can now be expressed explicitly in terms of the microvariables $W_{2(mn)}^{(\beta\gamma)}$ and $W_{3(mn)}^{(\beta\gamma)}$ with the use of Eqs. $(42)-(50)$.

2.2.3 Displacement continuity conditions

The displacement continuity at the interfaces separating adjacent subcells within the generic cell (q,r) is imposed in an integral sense as follows

$$\frac{1}{l_\gamma^{(r)}}\int_{-l_\gamma^{(r)}/2}^{l_\gamma^{(r)}/2}\left[u_2^{(1\gamma)}(\frac{h_1^{(q)}}{2},\bar{x}_3^{(\gamma)})\right]^{(q,r)}d\bar{x}_3^{(\gamma)}=\frac{1}{l_\gamma^{(r)}}\int_{-l_\gamma^{(r)}/2}^{l_\gamma^{(r)}/2}\left[u_2^{(2\gamma)}(-\frac{h_2^{(q)}}{2},\bar{x}_3^{(\gamma)})\right]^{(q,r)}d\bar{x}_3^{(\gamma)} \tag{59}$$

$$\frac{1}{h_\beta^{(q)}}\int_{-h_\beta^{(q)}/2}^{h_\beta^{(q)}/2}\left[u_3^{(\beta 1)}(\bar{x}_2^{(\beta)},\frac{l_1^{(r)}}{2})\right]^{(q,r)}d\bar{x}_2^{(\beta)}=\frac{1}{h_\beta^{(q)}}\int_{-h_\beta^{(q)}/2}^{h_\beta^{(q)}/2}\left[u_3^{(\beta 2)}(\bar{x}_2^{(\beta)},-\frac{l_2^{(r)}}{2})\right]^{(q,r)}d\bar{x}_2^{(\beta)} \tag{60}$$

Similarly, the displacement continuity at the interfaces between generic cells is satisfied in an integral sense by requiring that

$$\frac{1}{l_\gamma^{(r)}}\int_{-l_\gamma^{(r)}/2}^{l_\gamma^{(r)}/2}\left[u_2^{(1\gamma)}(-\frac{h_1^{(q+1)}}{2},\bar{x}_3^{(\gamma)})\right]^{(q+1,r)}d\bar{x}_3^{(\gamma)}=\frac{1}{l_\gamma^{(r)}}\int_{-l_\gamma^{(r)}/2}^{l_\gamma^{(r)}/2}\left[u_2^{(2\gamma)}(\frac{h_2^{(q)}}{2},\bar{x}_3^{(\gamma)})\right]^{(q,r)}d\bar{x}_3^{(\gamma)} \tag{61}$$

$$\frac{1}{h_\beta^{(q)}}\int_{-h_\beta^{(q)}/2}^{h_\beta^{(q)}/2}\left[u_3^{(\beta 1)}(\bar{x}_2^{(\beta)},-\frac{l_1^{(r+1)}}{2})\right]^{(q,r+1)}d\bar{x}_2^{(\beta)}=\frac{1}{h_\beta^{(q)}}\int_{-h_\beta^{(q)}/2}^{h_\beta^{(q)}/2}\left[u_3^{(\beta 2)}(\bar{x}_2^{(\beta)},\frac{l_2^{(r)}}{2})\right]^{(q,r)}d\bar{x}_2^{(\beta)} \tag{62}$$

Satisfaction of the above displacement continuity conditions results in the following sixteen equations expressed directly in terms of the microvariables $W_{2(mn)}^{(\beta\gamma)}$ and $W_{3(mn)}^{(\beta\gamma)}$

$$\left[W_{j(00)}^{(1\gamma)}+\frac{1}{2}h_1W_{j(10)}^{(1\gamma)}+\frac{1}{4}h_1^2W_{j(20)}^{(1\gamma)}\right]^{(q,r)}=\left[W_{j(00)}^{(2\gamma)}-\frac{1}{2}h_2W_{j(10)}^{(2\gamma)}+\frac{1}{4}h_2^2W_{j(20)}^{(2\gamma)}\right]^{(q,r)} \tag{63}$$

$$\left[W^{(2\gamma)}_{j(00)} + \frac{1}{2}h_2 W^{(2\gamma)}_{j(10)} + \frac{1}{4}h_2^2 W^{(2\gamma)}_{j(20)}\right]^{(q,r)} = \left[W^{(1\gamma)}_{j(00)} - \frac{1}{2}h_1 W^{(1\gamma)}_{j(10)} + \frac{1}{4}h_1^2 W^{(1\gamma)}_{j(20)}\right]^{(q+1,r)} \tag{64}$$

$$\left[W^{(\beta 1)}_{j(00)} + \frac{1}{2}l_1 W^{(\beta 1)}_{j(01)} + \frac{1}{4}l_1^2 W^{(\beta 1)}_{j(02)}\right]^{(q,r)} = \left[W^{(\beta 2)}_{j(00)} - \frac{1}{2}h_2 W^{(\beta 2)}_{j(01)} + \frac{1}{4}l_2^2 W^{(\beta 2)}_{j(02)}\right]^{(q,r)} \tag{65}$$

$$\left[W^{(\beta 2)}_{j(00)} + \frac{1}{2}l_2 W^{(\beta 2)}_{j(01)} + \frac{1}{4}l_2^2 W^{(\beta 2)}_{j(02)}\right]^{(q,r)} = \left[W^{(\beta 1)}_{j(00)} - \frac{1}{2}l_1 W^{(\beta 1)}_{j(01)} + \frac{1}{4}l_1^2 W^{(\beta 1)}_{j(02)}\right]^{(q,r+1)} \tag{66}$$

2.2.4 Boundary conditions

As in the thermal analysis case, some of the displacement and traction continuity conditions described above are not valid for generic cells located at the boundaries defined by the indices $q = 1, N_q$, and $r = 1, N_r$. For the set of boundary cells with $q = 1$, the traction continuity between the given generic cell and preceding generic cell, Eqs. $(55) - (56)$, is not applicable. Similarly for $q = N_q$, the displacement continuity between the given generic cell and following generic cell, Eq. (64), is not applicable. These conditions are replaced the continuity of tractions between adjacent subcells within the generic cell $(1, r)$, and in case of traction boundary conditions by

$$\frac{1}{l_\gamma^{(r)}}\int_{-l_\gamma^{(r)}/2}^{l_\gamma^{(r)}/2}\left[\sigma_{2j}^{(1\gamma)}(-\frac{h_1^{(1)}}{2}, \bar{x}_3^{(\gamma)})\right]^{(1,r)} d\bar{x}_3^{(\gamma)} = t_{left}^{(r)}(x_3) \tag{67}$$

$$\frac{1}{l_\gamma^{(r)}}\int_{-l_\gamma^{(r)}/2}^{l_\gamma^{(r)}/2}\left[\sigma_{2j}^{(1\gamma)}(\frac{h_2^{(N_q)}}{2}, \bar{x}_3^{(\gamma)})\right]^{(N_q,r)} d\bar{x}_3^{(\gamma)} = t_{right}^{(r)}(x_3) \tag{68}$$

$$j = 2, 3$$

where $t_{left}^{(r)}(x_3)$, and $t_{right}^{(r)}(x_3)$ are the piece-wise uniform applied surface tractions. Similar reasoning holds for generic cells $(q, 1)$, and (q, N_r). If the top and the bottom surfaces are fixed for instance, the applied boundary conditions are given by

$$\frac{1}{h_\beta^{(q)}}\int_{-h_\beta^{(q)}/2}^{h_\beta^{(q)}/2}\left[u_i^{(\beta 1)}(\bar{x}_2^{(\beta)}, -\frac{l_1^{(1)}}{2})\right]^{(q,1)} d\bar{x}_2^{(\beta)} = 0 \tag{69}$$

$$\frac{1}{h_\beta^{(q)}}\int_{-h_\beta^{(q)}/2}^{h_\beta^{(q)}/2}\left[u_i^{(\beta 1)}(\bar{x}_2^{(\beta)}, \frac{l_2^{(N_r)}}{2})\right]^{(q,N_r)} d\bar{x}_2^{(\beta)} = 0 \tag{70}$$

For other type of boundary conditions, Eqs. $(67) - (70)$ are modified accordingly.

2.2.5 Solution for $W^{(\beta\gamma)}_{i(mn)}$

Thus for the solution of the $40N_qN_r$ unknown coefficients $W^{(\beta\gamma)}_{i(mn)}$ in each $(\beta\gamma)$ subcell, $40N_qN_r$ equations are assembled using the governing field equations, Eq. (41), traction continuity conditions, Eqs. $(55) - (58)$, and the displacement continuity conditions, Eqs. $(63) - (66)$, together with the imposed boundary conditions on the external boundaries of the composite, Eqs. $(67) - (70)$. The final system of equations obtained is symbolically written as

$$\mathbf{K}\ \mathbf{U} = \mathbf{f} \tag{71}$$

In the above equation, $\mathbf{K}$ is the structural stiffness matrix which contains information on the geometry and thermomechanical properties of the individual subcells $(\beta\gamma)$ in the N_qN_r generic cells. The displacement coefficient vector $\mathbf{U}$ contains the unknown coefficients that describe the displacement field in each subcell, i.e.,

$$\mathbf{U} = [\mathbf{U}_{11}^{(11)}, ..., \mathbf{U}_{N_qN_r}^{(22)}] \tag{72}$$

where

$$\mathbf{U}_{qr}^{(\beta\gamma)} = [W_{2(00)}, ..., W_{3(02)}]_{qr}^{(\beta\gamma)}$$

The mechanical force vector $\mathbf{f}$ contains information on the boundary conditions and the thermal loading effects generated by the applied temperature.

3 Higher-Order Theory: Efficient Reformulation

The basic equations of the original higher-order theory outlined in Section 2 will be contrasted and compared with the reformulated equations developed in this section. The reformulation simplifies the theory and makes it computationally more efficient, as will be demonstrated later. It must be emphasized that the basic structure and concepts of the higher-order theory with regard to the temperature and displacement field approximation based on the quadratic expansion in the local coordinate system attached to a subcell's center, satisfaction of the governing field equations (steady state heat conduction equation and equilibrium equations) in a volumetric sense, and the interfacial continuity and boundary conditions in a surface-integral sense, do not change. The major changes involve

- simplification of the volume discretization by eliminating the concept of generic cells, leaving only subcells as the basic building blocks of the material's microstructure
- replacement of volume-averaged heat flux and stress quantities defined in Section 2 by Eqs. (5) and (40) , respectively, by surface-averaged quantities (temperature and heat flux for thermal analysis, displacements and stresses for mechanical) associated with subcell interfaces as the fundamental unknown quantities

The above changes set the stage for reformulating the higher-order theory based on the local-global conductivity and stiffness matrix approaches described in the following subsections. As shown in Fig. 2, the microstructural pattern of the heterogeneous composite functionally graded in the $x_2 - x_3$ plane is represented by discretizing the cross-section into N_β and N_γ subcells in the intervals $0 \leq x_2 \leq H$, and $0 \leq x_3 \leq L$, respectively. The thermomechanical properties within a subcell are assumed to be constant. The composite is assumed to be infinite in the x_1 direction, whereas the dimensions of the subcell along the functionally graded directions x_2 and x_3 are h_β, l_γ, and can vary arbitrarily such that

$$H = \sum_{\beta=1}^{N_\beta} h_\beta \qquad L = \sum_{\gamma=1}^{N_\gamma} l_\gamma \tag{73}$$

The composite is subjected to a combination of surface displacements and/or tractions applied in the $x_2 - x_3$ plane along with a uniform strain $\bar{\varepsilon}_{11}$ ($\bar{\varepsilon}_{11} = 0$, for plane strain) in the x_1 direction. An arbitrary surface temperature or heat flux distribution may also be prescribed.

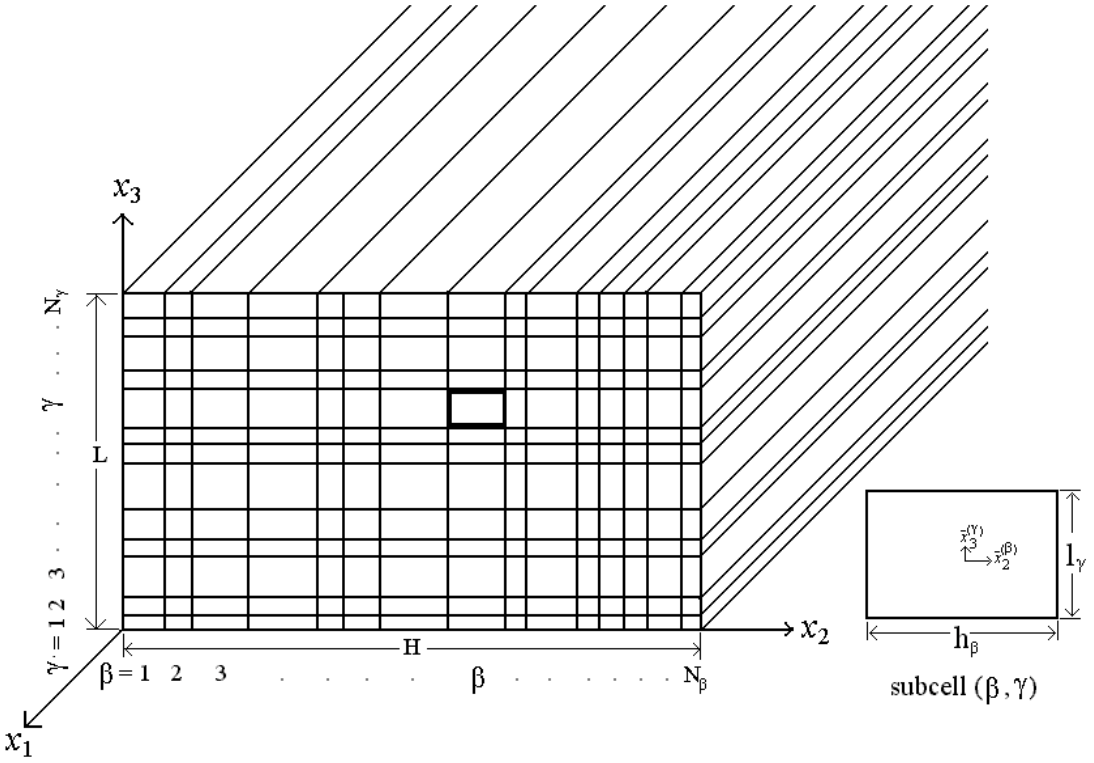

Fig. 2. Reformulated HOTFGM-2D representation of a composite functionally graded in the x_2 and x_3 directions with uniform microstructure in the x_1 direction.

In the case of the original higher-order theory, the global conductivity matrix relates the heat flux defined at the boundaries to the microvariables $T_{(mn)}^{(\beta,\gamma)}$ and the global stiffness matrix relates the tractions applied at the boundaries to the microvariables $W_{i(mn)}^{(\beta,\gamma)}$. In contrast, in the reformulated version the global conductivity matrix relates the heat flux defined at the boundaries to the common interfacial surface-averaged temperatures and surface-averaged temperatures at the outer surfaces. The global stiffness matrix relates the tractions at the boundaries to the common interfacial surface-averaged displacements and surface-averaged displacements at the boundaries.

3.1 Motivation for Reformulation

The motivation behind the reformulation of the higher-order theory is to decrease the number of equations in order to make it computationally more efficient. This is achieved by using the local-global conductivity and local-global stiffness matrix approach. This approach involves formulation of a local conductivity matrix that relates heat fluxes to temperatures, and a local stiffness matrix that relates tractions to displacements, evaluated at the external boundaries of each subvolume, and has been described in detail by Pindera (1991) in the context of mechanical boundary-value problems. In the reformulated version of the higher-order theory, the local conductivity matrix relates the *surface-averaged* fluxes to the *surface-averaged* temperatures for a particular subcell (β, γ), accounting for the satisfaction of the steady-state heat conduction equation. Similarly, the local stiffness matrix relates the *surface-averaged* tractions to the *surface-averaged* displacements for a particular subcell (β, γ), accounting for the satisfaction of the global equilibrium requirements in a volumetric sense. Once the local conductivity and stiffness matrices are formed, we

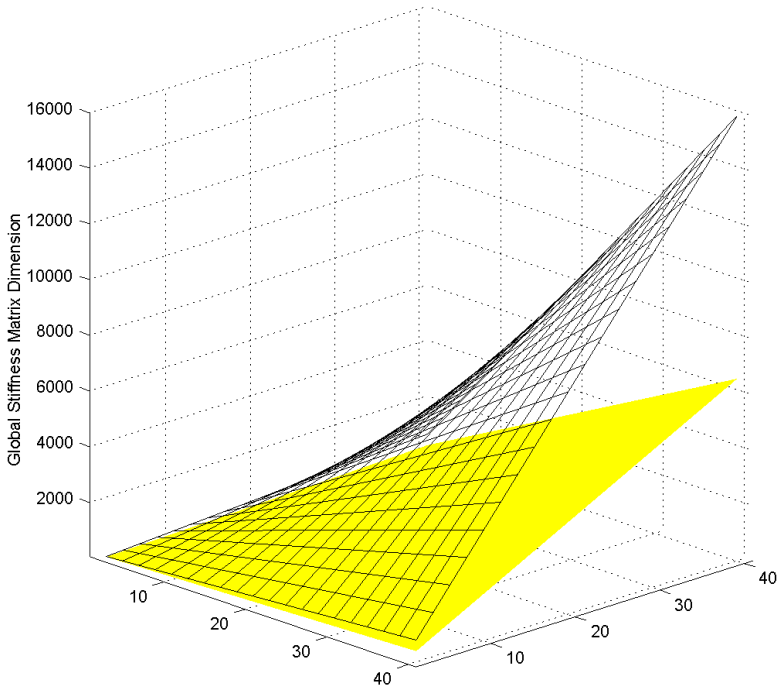

Fig. 3. Reduction in the size of the global stiffness matrix due to reformulation.

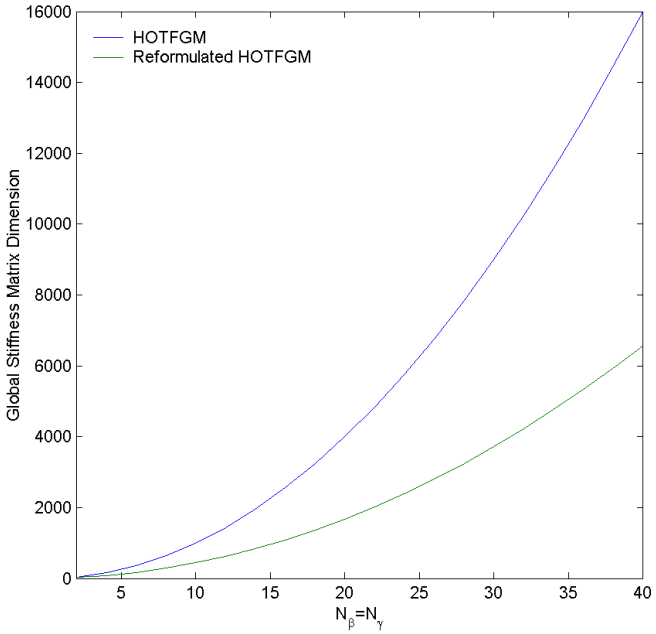

Fig. 4. Reduction in the size of the global stiffness matrix due to reformulation for equal number of subcells in the x_2 and x_3 directions.

use them to construct the global conductivity and stiffness matrices. Here, we enforce the traction and displacement (heat flux and temperature for thermal analysis) continuity conditions at the interfaces of the adjacent subcells in an average sense, thereby reducing the size of the global conductivity matrix and global stiffness matrix by more than fifty percent.

When the composite is discretized into N_β and N_γ subcells in the x_2 and x_3 directions, respectively, the rank of the global stiffness matrix in the original higher-order theory is $10N_\beta N_\gamma$ since, according to Section 2, each generic cell contains 4 subcells. As we shall see in this section, for the same number of subcells in the x_2 and x_3 directions, the rank of the global stiffness matrix in the reformulated version is reduced to $4N_\beta N_\gamma + 2N_\beta + 2N_\gamma$ ($4N_\beta N_\gamma + 2N_\beta + 2N_\gamma + 1$ for generalized plane strain). Thus for higher values of N_β and N_γ, the rank of the global stiffness matrix is reduced by approximately sixty percent as shown in Figs. 3 and 4.

3.2 Thermal Reformulation

The temperature distribution $T^{(\beta,\gamma)}$ in the subcell (β,γ) measured with respect to the reference temperature T_{ref} is approximated by the same second order polynomial expansion in the local coordinates $\overline{x}_2^{(\beta)}$, $\overline{x}_3^{(\gamma)}$ as that given by Eq. (2), reproduced below for convenience

$$T^{(\beta,\gamma)} = T_{(00)}^{(\beta,\gamma)} + \bar{x}_2^{(\beta)} T_{(10)}^{(\beta,\gamma)} + \bar{x}_3^{(\gamma)} T_{(01)}^{(\beta,\gamma)} + \frac{1}{2}(3\bar{x}_2^{(\beta)2} - \frac{h_\beta}{4}) T_{(20)}^{(\beta,\gamma)} + \frac{1}{2}(3\bar{x}_3^{(\gamma)2} - \frac{l_\gamma}{4}) T_{(02)}^{(\beta,\gamma)} \tag{74}$$

As given in Eq. (4), the heat flux at any point passing through a subcell (β,γ) is dictated by the Fourier's law of heat conduction,

$$q_i^{(\beta,\gamma)} = -k_i^{(\beta,\gamma)} \frac{\partial T^{(\beta,\gamma)}}{\partial \bar{x}_i^{(\cdot)}}, \ (i = 2,3; \ no \ sum) \tag{75}$$

where $k_i^{(\beta,\gamma)}$ are the heat conductivity coefficients of the material in the subcell (β,γ). Substituting Eq. (74) for the assumed temperature field in the above equation and simplifying, we get

$$q_2^{(\beta,\gamma)} = -k_2^{(\beta,\gamma)} \left(T_{(10)}^{(\beta,\gamma)} + 3\overline{x}_2^{(\beta)} T_{(20)}^{(\beta,\gamma)} \right) \tag{76}$$

$$q_3^{(\beta,\gamma)} = -k_3^{(\beta,\gamma)} \left(T_{(01)}^{(\beta,\gamma)} + 3\overline{x}_3^{(\gamma)} T_{(02)}^{(\beta,\gamma)} \right) \tag{77}$$

As mentioned earlier, the reformulation employs surface-averaged quantities in contrast with volume-averaged quantities in the original formulation. Hence, the surface-averaged temperatures and surface-averaged heat fluxes at the outer faces of the subcell are defined below. The surface-averaged heat flux $\bar{Q}_2^{-(\beta,\gamma)}$ going into the left face of the subcell (β,γ) is defined as

$$\bar{Q}_2^{-(\beta,\gamma)} = \frac{1}{l_\gamma} \int_{-l_\gamma/2}^{l_\gamma/2} q_2^{(\beta,\gamma)}(-\frac{h_\beta}{2}, \bar{x}_3^{(\gamma)}) d\bar{x}_3^{(\gamma)} \tag{78}$$

The surface-averaged heat flux $\bar{Q}_2^{+(\beta,\gamma)}$ going out of the right face of the subcell (β,γ) is defined as

$$\bar{Q}_2^{+(\beta,\gamma)} = \frac{1}{l_\gamma} \int_{-l_\gamma/2}^{l_\gamma/2} q_2^{(\beta,\gamma)}(\frac{h_\beta}{2}, \bar{x}_3^{(\gamma)}) d\bar{x}_3^{(\gamma)} \tag{79}$$

The surface-averaged heat flux $\bar{Q}_3^{-(\beta,\gamma)}$ going into the bottom face of the subcell (β,γ) is defined as

$$\bar{Q}_3^{-(\beta,\gamma)} = \frac{1}{h_\beta} \int_{-h_\beta/2}^{h_\beta/2} q_3^{(\beta,\gamma)}(\bar{x}_2^{(\beta)}, -\frac{l_\gamma}{2}) d\bar{x}_2^{(\beta)} \tag{80}$$

The surface-averaged heat flux $\bar{Q}_3^{+(\beta,\gamma)}$ going out of the top face of the subcell (β,γ) is defined as

$$\bar{Q}_3^{+(\beta,\gamma)} = \frac{1}{h_\beta}\int_{-h_\beta/2}^{h_\beta/2} q_3^{(\beta,\gamma)}(\bar{x}_2^{(\beta)}, \frac{l_\gamma}{2}) d\bar{x}_2^{(\beta)} \tag{81}$$

Substituting Eq. (76) into Eqs. (78) and (79), and Eq. (77) into Eqs. (80) and (81) , and performing the required integrations, we obtain

$$\bar{Q}_2^{-(\beta,\gamma)} = -k_2^{(\beta,\gamma)}\left(T_{(10)}^{(\beta,\gamma)} - \frac{3h_\beta}{2}T_{(20)}^{(\beta,\gamma)}\right) \tag{82}$$

$$\bar{Q}_2^{+(\beta,\gamma)} = -k_2^{(\beta,\gamma)}\left(T_{(10)}^{(\beta,\gamma)} + \frac{3h_\beta}{2}T_{(20)}^{(\beta,\gamma)}\right) \tag{83}$$

$$\bar{Q}_3^{-(\beta,\gamma)} = -k_3^{(\beta,\gamma)}\left(T_{(01)}^{(\beta,\gamma)} - \frac{3l_\gamma}{2}T_{(02)}^{(\beta,\gamma)}\right) \tag{84}$$

$$\bar{Q}_3^{+(\beta,\gamma)} = -k_3^{(\beta,\gamma)}\left(T_{(01)}^{(\beta,\gamma)} + \frac{3l_\gamma}{2}T_{(02)}^{(\beta,\gamma)}\right) \tag{85}$$

Assembling Eqs. $(82)-(85)$ in matrix form, we have

$$\begin{bmatrix} \bar{Q}_2^+ \\ \bar{Q}_2^- \end{bmatrix}^{(\beta,\gamma)} = -k_2^{(\beta,\gamma)} \begin{bmatrix} 1 & \frac{3h_\beta}{2} \\ 1 & -\frac{3h_\beta}{2} \end{bmatrix} \begin{bmatrix} T_{(10)} \\ T_{(20)} \end{bmatrix}^{(\beta,\gamma)} \tag{86}$$

$$\begin{bmatrix} \bar{Q}_3^+ \\ \bar{Q}_3^- \end{bmatrix}^{(\beta,\gamma)} = -k_3^{(\beta,\gamma)} \begin{bmatrix} 1 & \frac{3l_\gamma}{2} \\ 1 & -\frac{3l_\gamma}{2} \end{bmatrix} \begin{bmatrix} T_{(01)} \\ T_{(02)} \end{bmatrix}^{(\beta,\gamma)} \tag{87}$$

Equations (86) and (87) relate the surface-averaged heat fluxes to the microvariables $T_{(mn)}^{(\beta,\gamma)}$. Next, we express the microvariables $T_{(mn)}^{(\beta,\gamma)}$ in terms of the surface-averaged temperatures in order to form the local conductivity matrix that relates the surface-averaged fluxes to the surface-averaged temperatures for a particular subcell (β,γ). Hence, we proceed to define the surface-averaged temperatures as we have defined the surface-averaged heat fluxes above. At the left face of the subcell (β,γ) i.e. at $\overline{x}_2^{(\beta)} = -h_\beta/2$, the surface-averaged temperature $\bar{T}_2^{-(\beta,\gamma)}$ is defined as

$$\bar{T}_2^{-(\beta,\gamma)} = \frac{1}{l_\gamma}\int_{-l_\gamma/2}^{l_\gamma/2} T^{(\beta,\gamma)}(-\frac{h_\beta}{2}, \bar{x}_3^{(\gamma)}) d\bar{x}_3^{(\gamma)} \tag{88}$$

Similarly, at the right face of the subcell (β,γ), the surface-averaged temperature $\bar{T}_2^{+(\beta,\gamma)}$ is defined as

$$\bar{T}_2^{+(\beta,\gamma)} = \frac{1}{l_\gamma}\int_{-l_\gamma/2}^{l_\gamma/2} T^{(\beta,\gamma)}(\frac{h_\beta}{2}, \bar{x}_3^{(\gamma)}) d\bar{x}_3^{(\gamma)} \tag{89}$$

At the bottom face of the subcell (β,γ), the surface-averaged temperature $\bar{T}_3^{-(\beta,\gamma)}$ is defined as

$$\bar{T}_3^{-(\beta,\gamma)} = \frac{1}{h_\beta}\int_{-h_\beta/2}^{h_\beta/2} T^{(\beta,\gamma)}(\bar{x}_2^{(\beta)}, -\frac{l_\gamma}{2}) d\bar{x}_2^{(\beta)} \tag{90}$$

At the top face of the subcell (β,γ), the surface-averaged temperature $\bar{T}_3^{+(\beta,\gamma)}$ is defined as

$$\bar{T}_3^{+(\beta,\gamma)} = \frac{1}{h_\beta}\int_{-h_\beta/2}^{h_\beta/2} T^{(\beta,\gamma)}(\bar{x}_2^{(\beta)}, \frac{l_\gamma}{2}) d\bar{x}_2^{(\beta)} \tag{91}$$

Substituting the expression for $T^{(\beta,\gamma)}$ given by Eq. (74) into the above definitions and performing the averaging procedure, we obtain

$$\bar{T}_2^{-(\beta,\gamma)} = T_{(00)}^{(\beta,\gamma)} - \frac{h_\beta}{2} T_{(10)}^{(\beta,\gamma)} + \frac{h_\beta^2}{4} T_{(20)}^{(\beta,\gamma)} \tag{92}$$

$$\bar{T}_2^{+(\beta,\gamma)} = T_{(00)}^{(\beta,\gamma)} + \frac{h_\beta}{2} T_{(10)}^{(\beta,\gamma)} + \frac{h_\beta^2}{4} T_{(20)}^{(\beta,\gamma)} \tag{93}$$

$$\bar{T}_3^{-(\beta,\gamma)} = T_{(00)}^{(\beta,\gamma)} - \frac{l_\gamma}{2} T_{(01)}^{(\beta,\gamma)} + \frac{l_\gamma^2}{4} T_{(02)}^{(\beta,\gamma)} \tag{94}$$

$$\bar{T}_3^{+(\beta,\gamma)} = T_{(00)}^{(\beta,\gamma)} + \frac{l_\gamma}{2} T_{(01)}^{(\beta,\gamma)} + \frac{l_\gamma^2}{4} T_{(02)}^{(\beta,\gamma)} \tag{95}$$

Assembling Eqs. (92) − (95) in matrix form, we have

$$\begin{bmatrix} \bar{T}_2^+ \\ \bar{T}_2^- \end{bmatrix}^{(\beta,\gamma)} = \begin{bmatrix} \frac{h_\beta}{2} & \frac{h_\beta^2}{4} \\ -\frac{h_\beta}{2} & \frac{h_\beta^2}{4} \end{bmatrix} \begin{bmatrix} T_{(10)} \\ T_{(20)} \end{bmatrix}^{(\beta,\gamma)} + \begin{bmatrix} T_{(00)} \\ T_{(00)} \end{bmatrix}^{(\beta,\gamma)} \tag{96}$$

$$\begin{bmatrix} \bar{T}_3^+ \\ \bar{T}_3^- \end{bmatrix}^{(\beta,\gamma)} = \begin{bmatrix} \frac{l_\gamma}{2} & \frac{l_\gamma^2}{4} \\ -\frac{l_\gamma}{2} & \frac{l_\gamma^2}{4} \end{bmatrix} \begin{bmatrix} T_{(01)} \\ T_{(02)} \end{bmatrix}^{(\beta,\gamma)} + \begin{bmatrix} T_{(00)} \\ T_{(00)} \end{bmatrix}^{(\beta,\gamma)} \tag{97}$$

Adding and subtracting Eq. (92) and (93), we obtain

$$\begin{bmatrix} T_{(10)} \\ T_{(20)} \end{bmatrix}^{(\beta,\gamma)} = \begin{bmatrix} \frac{1}{h_\beta} & -\frac{1}{h_\beta} \\ \frac{2}{h_\beta^2} & \frac{2}{h_\beta^2} \end{bmatrix} \begin{bmatrix} \bar{T}_2^+ \\ \bar{T}_2^- \end{bmatrix}^{(\beta,\gamma)} - \frac{4}{h_\beta^2} \begin{bmatrix} 0 \\ T_{(00)} \end{bmatrix}^{(\beta,\gamma)} \tag{98}$$

Similarly, adding and subtracting Eq. (94) and (95), we obtain

$$\begin{bmatrix} T_{(01)} \\ T_{(02)} \end{bmatrix}^{(\beta,\gamma)} = \begin{bmatrix} \frac{1}{l_\gamma} & -\frac{1}{l_\gamma} \\ \frac{2}{l_\gamma^2} & \frac{2}{l_\gamma^2} \end{bmatrix} \begin{bmatrix} \bar{T}_3^+ \\ \bar{T}_3^- \end{bmatrix}^{(\beta,\gamma)} - \frac{4}{l_\gamma^2} \begin{bmatrix} 0 \\ T_{(00)} \end{bmatrix}^{(\beta,\gamma)} \tag{99}$$

Equations (98) and (99) relate the first and second order microvariables to the surface-averaged temperatures and the zeroth order microvariables. In order to express the first and second order microvariables solely in terms of the surface-averaged temperatures, we make use of the volume-averaged steady-state heat conduction equation.

3.2.1 Heat conduction equation

The heat flux in the material occupying the subcell (β,γ) in the region $\left|\overline{x}_2^{(\beta,\gamma)}\right| \le \frac{1}{2}h_\beta$, $\left|\overline{x}_3^{(\beta,\gamma)}\right| \le \frac{1}{2}l_\gamma$, must satisfy the steady-state heat conduction equation given by Eq. (3), reproduced here for convenience, in a volumetric sense

$$\frac{\partial q_2^{(\beta,\gamma)}}{\partial \bar{x}_2^{(\beta)}} + \frac{\partial q_3^{(\beta,\gamma)}}{\partial \bar{x}_3^{(\gamma)}} = 0 \tag{100}$$

Substituting Eqs. (76) and (77) for the heat flux in the $\bar{x}_2$ and $\bar{x}_3$ directions, respectively in the above equation, performing the required volumetric averaging and simplifying, we get

$$[k_2 T_{(20)} + k_3 T_{(02)}]^{(\beta,\gamma)} = 0 \tag{101}$$

Substituting the second-order microvariables $T_{(20)}^{(\beta,\gamma)}$ and $T_{(02)}^{(\beta,\gamma)}$ from Eqs. (98) and (99) and simplifying, we obtain

$$T_{(00)}^{(\beta,\gamma)} = \frac{k_2^{(\beta,\gamma)}}{2\bar{k}^{(\beta,\gamma)}}(\bar{T}_2^+ + \bar{T}_2^-)^{(\beta,\gamma)} + \frac{k_3^{(\beta,\gamma)} h_\beta^2}{2\bar{k}^{(\beta,\gamma)} l_\gamma^2}(\bar{T}_3^+ + \bar{T}_3^-)^{(\beta,\gamma)} \tag{102}$$

where

$$\bar{k}^{(\beta,\gamma)} = k_2^{(\beta,\gamma)} + \frac{h_\beta^2}{l_\gamma^2} k_3^{(\beta,\gamma)} \tag{103}$$

Substituting Eq. (102) into Eqs. (98) and (99) and simplifying, we obtain

$$\begin{bmatrix} T_{(10)} \\ T_{(20)} \end{bmatrix}^{(\beta,\gamma)} = \begin{bmatrix} \frac{1}{h_\beta} & -\frac{1}{h_\beta} \\ \frac{2k_3^{(\beta,\gamma)}}{l_\gamma^2 \bar{k}^{(\beta,\gamma)}} & \frac{2k_3^{(\beta,\gamma)}}{l_\gamma^2 \bar{k}^{(\beta,\gamma)}} \end{bmatrix} \begin{bmatrix} \bar{T}_2^+ \\ \bar{T}_2^- \end{bmatrix}^{(\beta,\gamma)} - \frac{2k_3^{(\beta,\gamma)}}{\bar{k}^{(\beta,\gamma)} l_\gamma^2} \begin{bmatrix} 0 & 0 \\ 1 & 1 \end{bmatrix} \begin{bmatrix} \bar{T}_3^+ \\ \bar{T}_3^- \end{bmatrix}^{(\beta,\gamma)} \tag{104}$$

$$\begin{bmatrix} T_{(01)} \\ T_{(02)} \end{bmatrix}^{(\beta,\gamma)} = \begin{bmatrix} \frac{1}{l_\gamma} & -\frac{1}{l_\gamma} \\ \frac{2k_2^{(\beta,\gamma)}}{l_\gamma^2 \bar{k}^{(\beta,\gamma)}} & \frac{2k_2^{(\beta,\gamma)}}{l_\gamma^2 \bar{k}^{(\beta,\gamma)}} \end{bmatrix} \begin{bmatrix} \bar{T}_3^+ \\ \bar{T}_3^- \end{bmatrix}^{(\beta,\gamma)} - \frac{2k_2^{(\beta,\gamma)}}{\bar{k}^{(\beta,\gamma)} l_\gamma^2} \begin{bmatrix} 0 & 0 \\ 1 & 1 \end{bmatrix} \begin{bmatrix} \bar{T}_2^+ \\ \bar{T}_2^- \end{bmatrix}^{(\beta,\gamma)} \tag{105}$$

Equations (102), (104) and (105) express the microvariables $T_{(mn)}^{(\beta,\gamma)}$ explicitly in terms of the surface-averaged temperatures. Substituting Eqs. (104) and (105) into Eqs. (86) and (87) and simplifying, we obtain the local conductivity matrix as shown below

$$\begin{bmatrix} \bar{Q}_2^+ \\ -\bar{Q}_2^- \\ \bar{Q}_3^+ \\ -\bar{Q}_3^- \end{bmatrix}^{(\beta,\gamma)} = \begin{bmatrix} \kappa_{11} & \kappa_{12} & \kappa_{13} & \kappa_{14} \\ \kappa_{21} & \kappa_{22} & \kappa_{23} & \kappa_{24} \\ \kappa_{31} & \kappa_{32} & \kappa_{33} & \kappa_{34} \\ \kappa_{41} & \kappa_{42} & \kappa_{43} & \kappa_{44} \end{bmatrix}^{(\beta,\gamma)} \begin{bmatrix} \bar{T}_2^+ \\ \bar{T}_2^- \\ \bar{T}_3^+ \\ \bar{T}_3^- \end{bmatrix}^{(\beta,\gamma)} \tag{106}$$

where

$$\begin{aligned} \kappa_{11}^{(\beta,\gamma)} &= \kappa_{22}^{(\beta,\gamma)} = -k_2^{(\beta,\gamma)} \left(\frac{1}{h_\beta} + \frac{3h_\beta k_3^{(\beta,\gamma)}}{l_\gamma^2 \bar{k}^{(\beta,\gamma)}} \right) \\ \kappa_{12}^{(\beta,\gamma)} &= \kappa_{21}^{(\beta,\gamma)} = k_2^{(\beta,\gamma)} \left(\frac{1}{h_\beta} - \frac{3h_\beta k_3^{(\beta,\gamma)}}{l_\gamma^2 \bar{k}^{(\beta,\gamma)}} \right) \\ \kappa_{13}^{(\beta,\gamma)} &= \kappa_{14}^{(\beta,\gamma)} = \kappa_{23}^{(\beta,\gamma)} = \kappa_{24}^{(\beta,\gamma)} = \frac{3h_\beta k_2^{(\beta,\gamma)} k_3^{(\beta,\gamma)}}{l_\gamma^2 \bar{k}^{(\beta,\gamma)}} \end{aligned}$$

and

$$\begin{aligned} \kappa_{33}^{(\beta,\gamma)} &= \kappa_{44}^{(\beta,\gamma)} = -k_3^{(\beta,\gamma)} \left(\frac{1}{l_\gamma} + \frac{3k_2^{(\beta,\gamma)}}{l_\gamma \bar{k}^{(\beta,\gamma)}} \right) \\ \kappa_{12}^{(\beta,\gamma)} &= \kappa_{21}^{(\beta,\gamma)} = k_3^{(\beta,\gamma)} \left(\frac{1}{l_\gamma} - \frac{3k_2^{(\beta,\gamma)}}{l_\gamma \bar{k}^{(\beta,\gamma)}} \right) \\ \kappa_{31}^{(\beta,\gamma)} &= \kappa_{32}^{(\beta,\gamma)} = \kappa_{41}^{(\beta,\gamma)} = \kappa_{42}^{(\beta,\gamma)} = \frac{3k_2^{(\beta,\gamma)} k_3^{(\beta,\gamma)}}{l_\gamma \bar{k}^{(\beta,\gamma)}} \end{aligned}$$

Therefore, we have formulated the local conductivity matrix which relates the surface-averaged heat fluxes to surface-averaged temperatures. The next step is to assemble the global conductivity matrix using the interfacial continuity conditions and the boundary conditions.

3.2.2 Temperature continuity conditions

The temperature continuity at the interfaces between adjacent subcells is applied in an average sense. Considering the β^{th} interface, which is the interface between the subcells (β, γ) and $(\beta+1, \gamma)$, the surface-averaged temperatures in the x_2 direction, $\bar{T}_2^{+(\beta,\gamma)}$ and $\bar{T}_2^{-(\beta+1,\gamma)}$, must be equal. Hence, we can represent them using just one variable, i.e.

$$\bar{T}_2^{+(\beta,\gamma)} = \bar{T}_2^{-(\beta+1,\gamma)} = \bar{T}_2^{(\beta+1,\gamma)} \tag{107}$$

Similarly, considering the γ^{th} interface, which is the interface between the subcells (β, γ) and $(\beta, \gamma+1)$, and applying the temperature continuity in the x_3 direction

$$\bar{T}_3^{+(\beta,\gamma)} = \bar{T}_3^{-(\beta,\gamma+1)} = \bar{T}_3^{(\beta,\gamma+1)} \tag{108}$$

Equations (107) and (108) are similar to the temperature continuity conditions (19)−(22) in Section 2. Equations (107) and (108) hold true for $\beta = 1, ..., N_\beta - 1$ and $\gamma = 1, ..., N_\gamma - 1$, respectively. This gives rise to $(N_\beta - 1)N_\gamma + (N_\gamma - 1)N_\beta$ unknown surface-averaged temperatures defined at the subcell interfaces (both in x_2 and x_3 direction). The quantities

$$\bar{T}_2^{(1,\gamma)},\ \bar{T}_2^{\left(N_\beta+1,\gamma\right)},\ \bar{T}_3^{(\beta,1)},\ \bar{T}_3^{(\beta,N_\gamma+1)}$$

define the surface-averaged temperatures at the external boundaries of the composite. These quantities are either known or unknown depending on whether the temperature or heat flux is defined at the external boundaries.

3.2.3 Heat flux continuity conditions

The heat flux continuity at the interfaces between adjacent subcells is applied in an average sense. Considering the β^{th} interface and applying the heat flux continuity in the x_2 direction

$$\bar{Q}_2^{+(\beta,\gamma)} - \bar{Q}_2^{-(\beta+1,\gamma)} = 0 \tag{109}$$

where $\bar{Q}_2^{+(\beta,\gamma)}$ is the surface-averaged heat flux going out of the right face ($\overline{x}_2 = h_\beta/2$) of the subcell (β, γ) and $\bar{Q}_2^{-(\beta+1,\gamma)}$ is the surface-averaged heat flux entering into the left face ($x_2 = -h_{\beta+1}/2$) of the subcell $(\beta+1, \gamma)$ defined by Eqs. (79) and (78) respectively. Similarly, considering the γ^{th} interface and applying the heat flux continuity in the x_3 direction

$$\bar{Q}_3^{+(\beta,\gamma)} - \bar{Q}_3^{-(\beta,\gamma+1)} = 0 \tag{110}$$

Equations (109) and (110) are similar to the heat flux continuity conditions (11) − (14). Using the local conductivity matrix (106), Eqs. (109) and (110) can be expressed in terms of the surface-averaged temperatures

$$\begin{aligned}&\kappa_{11}^{(\beta,\gamma)}\bar{T}_2^{+(\beta,\gamma)} + \kappa_{12}^{(\beta,\gamma)}\bar{T}_2^{-(\beta,\gamma)} + \kappa_{13}^{(\beta,\gamma)}\bar{T}_3^{+(\beta,\gamma)} + \kappa_{14}^{(\beta,\gamma)}\bar{T}_3^{-(\beta,\gamma)} + \kappa_{21}^{(\beta+1,\gamma)}\bar{T}_2^{+(\beta+1,\gamma)} + \\ &\kappa_{22}^{(\beta+1,\gamma)}\bar{T}_2^{-(\beta+1,\gamma)} + \kappa_{23}^{(\beta+1,\gamma)}\bar{T}_3^{+(\beta+1,\gamma)} + \kappa_{24}^{(\beta+1,\gamma)}\bar{T}_3^{-(\beta+1,\gamma)} = 0\end{aligned} \tag{111}$$

$$\begin{aligned}&\kappa_{31}^{(\beta,\gamma)}\bar{T}_2^{+(\beta,\gamma)} + \kappa_{32}^{(\beta,\gamma)}\bar{T}_2^{-(\beta,\gamma)} + \kappa_{33}^{(\beta,\gamma)}\bar{T}_3^{+(\beta,\gamma)} + \kappa_{34}^{(\beta,\gamma)}\bar{T}_3^{-(\beta,\gamma)} + \kappa_{41}^{(\beta,\gamma+1)}\bar{T}_2^{+(\beta,\gamma+1)} + \\ &\kappa_{42}^{(\beta,\gamma+1)}\bar{T}_2^{-(\beta,\gamma+1)} + \kappa_{43}^{(\beta,\gamma+1)}\bar{T}_3^{+(\beta,\gamma+1)} + \kappa_{44}^{(\beta,\gamma+1)}\bar{T}_3^{-(\beta,\gamma+1)} = 0\end{aligned} \tag{112}$$

Using the temperature continuity conditions given by Eqs. (107) and (108), Eqs. (111) and (112) can be simplified and written in terms of the common interfacial surface-averaged temperatures

$$\kappa_{12}^{(\beta,\gamma)}\bar{T}_2^{(\beta,\gamma)} + (\kappa_{11}^{(\beta,\gamma)} + \kappa_{22}^{(\beta+1,\gamma)})\bar{T}_2^{(\beta+1,\gamma)} + \kappa_{21}^{(\beta+1,\gamma)}\bar{T}_2^{(\beta+2,\gamma)} + \kappa_{14}^{(\beta,\gamma)}\bar{T}_3^{(\beta,\gamma)} + \kappa_{13}^{(\beta,\gamma)}\bar{T}_3^{(\beta,\gamma+1)} + \kappa_{24}^{(\beta,\gamma)}\bar{T}_3^{(\beta+1,\gamma)} + \kappa_{23}^{(\beta+1,\gamma)}\bar{T}_3^{(\beta+1,\gamma+1)} = 0 \tag{113}$$

$$\kappa_{32}^{(\beta,\gamma)}\bar{T}_2^{(\beta,\gamma)} + \kappa_{31}^{(\beta,\gamma)}\bar{T}_2^{(\beta+1,\gamma)} + \kappa_{42}^{(\beta,\gamma+1)}\bar{T}_2^{(\beta,\gamma+1)} + \kappa_{41}^{(\beta,\gamma+1)}\bar{T}_2^{(\beta+1,\gamma+1)} + \kappa_{34}^{(\beta,\gamma)}\bar{T}_3^{(\beta,\gamma)} + (\kappa_{33}^{(\beta,\gamma)} + \kappa_{44}^{(\beta,\gamma+1)})\bar{T}_3^{(\beta,\gamma+1)} + \kappa_{43}^{(\beta,\gamma+1)}\bar{T}_3^{(\beta,\gamma+2)} = 0 \tag{114}$$

Thus, Eqs. (113) and (114) provide us with a total of $(N_\beta - 1)N_\gamma + (N_\gamma - 1)N_\beta$ equations in terms of the common interfacial surface-averaged temperatures and the surface-averaged temperatures at the external boundaries.

3.2.4 Boundary conditions

At the external boundaries of the composite, we have $2(N_\beta + N_\gamma)$ faces of the subcells where either the heat flux or the temperatures are defined. This gives rise to additional $2(N_\beta + N_\gamma)$ unknown surface-averaged quantities. The additional $2(N_\beta + N_\gamma)$ equations are obtained from the imposed boundary conditions given by

$$\bar{T}_2^{(1,\gamma)} = T_{left}^{(\gamma)}(x_3) \tag{115}$$

$$\bar{T}_2^{(N_\beta,\gamma)} = T_{right}^{(\gamma)}(x_3) \tag{116}$$

where $T_{left}^{(\gamma)}(x_3)$, and $T_{right}^{(\gamma)}(x_3)$ are the piece-wise uniform applied temperatures on the external boundaries in the $x_2 - x_3$ plane. Similar reasoning holds for subcells $(\beta, 1)$, and (β, N_γ) and the applied boundary conditions are given by

$$\bar{T}_3^{(\beta,1)} = T_{bottom}^{(\beta)}(x_2) \tag{117}$$

$$\bar{T}_3^{(\beta,N_\gamma)} = T_{top}^{(\beta)}(x_2) \tag{118}$$

If the heat flux at any of the boundaries is defined instead of temperatures, Eqs. $(115) - (118)$ are modified accordingly.

Note that, at least one $\bar{T}_2^{(\cdot)}$ and at least one $\bar{T}_3^{(\cdot)}$ at the external boundary need to be defined in order to prevent matrix singularity. If only heat flux is defined at the external boundaries, theoretically it gives rise to the possibility of having more than one temperature distribution. This is analogous to the rigid body motion if only tractions are defined at the external boundaries and not a single point is fixed in space.

3.2.5 Solution for the surface-averaged temperatures

Equations (113) and (114) together with the imposed boundary conditions (Eqs. $(115) - (118)$) provide us with the necessary $(N_\beta + 1)N_\gamma + (N_\gamma + 1)N_\beta$ relations for $(N_\beta + 1)N_\gamma + (N_\gamma + 1)N_\beta$ unknown surface-averaged variables (i.e., $(N_\beta - 1)N_\gamma + (N_\gamma - 1)N_\beta$ unknown common interfacial surface-averaged temperatures along with $2(N_\beta + N_\gamma)$ unknown surface-averaged temperatures and/or heat fluxes at the external boundaries).

The final system of equations is symbolically written as

$$\boldsymbol{\kappa}\ \bar{\mathbf{T}} = \bar{\mathbf{Q}} \tag{119}$$

In the above equation, $\boldsymbol{\kappa}$ is the global thermal conductivity matrix obtained after assembling the local conductivity matrices given by Eq. (106) using the local-global conductivity matrix approach as explained above. The matrix $\boldsymbol{\kappa}$ essentially contains information on the geometry and thermal conductivities of the individual $N_\beta N_\gamma$ subcells. The general format and assembly of the global thermal conductivity matrix $\boldsymbol{\kappa}$ has been summarized in the next subsection. The vector $\bar{\mathbf{T}}$ contains the unknown surface-averaged temperatures at the subcell interfaces and the surface-averaged temperatures at the outer edges of the composite (some of which are known), and is given by

$$\bar{\mathbf{T}} = [\bar{\mathbf{T}}_2^{(1)}, ..., \bar{\mathbf{T}}_2^{(N_\gamma)}, \bar{\mathbf{T}}_3^{(1)}, ..., \bar{\mathbf{T}}_3^{(N_\beta)}]$$

where

$$\bar{\mathbf{T}}_2^{(\gamma)} = [\bar{T}_2^{(1,\gamma)}, ..., \bar{T}_2^{(N_\beta+1,\gamma)}] \qquad \bar{\mathbf{T}}_3^{(\beta)} = [\bar{T}_3^{(1,\beta)}, ..., \bar{T}_3^{(N_\beta+1,\beta)}]$$

The surface-averaged heat flux vector $\bar{\mathbf{Q}}$ contains information about the piece-wise uniform heat fluxes defined at the external boundaries of the composite and consists mainly of zeros which are obtained after applying the interfacial heat flux continuity. It is given by

$$\bar{\mathbf{Q}} = [\bar{\mathbf{Q}}_2^{(1)}, ..., \bar{\mathbf{Q}}_2^{(N_\gamma)}, \bar{\mathbf{Q}}_3^{(1)}, ..., \bar{\mathbf{Q}}_3^{(N_\beta)}]$$

where

$$\bar{\mathbf{Q}}_2^{(\gamma)} = [\bar{Q}_2^{(1,\gamma)}, 0, ..., 0, \bar{Q}_2^{(N_\beta+1,\gamma)}] \qquad \bar{\mathbf{Q}}_3^{(\beta)} = [\bar{Q}_3^{(1,\beta)}, 0, ..., 0, \bar{Q}_3^{(N_\beta+1,\beta)}]$$

Once Eq. (119) is solved for the surface-averaged temperatures at all the subcell interfaces and external boundaries, we substitute the surface-averaged temperatures back into Eqs. (102), (98) and (99), and obtain the microvariables $T_{(mn)}^{(\beta,\gamma)}$ which define the temperature field in each subcell.

3.2.6 Assembly of the global thermal conductivity matrix $\boldsymbol{\kappa}$

The general format and assembly of the global conductivity matrix $\boldsymbol{\kappa}$ is summarized in this subsection. $\boldsymbol{\kappa}$ consists of four submatrices

$$\boldsymbol{\kappa} = \begin{bmatrix} \boldsymbol{\kappa}_{11} & \boldsymbol{\kappa}_{12} \\ \boldsymbol{\kappa}_{21} & \boldsymbol{\kappa}_{22} \end{bmatrix}$$

where $\boldsymbol{\kappa}_{11}$ and $\boldsymbol{\kappa}_{22}$ relate the quantities in their respective directions and have entries concentrated along the diagonal.The submatrices $\boldsymbol{\kappa}_{12}$ and $\boldsymbol{\kappa}_{21}$ represent the coupling of field variables in the x_2 and x_3 direction and have entries scattered throughout. The global thermal conductivity matrix $\boldsymbol{\kappa}$ is a square matrix of size $[N_\beta(N_\gamma+1)+N_\gamma(N_\beta+1) \times N_\beta(N_\gamma+1)+N_\gamma(N_\beta+1)]$. The structure of the submatrix $\boldsymbol{\kappa}_{11}$ is shown below

$$\boldsymbol{\kappa}_{11} = \begin{bmatrix} \mathbf{A}_2^{(1)} & \mathbf{0} & \mathbf{0} & \mathbf{0} & \mathbf{0} & \mathbf{0} & \mathbf{0} & \mathbf{0} \\ \mathbf{0} & \mathbf{A}_2^{(2)} & \mathbf{0} & \mathbf{0} & \mathbf{0} & \mathbf{0} & \mathbf{0} & \mathbf{0} \\ \mathbf{0} & \mathbf{0} & . & \mathbf{0} & \mathbf{0} & \mathbf{0} & \mathbf{0} & \mathbf{0} \\ \mathbf{0} & \mathbf{0} & \mathbf{0} & . & \mathbf{0} & \mathbf{0} & \mathbf{0} & \mathbf{0} \\ \mathbf{0} & \mathbf{0} & \mathbf{0} & \mathbf{0} & . & \mathbf{0} & \mathbf{0} & \mathbf{0} \\ \mathbf{0} & \mathbf{0} & \mathbf{0} & \mathbf{0} & \mathbf{0} & . & \mathbf{0} & \mathbf{0} \\ \mathbf{0} & \mathbf{0} & \mathbf{0} & \mathbf{0} & \mathbf{0} & \mathbf{0} & . & \mathbf{0} \\ \mathbf{0} & \mathbf{0} & \mathbf{0} & \mathbf{0} & \mathbf{0} & \mathbf{0} & \mathbf{0} & \mathbf{A}_2^{(N_\gamma)} \end{bmatrix}$$

where the size of $\boldsymbol{\kappa}_{11}$ is $[N_\gamma(N_\beta+1) \times N_\gamma(N_\beta+1)]$. The structure of the submatrices $\mathbf{A}_2^{(\gamma)}$ is shown in the appendix. The structure of $\boldsymbol{\kappa}_{22}$ is similar to $\boldsymbol{\kappa}_{11}$. The structure of the coupling matrix $\boldsymbol{\kappa}_{12}$ is shown below

$$\boldsymbol{\kappa}_{12} = \begin{bmatrix} \mathbf{B}_2^{(11)} & \mathbf{B}_2^{(12)} & . & . & . & . & . & \mathbf{B}_2^{(1N_\beta)} \\ \mathbf{B}_2^{(21)} & \mathbf{B}_2^{(22)} & . & . & . & . & . & \mathbf{B}_2^{(2N_\beta)} \\ . & . & . & . & . & . & . & . \\ . & . & . & . & . & . & . & . \\ . & . & . & . & . & . & . & . \\ . & . & . & . & . & . & . & . \\ . & . & . & . & . & . & . & . \\ \mathbf{B}_2^{(N_\gamma 1)} & \mathbf{B}_2^{(N_\gamma 2)} & . & . & . & . & . & \mathbf{B}_2^{(N_\gamma N_\beta)} \end{bmatrix}$$

where the size of $\boldsymbol{\kappa}_{12}$ is $[N_\gamma(N_\beta+1) \times N_\beta(N_\gamma+1)]$. The structure of the submatrices $\mathbf{B}_2^{(\gamma\beta)}$ is shown in the appendix. The structure of $\boldsymbol{\kappa}_{21}$ is similar to $\boldsymbol{\kappa}_{12}$.

3.3 Mechanical Reformulation

The displacement field in the subcell (β,γ) of the composite functionally graded in $x_2 - x_3$ plane is approximated by the same second-order polynomial expansion in the local coordinates $\bar{x}_2^{(\beta)}$, and $\bar{x}_3^{(\gamma)}$ as that given by Eqs. $(32)-(34)$ in Section 2, reproduced below for convenience

$$u_1^{(\beta,\gamma)} = x_1 \bar{\varepsilon}_{11} \tag{120}$$

$$u_2^{(\beta,\gamma)} = W_{2(00)}^{(\beta,\gamma)} + \overline{x}_2^{(\beta)} W_{2(10)}^{(\beta,\gamma)} + \overline{x}_3^{(\gamma)} W_{2(01)}^{(\beta,\gamma)} + \frac{1}{2}(3\overline{x}_2^{(\beta)2} - \frac{h_\beta^2}{4}) W_{2(20)}^{(\beta,\gamma)} + \frac{1}{2}(3\overline{x}_3^{(\gamma)2} - \frac{l_\gamma^2}{4}) W_{2(02)}^{(\beta,\gamma)} \tag{121}$$

$$u_3^{(\beta,\gamma)} = W_{3(00)}^{(\beta,\gamma)} + \overline{x}_2^{(\beta)} W_{3(10)}^{(\beta,\gamma)} + \overline{x}_3^{(\gamma)} W_{3(01)}^{(\beta,\gamma)} + \frac{1}{2}(3\overline{x}_2^{(\beta)2} - \frac{h_\beta^2}{4}) W_{3(20)}^{(\beta,\gamma)} + \frac{1}{2}(3\overline{x}_3^{(\gamma)2} - \frac{l_\gamma^2}{4}) W_{3(02)}^{(\beta,\gamma)} \tag{122}$$

For plane deformation (plane strain) case

$$\bar{\varepsilon}_{11} = 0 \tag{123}$$

and for generalized plane strain, $\bar{\varepsilon}_{11}$ is determined from the condition

$$\sum_{\gamma=1}^{N_\beta} \sum_{\beta=1}^{N_\beta} \int_{-h_\beta/2}^{h_\beta/2} \int_{-l_\gamma/2}^{l_\gamma/2} \sigma_{ij}^{(\beta,\gamma)} d\bar{x}_2^{(\beta)} d\bar{x}_3^{(\gamma)} = 0 \tag{124}$$

For an orthotropic elastic material occupying the subcell (β,γ), the stress components are related to the strain components through the familiar Hooke's law

$$\sigma_{ij}^{(\beta,\gamma)} = C_{ijkl}^{(\beta,\gamma)} \varepsilon_{kl}^{(\beta,\gamma)} - \sigma_{ij}^{T(\beta,\gamma)} \tag{125}$$

$C_{ijkl}^{(\beta,\gamma)}$ are the stiffness tensor elements for the material occupying the subcell (β,γ), $\varepsilon_{ij}^{(\beta,\gamma)}$ are the elastic strain components, and $\sigma_{ij}^{T(\alpha\beta\gamma)}$ are the components of thermal stress vector given by

$$\sigma_{ij}^{T(\beta,\gamma)} = \Gamma_{ij}^{(\beta,\gamma)} T^{(\beta,\gamma)} \tag{126}$$

where $\Gamma_{ij}^{(\beta,\gamma)}$ is the product of the stiffness tensor components and thermal expansion coefficients $\alpha_{ij}^{(\beta,\gamma)}$, and $T^{(\beta,\gamma)}$ represents the temperature change at a particular location in the composite.

The components of the strain tensor in the individual subcells are obtained from the strain-displacement relations,

$$\varepsilon_{ij}^{(\beta,\gamma)} = \frac{1}{2}\left(\frac{\partial u_j^{(\beta,\gamma)}}{\partial \bar{x}_i^{(\cdot)}} + \frac{\partial u_i^{(\beta,\gamma)}}{\partial \bar{x}_j^{(\cdot)}}\right) \tag{127}$$

Substituting Eqs. (121) and (122) into Eq. (127) and simplifying, we get

$$\varepsilon_{22}^{(\beta,\gamma)} = W_{2(10)}^{(\beta,\gamma)} + 3\overline{x}_2^{(\beta)} W_{2(20)}^{(\beta,\gamma)} \tag{128}$$

$$\varepsilon_{33}^{(\beta,\gamma)} = W_{3(01)}^{(\beta,\gamma)} + 3\overline{x}_2^{(\beta)} W_{3(02)}^{(\beta,\gamma)} \tag{129}$$

$$\varepsilon_{23}^{(\beta,\gamma)} = \frac{1}{2}[W_{2(01)}^{(\beta,\gamma)} + 3\overline{x}_3^{(\gamma)} W_{2(02)}^{(\beta,\gamma)} + W_{3(10)}^{(\beta,\gamma)} + 3\overline{x}_2^{(\beta)} W_{3(20)}^{(\beta,\gamma)}] \tag{130}$$

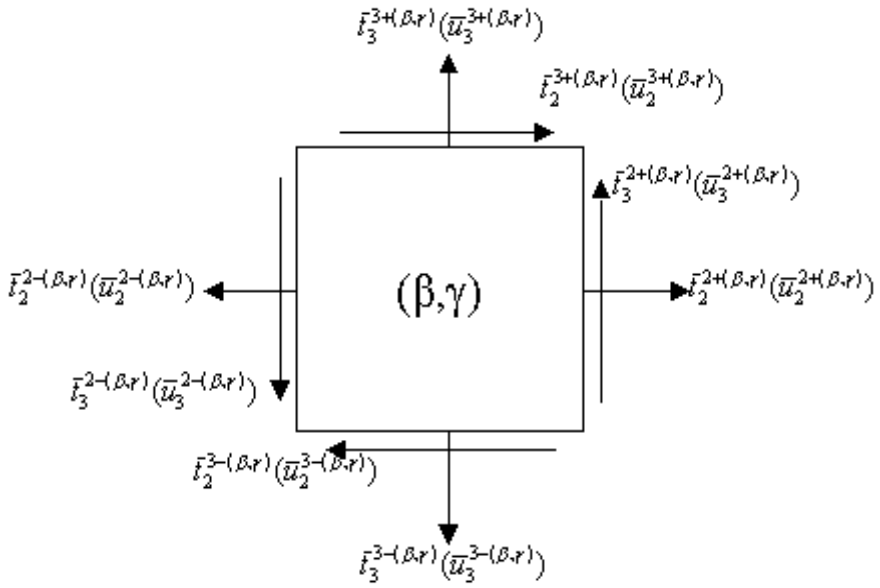

Fig. 5. Schematic of a subcell (β,γ) showing the surface averaged tractions and displacements defined in the reformulated HOTFGM-2D.

The local stiffness matrix relates the surface-averaged tractions to the surface-averaged displacements on the subcell's faces as shown in Fig. 5. The surface-averaged tractions are determined using the familiar expressions for tractions given in terms of the stress components

$$t_i^{\mathbf{n}(\beta,\gamma)} = \sigma_{ji}^{(\beta,\gamma)} n_j^{(\beta,\gamma)} \tag{131}$$

where $n_j^{(\beta,\gamma)}$ are the components of the unit vector normal to the face of the (β,γ) subcell. At the left face of the subcell (β,γ), the surface-averaged tractions $\bar{t}_2^{2-(\beta,\gamma)}$ and $\bar{t}_3^{2-(\beta,\gamma)}$ are defined as

$$\bar{t}_2^{2-(\beta,\gamma)} = \frac{1}{l_\gamma}\int_{-l_\gamma/2}^{l_\gamma/2} t_2^{\mathbf{n}(\beta,\gamma)}\left(-\frac{h_\beta}{2}, \bar{x}_3^{(\gamma)}\right) d\bar{x}_3^{(\gamma)} \tag{132}$$

$$\bar{t}_3^{2-(\beta,\gamma)} = \frac{1}{l_\gamma}\int_{-l_\gamma/2}^{l_\gamma/2} t_3^{\mathbf{n}(\beta,\gamma)}\left(-\frac{h_\beta}{2}, \bar{x}_3^{(\gamma)}\right) d\bar{x}_3^{(\gamma)} \tag{133}$$

Similarly, surface-averaged tractions at the right face of the subcell (β,γ) are defined as

$$\bar{t}_2^{2+(\beta,\gamma)} = \frac{1}{l_\gamma}\int_{-l_\gamma/2}^{l_\gamma/2} t_2^{\mathbf{n}(\beta,\gamma)}(\frac{h_\beta}{2},\bar{x}_3^{(\gamma)})d\bar{x}_3^{(\gamma)} \tag{134}$$

$$\bar{t}_3^{2+(\beta,\gamma)} = \frac{1}{l_\gamma}\int_{-l_\gamma/2}^{l_\gamma/2} t_3^{\mathbf{n}(\beta,\gamma)}(\frac{h_\beta}{2},\bar{x}_3^{(\gamma)})d\bar{x}_3^{(\gamma)} \tag{135}$$

Surface averaged tractions at the bottom face of the subcell (β,γ) are defined as

$$\bar{t}_2^{3-(\beta,\gamma)} = \frac{1}{h_\beta}\int_{-h_\beta/2}^{h_\beta/2} t_2^{\mathbf{n}(\beta,\gamma)}(\bar{x}_2^{(\beta)},-\frac{l_\gamma}{2})d\bar{x}_2^{(\beta)} \tag{136}$$

$$\bar{t}_3^{3-(\beta,\gamma)} = \frac{1}{h_\beta}\int_{-h_\beta/2}^{h_\beta/2} t_3^{\mathbf{n}(\beta,\gamma)}(\bar{x}_2^{(\beta)},-\frac{l_\gamma}{2})d\bar{x}_2^{(\beta)} \tag{137}$$

Surface averaged tractions at the top face of the subcell (β,γ) are defined as

$$\bar{t}_2^{3+(\beta,\gamma)} = \frac{1}{h_\beta}\int_{-h_\beta/2}^{h_\beta/2} t_2^{\mathbf{n}(\beta,\gamma)}(\bar{x}_2^{(\beta)},\frac{l_\gamma}{2})d\bar{x}_2^{(\beta)} \tag{138}$$

$$\bar{t}_3^{3+(\beta,\gamma)} = \frac{1}{h_\beta}\int_{-h_\beta/2}^{h_\beta/2} t_3^{\mathbf{n}(\beta,\gamma)}(\bar{x}_2^{(\beta)},\frac{l_\gamma}{2})d\bar{x}_2^{(\beta)} \tag{139}$$

Substituting Eqs. (131), (125), (126), and $(128)-(130)$ into Eqs. $(132)-(139)$, performing the required integration and assembling the resulting equations for the surface-averaged tractions in matrix form, we get

$$\begin{bmatrix} \bar{t}_2^{2+} \\ \bar{t}_2^{2-} \end{bmatrix}^{(\beta,\gamma)} = C_{22}^{(\beta,\gamma)} \begin{bmatrix} 1 & \frac{3h_\beta}{2} \\ -1 & \frac{3h_\beta}{2} \end{bmatrix} \begin{bmatrix} W_{2(10)} \\ W_{2(20)} \end{bmatrix}^{(\beta,\gamma)} + C_{23}^{(\beta,\gamma)} \begin{bmatrix} W_{3(01)} \\ -W_{3(01)} \end{bmatrix}^{(\beta,\gamma)} - (C_{12}\alpha_{11}+C_{22}\alpha_{22}+C_{23}\alpha_{33})^{(\beta,\gamma)} \begin{bmatrix} \bar{T}_2^{+} \\ -\bar{T}_2^{-} \end{bmatrix}^{(\beta,\gamma)} \tag{140}$$

$$\begin{bmatrix} \bar{t}_3^{2+} \\ \bar{t}_3^{2-} \end{bmatrix}^{(\beta,\gamma)} = C_{44}^{(\beta,\gamma)} \begin{bmatrix} 1 & \frac{3h_\beta}{2} \\ -1 & \frac{3h_\beta}{2} \end{bmatrix} \begin{bmatrix} W_{3(10)} \\ W_{3(20)} \end{bmatrix}^{(\beta,\gamma)} + C_{44}^{(\beta,\gamma)} \begin{bmatrix} W_{2(01)} \\ -W_{2(01)} \end{bmatrix}^{(\beta,\gamma)} \tag{141}$$

$$\begin{bmatrix} \bar{t}_3^{3+} \\ \bar{t}_3^{3-} \end{bmatrix}^{(\beta,\gamma)} = C_{33}^{(\beta,\gamma)} \begin{bmatrix} 1 & \frac{3l_\gamma}{2} \\ -1 & \frac{3l_\gamma}{2} \end{bmatrix} \begin{bmatrix} W_{3(01)} \\ W_{3(02)} \end{bmatrix}^{(\beta,\gamma)} + C_{23}^{(\beta,\gamma)} \begin{bmatrix} W_{2(10)} \\ -W_{2(10)} \end{bmatrix}^{(\beta,\gamma)} - (C_{13}\alpha_{11}+C_{23}\alpha_{22}+C_{33}\alpha_{33})^{(\beta,\gamma)} \begin{bmatrix} \bar{T}_3^{+} \\ -\bar{T}_3^{-} \end{bmatrix}^{(\beta,\gamma)} \tag{142}$$

$$\begin{bmatrix} \bar{t}_2^{3+} \\ \bar{t}_2^{3-} \end{bmatrix}^{(\beta,\gamma)} = C_{44}^{(\beta,\gamma)} \begin{bmatrix} 1 & \frac{3l_\gamma}{2} \\ -1 & \frac{3l_\gamma}{2} \end{bmatrix} \begin{bmatrix} W_{2(01)} \\ W_{2(02)} \end{bmatrix}^{(\beta,\gamma)} + C_{44}^{(\beta,\gamma)} \begin{bmatrix} W_{3(10)} \\ -W_{3(10)} \end{bmatrix}^{(\beta,\gamma)} \tag{143}$$

Equations $(140)-(143)$ relate the surface-averaged tractions to the first and second order microvariables that determine the displacement field within the subcell (β,γ). We need to relate these microvariables to the surface-averaged displacements, and surface-averaged temperatures obtained after solving the thermal problem, in order to formulate the local stiffness matrix. Hence, we

proceed to define the surface-averaged displacements. At the left face of the subcell (β,γ), the surface-averaged displacements $\bar{u}_2^{2-(\beta,\gamma)}$ and $\bar{u}_3^{2-(\beta,\gamma)}$ are defined as

$$\bar{u}_2^{2-(\beta,\gamma)} = \frac{1}{l_\gamma}\int_{-l_\gamma/2}^{l_\gamma/2} u_2^{(\beta,\gamma)}(-\frac{h_\beta}{2}, \bar{x}_3^{(\gamma)})d\bar{x}_3^{(\gamma)} \tag{144}$$

$$\bar{u}_3^{2-(\beta,\gamma)} = \frac{1}{l_\gamma}\int_{-l_\gamma/2}^{l_\gamma/2} u_3^{(\beta,\gamma)}(-\frac{h_\beta}{2}, \bar{x}_3^{(\gamma)})d\bar{x}_3^{(\gamma)} \tag{145}$$

Similarly, surface-averaged displacements at the right face of the subcell (β,γ) are defined as

$$\bar{u}_2^{2+(\beta,\gamma)} = \frac{1}{l_\gamma}\int_{-l_\gamma/2}^{l_\gamma/2} u_2^{(\beta,\gamma)}(\frac{h_\beta}{2}, \bar{x}_3^{(\gamma)})d\bar{x}_3^{(\gamma)} \tag{146}$$

$$\bar{u}_3^{2+(\beta,\gamma)} = \frac{1}{l_\gamma}\int_{-l_\gamma/2}^{l_\gamma/2} u_3^{(\beta,\gamma)}(\frac{h_\beta}{2}, \bar{x}_3^{(\gamma)})d\bar{x}_3^{(\gamma)} \tag{147}$$

Surface averaged displacements at the bottom face of the subcell (β,γ) are defined as

$$\bar{u}_2^{3-(\beta,\gamma)} = \frac{1}{h_\beta}\int_{-h_\beta/2}^{h_\beta/2} u_2^{(\beta,\gamma)}(\bar{x}_2^{(\beta)}, -\frac{l_\gamma}{2})d\bar{x}_2^{(\beta)} \tag{148}$$

$$\bar{u}_3^{3-(\beta,\gamma)} = \frac{1}{h_\beta}\int_{-h_\beta/2}^{h_\beta/2} u_3^{(\beta,\gamma)}(\bar{x}_2^{(\beta)}, -\frac{l_\gamma}{2})d\bar{x}_2^{(\beta)} \tag{149}$$

Surface averaged displacements at the top face of the subcell (β,γ) are defined as

$$\bar{u}_2^{3+(\beta,\gamma)} = \frac{1}{h_\beta}\int_{-h_\beta/2}^{h_\beta/2} u_2^{(\beta,\gamma)}(\bar{x}_2^{(\beta)}, \frac{l_\gamma}{2})d\bar{x}_2^{(\beta)} \tag{150}$$

$$\bar{u}_3^{3+(\beta,\gamma)} = \frac{1}{h_\beta}\int_{-h_\beta/2}^{h_\beta/2} u_3^{(\beta,\gamma)}(\bar{x}_2^{(\beta)}, \frac{l_\gamma}{2})d\bar{x}_2^{(\beta)} \tag{151}$$

Substituting the expressions for $u_i^{(\beta,\gamma)}$ given by Eqs. (121) and (122), and performing the above averaging procedure, we obtain

$$\bar{u}_2^{2-(\beta,\gamma)} = W_{2(00)}^{(\beta,\gamma)} - \frac{h_\beta}{2}W_{2(10)}^{(\beta,\gamma)} + \frac{h_\beta^2}{4}W_{2(20)}^{(\beta,\gamma)} \tag{152}$$

$$\bar{u}_3^{2-(\beta,\gamma)} = W_{3(00)}^{(\beta,\gamma)} - \frac{h_\beta}{2}W_{3(10)}^{(\beta,\gamma)} + \frac{h_\beta^2}{4}W_{3(20)}^{(\beta,\gamma)} \tag{153}$$

$$\bar{u}_2^{2+(\beta,\gamma)} = W_{2(00)}^{(\beta,\gamma)} + \frac{h_\beta}{2}W_{2(10)}^{(\beta,\gamma)} + \frac{h_\beta^2}{4}W_{2(20)}^{(\beta,\gamma)} \tag{154}$$

$$\bar{u}_3^{2+(\beta,\gamma)} = W_{3(00)}^{(\beta,\gamma)} + \frac{h_\beta}{2}W_{3(10)}^{(\beta,\gamma)} + \frac{h_\beta^2}{4}W_{3(20)}^{(\beta,\gamma)} \tag{155}$$

$$\bar{u}_2^{3-(\beta,\gamma)} = W_{2(00)}^{(\beta,\gamma)} - \frac{l_\gamma}{2}W_{2(01)}^{(\beta,\gamma)} + \frac{l_\gamma^2}{4}W_{2(02)}^{(\beta,\gamma)} \tag{156}$$

$$\bar{u}_3^{3-(\beta,\gamma)} = W_{3(00)}^{(\beta,\gamma)} - \frac{l_\gamma}{2}W_{3(01)}^{(\beta,\gamma)} + \frac{l_\gamma^2}{4}W_{3(02)}^{(\beta,\gamma)} \tag{157}$$

$$\bar{u}_2^{3+(\beta,\gamma)} = W_{2(00)}^{(\beta,\gamma)} + \frac{l_\gamma}{2}W_{2(01)}^{(\beta,\gamma)} + \frac{l_\gamma^2}{4}W_{2(02)}^{(\beta,\gamma)} \tag{158}$$

$$\bar{u}_3^{3+(\beta,\gamma)} = W_{3(00)}^{(\beta,\gamma)} + \frac{l_\gamma}{2}W_{3(01)}^{(\beta,\gamma)} + \frac{l_\gamma^2}{4}W_{3(02)}^{(\beta,\gamma)} \tag{159}$$

Assembling Eqs. (152) − (159) for the surface-averaged displacements in matrix form

$$\left[\begin{array}{c} \bar{u}_2^{2+} \\ \bar{u}_2^{2-} \end{array}\right]^{(\beta,\gamma)} = \left[\begin{array}{cc} \frac{h_\beta}{2} & \frac{h_\beta^2}{4} \\ -\frac{h_\beta}{2} & \frac{h_\beta^2}{4} \end{array}\right] \left[\begin{array}{c} W_{2(10)} \\ W_{2(20)} \end{array}\right]^{(\beta,\gamma)} + \left[\begin{array}{c} W_{2(00)} \\ W_{2(00)} \end{array}\right]^{(\beta,\gamma)} \tag{160}$$

$$\left[\begin{array}{c} \bar{u}_3^{2+} \\ \bar{u}_3^{2-} \end{array}\right]^{(\beta,\gamma)} = \left[\begin{array}{cc} \frac{h_\beta}{2} & \frac{h_\beta^2}{4} \\ -\frac{h_\beta}{2} & \frac{h_\beta^2}{4} \end{array}\right] \left[\begin{array}{c} W_{3(10)} \\ W_{3(20)} \end{array}\right]^{(\beta,\gamma)} + \left[\begin{array}{c} W_{3(00)} \\ W_{3(00)} \end{array}\right]^{(\beta,\gamma)} \tag{161}$$

$$\left[\begin{array}{c} \bar{u}_3^{3+} \\ \bar{u}_3^{3-} \end{array}\right]^{(\beta,\gamma)} = \left[\begin{array}{cc} \frac{l_\gamma}{2} & \frac{l_\gamma^2}{4} \\ -\frac{l_\gamma}{2} & \frac{l_\gamma^2}{4} \end{array}\right] \left[\begin{array}{c} W_{3(01)} \\ W_{3(02)} \end{array}\right]^{(\beta,\gamma)} + \left[\begin{array}{c} W_{3(00)} \\ W_{3(00)} \end{array}\right]^{(\beta,\gamma)} \tag{162}$$

$$\left[\begin{array}{c} \bar{u}_2^{3+} \\ \bar{u}_2^{3-} \end{array}\right]^{(\beta,\gamma)} = \left[\begin{array}{cc} \frac{l_\gamma}{2} & \frac{l_\gamma^2}{4} \\ -\frac{l_\gamma}{2} & \frac{l_\gamma^2}{4} \end{array}\right] \left[\begin{array}{c} W_{2(01)} \\ W_{2(02)} \end{array}\right]^{(\beta,\gamma)} + \left[\begin{array}{c} W_{2(00)} \\ W_{2(00)} \end{array}\right]^{(\beta,\gamma)} \tag{163}$$

Adding and subtracting Eqs. (152) and (154), we get

$$\left[\begin{array}{c} W_{2(10)} \\ W_{2(20)} \end{array}\right]^{(\beta,\gamma)} = \left[\begin{array}{cc} \frac{1}{h_\beta} & -\frac{1}{h_\beta} \\ \frac{2}{h_\beta^2} & \frac{2}{h_\beta^2} \end{array}\right] \left[\begin{array}{c} \bar{u}_2^{2+} \\ \bar{u}_2^{2-} \end{array}\right]^{(\beta,\gamma)} - \frac{4}{h_\beta^2} \left[\begin{array}{c} 0 \\ W_{2(00)} \end{array}\right]^{(\beta,\gamma)} \tag{164}$$

Adding and subtracting Eqs. (153) and (155), we get

$$\left[\begin{array}{c} W_{3(10)} \\ W_{3(20)} \end{array}\right]^{(\beta,\gamma)} = \left[\begin{array}{cc} \frac{1}{h_\beta} & -\frac{1}{h_\beta} \\ \frac{2}{h_\beta^2} & \frac{2}{h_\beta^2} \end{array}\right] \left[\begin{array}{c} \bar{u}_3^{2+} \\ \bar{u}_3^{2-} \end{array}\right]^{(\beta,\gamma)} - \frac{4}{h_\beta^2} \left[\begin{array}{c} 0 \\ W_{3(00)} \end{array}\right]^{(\beta,\gamma)} \tag{165}$$

Adding and subtracting Eqs. (157) and (159), we get

$$\left[\begin{array}{c} W_{3(01)} \\ W_{3(02)} \end{array}\right]^{(\beta,\gamma)} = \left[\begin{array}{cc} \frac{1}{l_\gamma} & -\frac{1}{l_\gamma} \\ \frac{2}{l_\gamma^2} & \frac{2}{l_\gamma^2} \end{array}\right] \left[\begin{array}{c} \bar{u}_3^{3+} \\ \bar{u}_3^{3-} \end{array}\right]^{(\beta,\gamma)} - \frac{4}{l_\gamma^2} \left[\begin{array}{c} 0 \\ W_{3(00)} \end{array}\right]^{(\beta,\gamma)} \tag{166}$$

Adding and subtracting Eqs. (156) and (158), we get

$$\left[\begin{array}{c} W_{2(01)} \\ W_{2(02)} \end{array}\right]^{(\beta,\gamma)} = \left[\begin{array}{cc} \frac{1}{l_\gamma} & -\frac{1}{l_\gamma} \\ \frac{2}{l_\gamma^2} & \frac{2}{l_\gamma^2} \end{array}\right] \left[\begin{array}{c} \bar{u}_2^{3+} \\ \bar{u}_2^{3-} \end{array}\right]^{(\beta,\gamma)} - \frac{4}{l_\gamma^2} \left[\begin{array}{c} 0 \\ W_{2(00)} \end{array}\right]^{(\beta,\gamma)} \tag{167}$$

Equations (164) − (167) relate the first and second order microvariables to the surface-averaged displacements and the zeroth order microvariables. In order to express the microvariables explicitly in terms of the surface-averaged quantities, we make use of the equilibrium equations.

3.3.1 Equilibrium equations

For the structure to remain in equilibrium, the stress field in the subcell (β, γ) must satisfy the equilibrium equations. As in the original formulation of the higher-order theory, we satisfy the equilibrium equations, Eq. (36) in Section 2, in an average sense, which is demonstrated by the following equations

$$\frac{1}{A_{(\beta\gamma)}} \int_{-h_\beta/2}^{h_\beta/2} \int_{-l_\gamma/2}^{l_\gamma/2} \sigma_{ji,j}^{(\beta\gamma)} d\bar{x}_2^{(\beta)} d\bar{x}_3^{(\gamma)} = 0, \qquad i = 2, 3 \tag{168}$$

Substituting Eqs. (125), (126) and (128) − (130) into Eq. (168) and performing the required integration yields, after simplification, the following equations

$$3(C_{22}W_{2(20)} + C_{44}W_{2(02)})^{(\beta,\gamma)} = (C_{12}\alpha_{11} + C_{22}\alpha_{22} + C_{23}\alpha_{33})^{(\beta,\gamma)}T_{(10)}^{(\beta,\gamma)} \tag{169}$$

$$3(C_{33}W_{3(02)} + C_{44}W_{3(20)})^{(\beta,\gamma)} = (C_{13}\alpha_{11} + C_{23}\alpha_{22} + C_{33}\alpha_{33})^{(\beta,\gamma)}T_{(01)}^{(\beta,\gamma)} \tag{170}$$

Substituting the second order displacement microvariables from Eqs. (164) − (167), we obtain the zeroth order microvariables in terms of the surface-averaged displacements and the first order temperature microvariables as shown below

$$W_{2(00)}^{(\beta,\gamma)} = \frac{C_{22}^{(\beta,\gamma)}}{2\bar{C}_{22}^{(\beta,\gamma)}}(\bar{u}_2^{2+} + \bar{u}_2^{2-})^{(\beta,\gamma)} + \frac{h_\beta^2 C_{44}^{(\beta,\gamma)}}{2l_\gamma^2\bar{C}_{22}^{(\beta,\gamma)}}(\bar{u}_2^{3+} + \bar{u}_2^{3-})^{(\beta,\gamma)} - \bar{\alpha}_{22}^{(\beta,\gamma)}T_{(10)}^{(\beta,\gamma)} \tag{171}$$

$$W_{3(00)}^{(\beta,\gamma)} = \frac{C_{33}^{(\beta,\gamma)}}{2\bar{C}_{33}^{(\beta,\gamma)}}(\bar{u}_3^{3+} + \bar{u}_3^{3-})^{(\beta,\gamma)} + \frac{l_\gamma^2 C_{44}^{(\beta,\gamma)}}{2h_\beta^2\bar{C}_{33}^{(\beta,\gamma)}}(\bar{u}_3^{2+} + \bar{u}_3^{2-})^{(\beta,\gamma)} - \bar{\alpha}_{33}^{(\beta,\gamma)}T_{(01)}^{(\beta,\gamma)} \tag{172}$$

where

$$\bar{C}_{22}^{(\beta,\gamma)} = C_{22}^{(\beta,\gamma)} + \frac{h_\beta^2}{l_\gamma^2}C_{44}^{(\beta,\gamma)} \tag{173}$$

$$\bar{C}_{33}^{(\beta,\gamma)} = C_{33}^{(\beta,\gamma)} + \frac{l_\gamma^2}{h_\beta^2}C_{44}^{(\beta,\gamma)} \tag{174}$$

and

$$\bar{\alpha}_{22} = \frac{(C_{12}\alpha_{11} + C_{22}\alpha_{22} + C_{23}\alpha_{33})^{(\beta,\gamma)}}{3\bar{C}_{22}^{(\beta,\gamma)}} \tag{175}$$

$$\bar{\alpha}_{33} = \frac{(C_{13}\alpha_{11} + C_{23}\alpha_{22} + C_{33}\alpha_{33})^{(\beta,\gamma)}}{3\bar{C}_{33}^{(\beta,\gamma)}} \tag{176}$$

Substituting Eqs. (171) − (172) into Eqs. (164) − (167) and simplifying yields

$$\begin{bmatrix} W_{2(10)} \\ W_{2(20)} \end{bmatrix}^{(\beta,\gamma)} = \begin{bmatrix} \frac{1}{h_\beta} & -\frac{1}{h_\beta} \\ \frac{2C_{44}^{(\beta,\gamma)}}{l_\gamma^2\bar{C}_{22}^{(\beta,\gamma)}} & \frac{2C_{44}^{(\beta,\gamma)}}{l_\gamma^2\bar{C}_{22}^{(\beta,\gamma)}} \end{bmatrix} \begin{bmatrix} \bar{u}_2^{2+} \\ \bar{u}_2^{2-} \end{bmatrix}^{(\beta,\gamma)} - \frac{2C_{44}^{(\beta,\gamma)}}{l_\gamma^2\bar{C}_{22}^{(\beta,\gamma)}} \begin{bmatrix} 0 & 0 \\ 1 & 1 \end{bmatrix} \begin{bmatrix} \bar{u}_2^{3+} \\ \bar{u}_2^{3-} \end{bmatrix}^{(\beta,\gamma)} + \bar{\alpha}_{22} \begin{bmatrix} 0 \\ T_{(10)} \end{bmatrix}^{(\beta,\gamma)} \tag{177}$$

$$\begin{bmatrix} W_{3(10)} \\ W_{3(20)} \end{bmatrix}^{(\beta,\gamma)} = \begin{bmatrix} \frac{1}{h_\beta} & -\frac{1}{h_\beta} \\ \frac{2C_{33}^{(\beta,\gamma)}}{h_\beta^2\bar{C}_{33}^{(\beta,\gamma)}} & \frac{2C_{33}^{(\beta,\gamma)}}{h_\beta^2\bar{C}_{33}^{(\beta,\gamma)}} \end{bmatrix} \begin{bmatrix} \bar{u}_3^{2+} \\ \bar{u}_3^{2-} \end{bmatrix}^{(\beta,\gamma)} - \frac{2C_{33}^{(\beta,\gamma)}}{h_\beta^2\bar{C}_{33}^{(\beta,\gamma)}} \begin{bmatrix} 0 & 0 \\ 1 & 1 \end{bmatrix} \begin{bmatrix} \bar{u}_3^{3+} \\ \bar{u}_3^{3-} \end{bmatrix}^{(\beta,\gamma)} + \frac{\bar{\alpha}_{22}l_\gamma^2}{h_\beta^2} \begin{bmatrix} 0 \\ T_{(01)} \end{bmatrix}^{(\beta,\gamma)} \tag{178}$$

$$\left[\begin{array}{c} W_{3(01)} \\ W_{3(02)} \end{array}\right]^{(\beta,\gamma)} = \left[\begin{array}{cc} \frac{1}{l_\gamma} & -\frac{1}{l_\gamma} \\ \frac{2C_{44}^{(\beta,\gamma)}}{h_\beta^2 \bar{C}_{33}^{(\beta,\gamma)}} & \frac{2C_{44}^{(\beta,\gamma)}}{h_\beta^2 \bar{C}_{33}^{(\beta,\gamma)}} \end{array}\right] \left[\begin{array}{c} \bar{u}_3^{3+} \\ \bar{u}_3^{3-} \end{array}\right]^{(\beta,\gamma)} - \frac{2C_{44}^{(\beta,\gamma)}}{h_\beta^2 \bar{C}_{33}^{(\beta,\gamma)}} \left[\begin{array}{cc} 0 & 0 \\ 1 & 1 \end{array}\right] \left[\begin{array}{c} \bar{u}_3^{2+} \\ \bar{u}_3^{2-} \end{array}\right]^{(\beta,\gamma)} + \bar{\alpha}_{33} \left[\begin{array}{c} 0 \\ T_{(01)} \end{array}\right]^{(\beta,\gamma)} \tag{179}$$

$$\left[\begin{array}{c} W_{2(01)} \\ W_{2(02)} \end{array}\right]^{(\beta,\gamma)} = \left[\begin{array}{cc} \frac{1}{l_\gamma} & -\frac{1}{l_\gamma} \\ \frac{2C_{22}^{(\beta,\gamma)}}{l_\gamma^2 \bar{C}_{22}^{(\beta,\gamma)}} & \frac{2C_{22}^{(\beta,\gamma)}}{l_\gamma^2 \bar{C}_{22}^{(\beta,\gamma)}} \end{array}\right] \left[\begin{array}{c} \bar{u}_2^{3+} \\ \bar{u}_2^{3-} \end{array}\right]^{(\beta,\gamma)} - \frac{2C_{22}^{(\beta,\gamma)}}{l_\gamma^2 \bar{C}_{22}^{(\beta,\gamma)}} \left[\begin{array}{cc} 0 & 0 \\ 1 & 1 \end{array}\right] \left[\begin{array}{c} \bar{u}_2^{2+} \\ \bar{u}_2^{2-} \end{array}\right]^{(\beta,\gamma)} + \frac{\bar{\alpha}_{33} h_\beta^2}{l_\gamma^2} \left[\begin{array}{c} 0 \\ T_{(10)} \end{array}\right]^{(\beta,\gamma)} \tag{180}$$

Equations (177) − (180) relate the microvariables to the surface-averaged displacements and the first order temperature microvariables. Now we can obtain the local stiffness matrix for the subcell (β, γ) by substituting the above equations into Eqs. (140) − (143) . Note that the terms involving the first order temperature microvariables can also be expressed in terms of the surface-averaged temperatures by making use of Eqs. (98) and (99). After simplification, we obtain

$$\left[\begin{array}{c} \vec{t}_2^{2+} \\ \vec{t}_2^{2-} \\ \vec{t}_3^{2+} \\ \vec{t}_3^{2-} \\ \vec{t}_2^{3+} \\ \vec{t}_2^{3-} \\ \vec{t}_3^{3+} \\ \vec{t}_3^{3-} \end{array}\right]^{(\beta,\gamma)} = \left[\begin{array}{cccccccc} K_{11} & K_{12} & 0 & 0 & K_{15} & K_{16} & K_{17} & K_{18} \\ K_{21} & K_{22} & 0 & 0 & K_{25} & K_{26} & K_{27} & K_{28} \\ 0 & 0 & K_{33} & K_{34} & K_{35} & K_{36} & K_{37} & K_{38} \\ 0 & 0 & K_{43} & K_{44} & K_{45} & K_{46} & K_{47} & K_{48} \\ K_{51} & K_{52} & K_{53} & K_{54} & K_{55} & K_{56} & 0 & 0 \\ K_{61} & K_{62} & K_{63} & K_{64} & K_{65} & K_{66} & 0 & 0 \\ K_{71} & K_{72} & K_{73} & K_{74} & 0 & 0 & K_{77} & K_{78} \\ K_{81} & K_{82} & K_{83} & K_{84} & 0 & 0 & K_{87} & K_{88} \end{array}\right]^{(\beta,\gamma)} \left[\begin{array}{c} \bar{u}_2^{2+} \\ \bar{u}_2^{2-} \\ \bar{u}_3^{2+} \\ \bar{u}_3^{2-} \\ \bar{u}_2^{3+} \\ \bar{u}_2^{3-} \\ \bar{u}_3^{3+} \\ \bar{u}_3^{3-} \end{array}\right] + \left[\begin{array}{cccc} \Gamma_{11} & \Gamma_{12} & 0 & 0 \\ \Gamma_{21} & \Gamma_{22} & 0 & 0 \\ 0 & 0 & \Gamma_{33} & \Gamma_{34} \\ 0 & 0 & \Gamma_{43} & \Gamma_{44} \\ \Gamma_{51} & \Gamma_{52} & 0 & 0 \\ \Gamma_{61} & \Gamma_{62} & 0 & 0 \\ 0 & 0 & \Gamma_{73} & \Gamma_{74} \\ 0 & 0 & \Gamma_{83} & \Gamma_{84} \end{array}\right]^{(\beta,\gamma)} \left[\begin{array}{c} \bar{T}_2^{+} \\ \bar{T}_2^{-} \\ \bar{T}_3^{+} \\ \bar{T}_3^{-} \end{array}\right]^{(\beta,\gamma)} \tag{181}$$

where

$$\begin{aligned} K_{11}^{(\beta,\gamma)} &= K_{22}^{(\beta,\gamma)} = \frac{C_{22}^{(\beta,\gamma)}}{h_\beta}(4 - 3\frac{C_{22}^{(\beta,\gamma)}}{\bar{C}_{22}^{(\beta,\gamma)}}) \\ K_{12}^{(\beta,\gamma)} &= K_{21}^{(\beta,\gamma)} = \frac{C_{22}^{(\beta,\gamma)}}{h_\beta}(2 - 3\frac{C_{22}^{(\beta,\gamma)}}{\bar{C}_{22}^{(\beta,\gamma)}}) \\ K_{15}^{(\beta,\gamma)} &= K_{16}^{(\beta,\gamma)} = K_{25}^{(\beta,\gamma)} = K_{26}^{(\beta,\gamma)} = -\frac{3C_{22}^{(\beta,\gamma)} C_{44}^{(\beta,\gamma)} h_\beta}{\bar{C}_{22}^{(\beta,\gamma)} l_\gamma^2} \\ K_{17}^{(\beta,\gamma)} &= -K_{18}^{(\beta,\gamma)} = -K_{27}^{(\beta,\gamma)} = K_{28}^{(\beta,\gamma)} = \frac{C_{23}^{(\beta,\gamma)}}{l_\gamma} \end{aligned}$$

$$
\begin{aligned}
K_{33}^{(\beta,\gamma)} &= K_{44}^{(\beta,\gamma)} = \frac{C_{44}^{(\beta,\gamma)}}{h_\beta}(4 - 3\frac{C_{44}^{(\beta,\gamma)}}{\bar{C}_{23}^{(\beta,\gamma)}}) \\
K_{34}^{(\beta,\gamma)} &= K_{43}^{(\beta,\gamma)} = \frac{C_{44}^{(\beta,\gamma)}}{h_\beta}(2 - 3\frac{C_{44}^{(\beta,\gamma)}}{\bar{C}_{23}^{(\beta,\gamma)}}) \\
K_{35}^{(\beta,\gamma)} &= -K_{36}^{(\beta,\gamma)} = -K_{45}^{(\beta,\gamma)} = K_{46}^{(\beta,\gamma)} = \frac{C_{44}^{(\beta,\gamma)}}{l_\gamma} \\
K_{37}^{(\beta,\gamma)} &= K_{38}^{(\beta,\gamma)} = K_{47}^{(\beta,\gamma)} = K_{48}^{(\beta,\gamma)} = -\frac{3C_{33}C_{44}^{(\beta,\gamma)}h_\beta}{\bar{C}_{23}^{(\beta,\gamma)}l_\gamma^2} \\
K_{51}^{(\beta,\gamma)} &= K_{52}^{(\beta,\gamma)} = K_{61}^{(\beta,\gamma)} = K_{62}^{(\beta,\gamma)} = -\frac{3C_{22}C_{44}^{(\beta,\gamma)}l_\gamma}{\bar{C}_{32}^{(\beta,\gamma)}h_\beta^2} \\
K_{53}^{(\beta,\gamma)} &= -K_{54}^{(\beta,\gamma)} = -K_{63}^{(\beta,\gamma)} = K_{64}^{(\beta,\gamma)} = \frac{C_{44}^{(\beta,\gamma)}}{h_\beta} \\
K_{55}^{(\beta,\gamma)} &= K_{66}^{(\beta,\gamma)} = \frac{C_{44}^{(\beta,\gamma)}}{l_\gamma}(4 - 3\frac{C_{44}^{(\beta,\gamma)}}{\bar{C}_{32}^{(\beta,\gamma)}}) \\
K_{56}^{(\beta,\gamma)} &= K_{65}^{(\beta,\gamma)} = \frac{C_{44}^{(\beta,\gamma)}}{l_\gamma}(2 - 3\frac{C_{44}^{(\beta,\gamma)}}{\bar{C}_{32}^{(\beta,\gamma)}}) \\
K_{71}^{(\beta,\gamma)} &= -K_{72}^{(\beta,\gamma)} = -K_{81}^{(\beta,\gamma)} = K_{82}^{(\beta,\gamma)} = \frac{C_{23}^{(\beta,\gamma)}}{h_\beta} \\
K_{73}^{(\beta,\gamma)} &= K_{74}^{(\beta,\gamma)} = K_{83}^{(\beta,\gamma)} = K_{84}^{(\beta,\gamma)} = -\frac{3C_{33}C_{44}^{(\beta,\gamma)}l_\gamma}{\bar{C}_{33}^{(\beta,\gamma)}h_\beta^2} \\
K_{77}^{(\beta,\gamma)} &= K_{88}^{(\beta,\gamma)} = \frac{C_{33}^{(\beta,\gamma)}}{l_\gamma}(4 - 3\frac{C_{33}^{(\beta,\gamma)}}{\bar{C}_{33}^{(\beta,\gamma)}}) \\
K_{78}^{(\beta,\gamma)} &= K_{87}^{(\beta,\gamma)} = \frac{C_{33}^{(\beta,\gamma)}}{l_\gamma}(2 - 3\frac{C_{33}^{(\beta,\gamma)}}{\bar{C}_{33}^{(\beta,\gamma)}})
\end{aligned}
$$

and

$$
\begin{aligned}
\Gamma_{11}^{(\beta,\gamma)} &= -\Gamma_{22}^{(\beta,\gamma)} = 3\bar{\alpha}_{22}^{(\beta,\gamma)}(\frac{C_{22}^{(\beta,\gamma)}}{2} - \bar{C}_{22}^{(\beta,\gamma)}) \\
\Gamma_{21}^{(\beta,\gamma)} &= -\Gamma_{12}^{(\beta,\gamma)} = \frac{3\bar{\alpha}_{22}^{(\beta,\gamma)}C_{22}^{(\beta,\gamma)}}{2} \\
\Gamma_{33}^{(\beta,\gamma)} &= -\Gamma_{34}^{(\beta,\gamma)} = \Gamma_{43}^{(\beta,\gamma)} = -\Gamma_{44}^{(\beta,\gamma)} = \frac{3\bar{\alpha}_{23}^{(\beta,\gamma)}C_{44}^{(\beta,\gamma)}h_\beta}{2l_\gamma} \\
\Gamma_{51}^{(\beta,\gamma)} &= -\Gamma_{52}^{(\beta,\gamma)} = \Gamma_{61}^{(\beta,\gamma)} = -\Gamma_{62}^{(\beta,\gamma)} = \frac{3\bar{\alpha}_{32}^{(\beta,\gamma)}C_{44}^{(\beta,\gamma)}l_\gamma}{2h_\beta} \\
\Gamma_{73}^{(\beta,\gamma)} &= -\Gamma_{84}^{(\beta,\gamma)} = 3\bar{\alpha}_{33}^{(\beta,\gamma)}(\frac{C_{33}^{(\beta,\gamma)}}{2} - \bar{C}_{33}^{(\beta,\gamma)}) \\
\Gamma_{83}^{(\beta,\gamma)} &= -\Gamma_{74}^{(\beta,\gamma)} = \frac{3\bar{\alpha}_{33}^{(\beta,\gamma)}C_{33}^{(\beta,\gamma)}}{2}
\end{aligned}
$$

3.3.2 Displacement continuity conditions

The displacement continuity at the interfaces between adjacent subcells is applied in an average sense. Considering the β^{th} interface, Fig. 6, the surface-averaged displacements in the x_2 direction, $\bar{u}_2^{2+(\beta,\gamma)}$ and $\bar{u}_2^{2-(\beta+1,\gamma)}$, must be equal. Hence, we represent them using just one variable, i.e.,

$$\bar{u}_2^{2+(\beta,\gamma)} = \bar{u}_2^{2-(\beta+1,\gamma)} = \bar{u}_2^{2(\beta+1,\gamma)} \tag{182}$$

Similarly, applying the continuity of surface-averaged displacements in the x_3 direction at the β^{th} interface

$$\bar{u}_3^{2+(\beta,\gamma)} = \bar{u}_3^{-2(\beta+1,\gamma)} = \bar{u}_3^{2(\beta+1,\gamma)} \tag{183}$$

Considering the γ^{th} interface, the surface-averaged displacements in the x_3 direction, $\bar{u}_3^{3+(\beta,\gamma)}$ and $\bar{u}_3^{3-(\beta+1,\gamma)}$, must be equal and therefore can be represented using just one variable, i.e.,

$$\bar{u}_3^{3+(\beta,\gamma)} = \bar{u}_3^{3-(\beta,\gamma+1)} = \bar{u}_3^{3(\beta,\gamma+1)} \tag{184}$$

Similarly, applying the continuity of surface-averaged displacements in the x_2 direction at the γ^{th} interface

$$\bar{u}_2^{3+(\beta,\gamma)} = \bar{u}_2^{3-(\beta,\gamma+1)} = \bar{u}_2^{3(\beta,\gamma+1)} \tag{185}$$

Equations (182) − (185) are similar to the displacement continuity conditions, Eqs. (59) − (62), in Section 2. Equations (182) − (183) and (184) − (185) hold true for $\beta = 1, ..., N_\beta - 1$ and $\gamma = 1, ..., N_\gamma - 1$, respectively. This gives rise to $2(N_\beta - 1)N_\gamma + 2(N_\gamma - 1)N_\beta$ unknown surface-averaged displacements defined at the subcell interfaces (both in x_2 and x_3 directions). The quantities

$$\bar{u}_2^{2(1,\gamma)}, \bar{u}_3^{2(1,\gamma)}, \bar{u}_2^{2\left(N_\beta+1,\gamma\right)}, \bar{u}_3^{2\left(N_\beta+1,\gamma\right)}, \bar{u}_2^{3(\beta,1)}, \bar{u}_3^{3(\beta,1)}, \bar{u}_2^{3(\beta,N_\gamma+1)}, \bar{u}_3^{3(\beta,N_\gamma+1)}$$

define the surface-averaged displacements at the external boundaries of the composite. These quantities are either known or unknown depending on whether tractions or displacements are defined at the external boundaries.

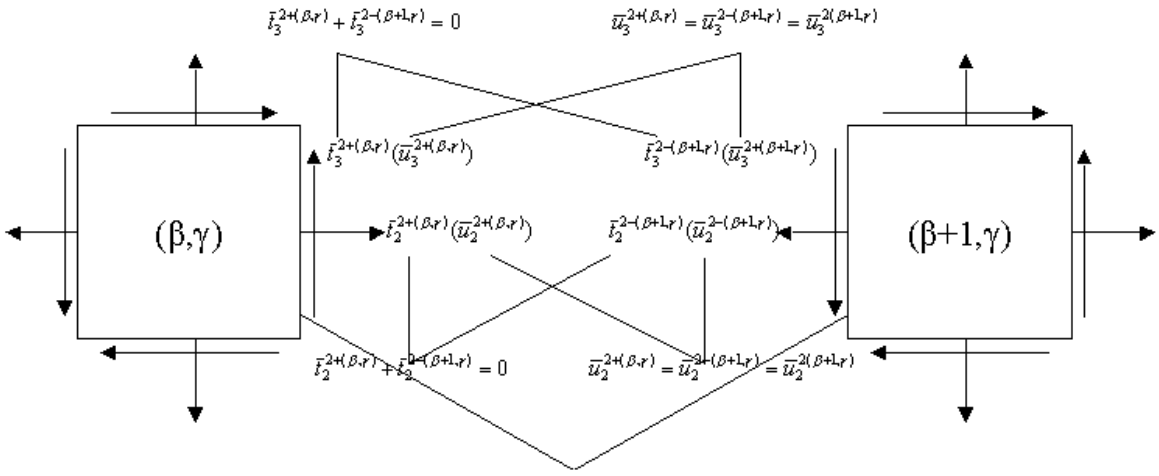

Fig. 6. Traction and displacement continuity applied at the interface of the subcells in an average sense.

3.3.3 Traction continuity conditions

The traction continuity at the interfaces between adjacent subcells is applied in an average sense. Considering the β^{th} interface, Fig. 6, the continuity of tractions in the x_2 direction is ensured by

$$\bar{t}_2^{2+(\beta,\gamma)} + \bar{t}_2^{2-(\beta+1,\gamma)} = 0 \tag{186}$$

where $\bar{t}_2^{+(\beta,\gamma)}$ is the surface-averaged traction at the right face ($\overline{x}_2 = h_\beta/2$) of the subcell (β,γ) and $\bar{t}_2^{-(\beta+1,\gamma)}$ is the surface-averaged traction at the left face ($x_2 = -h_{\beta+1}/2$) of the subcell $(\beta+1,\gamma)$ in the x_2 direction, defined by Eqs. (89) and (88), respectively. Similarly, the continuity of surface-averaged tractions at the β^{th} interface in the x_3 direction is ensured by

$$\bar{t}_3^{2+(\beta,\gamma)} + \bar{t}_3^{2-(\beta+1,\gamma)} = 0 \tag{187}$$

Considering the γ^{th} interface, and applying the continuity of tractions in the x_2 direction in an average sense we obtain

$$\bar{t}_2^{3+(\beta,\gamma)} + \bar{t}_2^{3-(\beta,\gamma+1)} = 0 \tag{188}$$

The continuity of surface-averaged tractions in the x_3 direction at the γ^{th} interface is ensured by

$$\bar{t}_3^{3+(\beta,\gamma)} + \bar{t}_3^{3-(\beta,\gamma+1)} = 0 \tag{189}$$

Equations (186) − (189) are similar to the traction continuity conditions, Eqs. (51) − (54), in Section 2. Using the local stiffness matrix (181), Eqs. (186)-(189) can be expressed in terms of the surface-averaged displacements

$$\begin{aligned}(K_{11}\bar{u}_2^{2+} + K_{12}\bar{u}_2^{2-} + K_{15}\bar{u}_2^{3+} + K_{16}\bar{u}_2^{3-} + K_{17}\bar{u}_3^{3+} + K_{18}\bar{u}_3^{3-})^{(\beta,\gamma)} + \\ (K_{21}\bar{u}_2^{2+} + K_{22}\bar{u}_2^{2-} + K_{25}\bar{u}_2^{3+} + K_{26}\bar{u}_2^{3-} + K_{27}\bar{u}_3^{3+} + K_{28}\bar{u}_3^{3-})^{(\beta+1,\gamma)} \quad = \\ (\Gamma_{11}\bar{T}_2^{+} + \Gamma_{12}\bar{T}_2^{-})^{(\beta,\gamma)} + (\Gamma_{21}\bar{T}_2^{+} + \Gamma_{22}\bar{T}_2^{-})^{(\beta+1,\gamma)}\end{aligned} \tag{190}$$

$$\begin{aligned}(K_{33}\bar{u}_3^{2+} + K_{34}\bar{u}_3^{2-} + K_{35}\bar{u}_2^{3+} + K_{36}\bar{u}_2^{3-} + K_{37}\bar{u}_3^{3+} + K_{38}\bar{u}_3^{3-})^{(\beta,\gamma)} + \\ (K_{43}\bar{u}_3^{2+} + K_{44}\bar{u}_3^{2-} + K_{45}\bar{u}_2^{3+} + K_{46}\bar{u}_2^{3-} + K_{47}\bar{u}_3^{3+} + K_{48}\bar{u}_3^{3-})^{(\beta+1,\gamma)} \quad = \\ (\Gamma_{33}\bar{T}_3^{+} + \Gamma_{34}\bar{T}_3^{-})^{(\beta,\gamma)} + (\Gamma_{43}\bar{T}_3^{+} + \Gamma_{44}\bar{T}_3^{-})^{(\beta+1,\gamma)}\end{aligned} \tag{191}$$

$$\begin{aligned}(K_{51}\bar{u}_2^{2+} + K_{52}\bar{u}_2^{2-} + K_{53}\bar{u}_3^{2+} + K_{54}\bar{u}_3^{2-} + K_{55}\bar{u}_2^{3+} + K_{56}\bar{u}_2^{3-})^{(\beta,\gamma)} + \\ (K_{61}\bar{u}_2^{2+} + K_{62}\bar{u}_2^{2-} + K_{63}\bar{u}_3^{2+} + K_{64}\bar{u}_3^{2-} + K_{65}\bar{u}_2^{3+} + K_{66}\bar{u}_2^{3-})^{(\beta,\gamma+1)} \quad = \\ (\Gamma_{51}\bar{T}_2^{+} + \Gamma_{52}\bar{T}_2^{-})^{(\beta,\gamma)} + (\Gamma_{61}\bar{T}_2^{+} + \Gamma_{62}\bar{T}_2^{-})^{(\beta,\gamma+1)}\end{aligned} \tag{192}$$

$$\begin{aligned}(K_{71}\bar{u}_2^{2+} + K_{72}\bar{u}_2^{2-} + K_{73}\bar{u}_3^{2+} + K_{74}\bar{u}_3^{2-} + K_{77}\bar{u}_3^{3+} + K_{78}\bar{u}_3^{3-})^{(\beta,\gamma)} + \\ (K_{81}\bar{u}_2^{2+} + K_{82}\bar{u}_2^{2-} + K_{83}\bar{u}_3^{2+} + K_{84}\bar{u}_3^{2-} + K_{87}\bar{u}_3^{3+} + K_{88}\bar{u}_3^{3-})^{(\beta,\gamma+1)} \quad = \\ (\Gamma_{73}\bar{T}_3^{+} + \Gamma_{74}\bar{T}_3^{-})^{(\beta,\gamma)} + (\Gamma_{83}\bar{T}_3^{+} + \Gamma_{84}\bar{T}_3^{-})^{(\beta,\gamma+1)}\end{aligned} \tag{193}$$

Using the displacement continuity conditions given by Eqs. (182) − (185), Eqs. (190) − (193) can be written in terms of the common surface-averaged displacements

$$\begin{aligned}K_{12}^{(\beta,\gamma)}\bar{u}_2^{2(\beta,\gamma)} + (K_{11}^{(\beta,\gamma)} + K_{22}^{(\beta+1,\gamma)})\bar{u}_2^{2(\beta+1,\gamma)} + K_{21}^{(\beta+1,\gamma)}\bar{u}_2^{2(\beta+2,\gamma)} + K_{16}^{(\beta,\gamma)}\bar{u}_2^{3(\beta,\gamma)} + \\ K_{15}^{(\beta,\gamma)}\bar{u}_2^{3(\beta,\gamma+1)} + K_{26}^{(\beta+1,\gamma)}\bar{u}_2^{3(\beta+1,\gamma)} + K_{25}^{(\beta+1,\gamma)}\bar{u}_2^{3(\beta+1,\gamma+1)} + K_{18}^{(\beta,\gamma)}\bar{u}_3^{3(\beta,\gamma)} + \\ K_{17}^{(\beta,\gamma)}\bar{u}_3^{3(\beta,\gamma+1)} + K_{28}^{(\beta+1,\gamma)}\bar{u}_3^{3(\beta+1,\gamma)} + K_{27}^{(\beta+1,\gamma)}\bar{u}_3^{3(\beta+1,\gamma+1)} \quad = \\ \Gamma_{12}^{(\beta,\gamma)}\bar{T}_2^{(\beta,\gamma)} + (\Gamma_{11}^{(\beta,\gamma)} + \Gamma_{22}^{(\beta+1,\gamma)})\bar{T}_2^{(\beta+1,\gamma)} + \Gamma_{21}^{(\beta+1,\gamma)}\bar{T}_2^{(\beta+2,\gamma)}\end{aligned} \tag{194}$$

$$K_{34}^{(\beta,\gamma)}\bar{u}_3^{2(\beta,\gamma)} + (K_{33}^{(\beta,\gamma)} + K_{44}^{(\beta+1,\gamma)})\bar{u}_3^{2(\beta+1,\gamma)} + K_{43}^{(\beta+1,\gamma)}\bar{u}_3^{2(\beta+2,\gamma)} + K_{36}^{(\beta,\gamma)}\bar{u}_2^{3(\beta,\gamma)} +$$
$$K_{46}^{(\beta+1,\gamma)}\bar{u}_2^{3(\beta+1,\gamma)} + K_{35}^{(\beta,\gamma)}\bar{u}_2^{3(\beta,\gamma+1)} + K_{45}^{(\beta+1,\gamma)}\bar{u}_2^{3(\beta+1,\gamma+1)} + K_{38}^{(\beta,\gamma)}\bar{u}_3^{3(\beta,\gamma)} +$$
$$K_{48}^{(\beta+1,\gamma)}\bar{u}_3^{3(\beta+1,\gamma)} + K_{37}^{(\beta,\gamma)}\bar{u}_3^{3(\beta,\gamma+1)} + K_{47}^{(\beta+1,\gamma)}\bar{u}_3^{3(\beta+1,\gamma+1)} =$$
$$\Gamma_{34}^{(\beta,\gamma)}\bar{T}_3^{(\beta,\gamma)} + \Gamma_{33}^{(\beta,\gamma)}\bar{T}_3^{(\beta,\gamma+1)} + \Gamma_{44}^{(\beta+1,\gamma)}\bar{T}_3^{(\beta+1,\gamma)} + \Gamma_{43}^{(\beta+1,\gamma)}\bar{T}_3^{(\beta+1,\gamma+1)} \tag{195}$$

$$K_{52}^{(\beta,\gamma)}\bar{u}_2^{2(\beta,\gamma)} + K_{51}^{(\beta,\gamma)}\bar{u}_2^{2(\beta+1,\gamma)} + K_{62}^{(\beta,\gamma+1)}\bar{u}_2^{2(\beta,\gamma+1)} + K_{61}^{(\beta,\gamma+1)}\bar{u}_2^{2(\beta+1,\gamma+1)} +$$
$$K_{54}^{(\beta,\gamma)}\bar{u}_3^{2(\beta,\gamma)} + K_{53}^{(\beta,\gamma)}\bar{u}_3^{2(\beta+1,\gamma)} + K_{64}^{(\beta,\gamma+1)}\bar{u}_3^{2(\beta,\gamma+1)} + K_{63}^{(\beta,\gamma+1)}\bar{u}_3^{2(\beta+1,\gamma+1)} +$$
$$K_{56}^{(\beta,\gamma)}\bar{u}_2^{3(\beta,\gamma)} + (K_{55}^{(\beta,\gamma)} + K_{66}^{(\beta,\gamma+1)})\bar{u}_2^{3(\beta,\gamma+1)} + K_{65}^{(\beta,\gamma+1)}\bar{u}_2^{3(\beta,\gamma+2)} =$$
$$\Gamma_{52}^{(\beta,\gamma)}\bar{T}_2^{(\beta,\gamma)} + \Gamma_{51}^{(\beta,\gamma)}\bar{T}_2^{(\beta+1,\gamma)} + \Gamma_{62}^{(\beta,\gamma+1)}\bar{T}_2^{(\beta,\gamma+1)} + \Gamma_{61}^{(\beta,\gamma+1)}\bar{T}_2^{(\beta+1,\gamma+1)} \tag{196}$$

$$K_{72}^{(\beta,\gamma)}\bar{u}_2^{2(\beta,\gamma)} + K_{71}^{(\beta,\gamma)}\bar{u}_2^{2(\beta+1,\gamma)} + K_{82}^{(\beta,\gamma+1)}\bar{u}_2^{2(\beta,\gamma+1)} + K_{81}^{(\beta,\gamma+1)}\bar{u}_2^{2(\beta+1,\gamma+1)} +$$
$$K_{74}^{(\beta,\gamma)}\bar{u}_3^{2(\beta,\gamma)} + K_{73}^{(\beta,\gamma)}\bar{u}_3^{2(\beta+1,\gamma)} + K_{84}^{(\beta,\gamma+1)}\bar{u}_3^{2(\beta,\gamma+1)} + K_{83}^{(\beta,\gamma+1)}\bar{u}_3^{2(\beta+1,\gamma+1)} +$$
$$K_{78}^{(\beta,\gamma)}\bar{u}_3^{3(\beta,\gamma)} + (K_{77}^{(\beta,\gamma)} + K_{88}^{(\beta,\gamma+1)})\bar{u}_3^{3(\beta,\gamma+1)} + K_{87}^{(\beta,\gamma+1)}\bar{u}_3^{3(\beta,\gamma+2)} =$$
$$\Gamma_{74}^{(\beta,\gamma)}\bar{T}_3^{(\beta,\gamma)} + (\Gamma_{73}^{(\beta,\gamma)} + \Gamma_{84}^{(\beta,\gamma+1)})\bar{T}_3^{(\beta,\gamma+1)} + \Gamma_{83}^{(\beta,\gamma+1)}\bar{T}_3^{(\beta,\gamma+2)} \tag{197}$$

Thus, Eqs. $(194) - (197)$ provide us with a total of $2(N_\beta - 1)N_\gamma + 2(N_\gamma - 1)N_\beta$ equations in terms of the common interfacial surface-averaged displacements and the surface-averaged displacements at the external boundaries.

3.3.4 Boundary conditions

At the external boundaries of the composite, we have $2(N_\beta + N_\gamma)$ faces of the subcells where either tractions or displacements are defined. This gives rise to additional $4(N_\beta + N_\gamma)$ unknown surface-averaged quantities. The additional $4(N_\beta + N_\gamma)$ equations are obtained from the imposed boundary conditions given by

$$\bar{t}_i^{2(1,\gamma)} = t_{left}^{(\gamma)}(x_3) \tag{198}$$

$$\bar{t}_i^{2(N_\beta,\gamma)} = t_{right}^{(\gamma)}(x_3) \qquad i = 2,3 \tag{199}$$

where $t_{left}^{(\gamma)}(x_3)$ and $t_{right}^{(\gamma)}(x_3)$ are piece-wise uniform surface tractions applied on the vertical boundaries in the $x_2 - x_3$ plane. Similar reasoning holds for subcells $(\beta, 1)$, and (β, N_γ). Alternatively, if the displacements are specified on the vertical boundaries, then the applied boundary conditions are given by

$$\overline{u}_i^{3(\beta,1)} = u_{bottom}^{(\beta)}(x_2) \tag{200}$$

$$\overline{u}_i^{3(\beta,N_\gamma)} = u_{top}^{(\beta)}(x_2) \qquad i = 2,3 \tag{201}$$

For other type of boundary conditions, the Eqs. $(198) - (201)$ are modified accordingly.

Note that at least one $\bar{u}_2^{(\cdot)}$ and at least one $\bar{u}_3^{(\cdot)}$ should be defined at the external boundary in order to prevent rigid body motion.

3.3.5 Solution for the surface-averaged displacements

Equations (194) − (197) together with the imposed boundary conditions (198) − (201) provide us with the necessary $2(N_\beta+1)N_\gamma+2(N_\gamma+1)N_\beta$ relations for the $2(N_\beta+1)N_\gamma+2(N_\gamma+1)N_\beta$ unknown surface-averaged variables, i.e., $2(N_\beta-1)N_\gamma+2(N_\gamma-1)N_\beta$ unknown common interfacial surface-averaged displacements along with $4(N_\beta+N_\gamma)$ unknown surface-averaged displacements and/or surface tractions at the external boundaries. Also, the unknown uniform strain $\bar{\varepsilon}_{11}$ is determined from the generalized plane strain condition given by Eq. (124). For plane strain, $\bar{\varepsilon}_{11}$ is zero.

The final system of equations obtained is symbolically written as

$$\mathbf{K}\ \overline{\mathbf{U}}=\overline{\mathbf{t}} \tag{202}$$

In the above equation, $\mathbf{K}$ is the global stiffness matrix obtained after assembling the local stiffness matrices given by Eq. (181) using the local-global stiffness matrix approach as explained above. The matrix $\mathbf{K}$ essentially contains information on the geometry and thermomechanical properties of the individual $N_\beta N_\gamma$ subcells. The general format and assembly of the global stiffness matrix $\mathbf{K}$ has been summarized in the next subsection. The vector $\overline{\mathbf{U}}$ contains the unknown surface-averaged displacements at the subcell interfaces and the outer edges of the composite and is given by

$$\overline{\mathbf{U}}=[\bar{\mathbf{u}}_2^{2(1)},...,\bar{\mathbf{u}}_2^{2(N_\gamma)},\bar{\mathbf{u}}_3^{2(1)},...,\bar{\mathbf{u}}_3^{2(N_\gamma)},\bar{\mathbf{u}}_2^{3(1)},...,\bar{\mathbf{u}}_2^{3(N_\beta)},\bar{\mathbf{u}}_3^{3(1)},...,\bar{\mathbf{u}}_3^{3(N_\beta)},\bar{\varepsilon}_{11}]$$

where

$$\begin{aligned}
\bar{\mathbf{u}}_2^{2(\gamma)} &= [\bar{u}_2^{2(1,\gamma)},...,\bar{u}_2^{2(N_\beta+1,\gamma)}] \qquad \bar{\mathbf{u}}_3^{2(\gamma)}=[\bar{u}_3^{2(1,\gamma)},...,\bar{u}_3^{2(N_\beta+1,\gamma)}]\\
\bar{\mathbf{u}}_2^{3(\beta)} &= [\bar{u}_2^{3(1,\beta)},...,\bar{u}_2^{3(N_\beta+1,\beta)}] \qquad \bar{\mathbf{u}}_3^{3(\beta)}=[\bar{u}_3^{3(1,\beta)},...,\bar{u}_3^{3(N_\beta+1,\beta)}]
\end{aligned}$$

The surface-averaged traction vector $\overline{\mathbf{t}}$ contains information on the applied boundary conditions and the mechanical effects produced by thermal loading.

Once Eq. (202) is solved for the surface-averaged displacements at all the subcell interfaces and external boundaries, we substitute the surface-averaged displacements back into Eqs. (171) − (172) and Eqs. (164) − (167) and obtain the microvariables $W_{i(mn)}^{(\beta,\gamma)}$ which define the displacement field in each subcell.

3.3.6 Assembly of the global stiffness matrix K

The general format and assembly of the global stiffness matrix $\mathbf{K}$ is summarized in this subsection. $\mathbf{K}$ consists of eight submatrices

$$\mathbf{K}=\begin{bmatrix}
\mathbf{K}_{11} & \mathbf{0} & \mathbf{K}_{13} & \mathbf{K}_{14}\\
\mathbf{0} & \mathbf{K}_{22} & \mathbf{K}_{23} & \mathbf{K}_{24}\\
\mathbf{K}_{31} & \mathbf{K}_{32} & \mathbf{K}_{33} & \mathbf{0}\\
\mathbf{K}_{41} & \mathbf{K}_{42} & \mathbf{0} & \mathbf{K}_{44}
\end{bmatrix}$$

where $\mathbf{K}_{11},\mathbf{K}_{22},\mathbf{K}_{33}$ and $\mathbf{K}_{44}$ relate the quantities in their respective directions and have entries concentrated along the diagonal. The remaining submatrices represent coupling of the field variables in the x_2 and x_3 directions and have entries scattered throughout. The size of the global stiffness matrix $\mathbf{K}$ is $[2N_\beta(N_\gamma+1)+2N_\gamma(N_\beta+1)]\times[2N_\beta(N_\gamma+1)+2N_\gamma(N_\beta+1)]$ for plane strain. An additional row and column is added for the generalized plane strain case. The structure of the submatrix $\mathbf{K}_{11}$ is shown below

$$\mathbf{K}_{11} = \begin{bmatrix} \mathbf{A}_{11}^{(1)} & \mathbf{0} & \mathbf{0} & \mathbf{0} & \mathbf{0} & \mathbf{0} & \mathbf{0} & \mathbf{0} \\ \mathbf{0} & \mathbf{A}_{11}^{(2)} & \mathbf{0} & \mathbf{0} & \mathbf{0} & \mathbf{0} & \mathbf{0} & \mathbf{0} \\ \mathbf{0} & \mathbf{0} & . & \mathbf{0} & \mathbf{0} & \mathbf{0} & \mathbf{0} & \mathbf{0} \\ \mathbf{0} & \mathbf{0} & \mathbf{0} & . & \mathbf{0} & \mathbf{0} & \mathbf{0} & \mathbf{0} \\ \mathbf{0} & \mathbf{0} & \mathbf{0} & \mathbf{0} & . & \mathbf{0} & \mathbf{0} & \mathbf{0} \\ \mathbf{0} & \mathbf{0} & \mathbf{0} & \mathbf{0} & \mathbf{0} & . & \mathbf{0} & \mathbf{0} \\ \mathbf{0} & \mathbf{0} & \mathbf{0} & \mathbf{0} & \mathbf{0} & \mathbf{0} & . & \mathbf{0} \\ \mathbf{0} & \mathbf{0} & \mathbf{0} & \mathbf{0} & \mathbf{0} & \mathbf{0} & \mathbf{0} & \mathbf{A}_{11}^{(N_\gamma)} \end{bmatrix}$$

where the size of $\mathbf{K}_{11}$ is $[N_\gamma(N_\beta+1) \times N_\gamma(N_\beta+1)]$. The structure of the submatrices $\mathbf{A}_{11}^{(\gamma)}$ is shown in the appendix. The structure of $\mathbf{K}_{22}, \mathbf{K}_{33}$ and $\mathbf{K}_{44}$ is similar to $\mathbf{K}_{11}$. The structure of the coupling matrix $\mathbf{K}_{13}$ is shown below

$$\mathbf{K}_{13} = \begin{bmatrix} \mathbf{B}_{13}^{(11)} & \mathbf{B}_{13}^{(12)} & . & . & . & . & . & \mathbf{B}_{13}^{(1N_\beta)} \\ \mathbf{B}_{13}^{(21)} & \mathbf{B}_{13}^{(22)} & . & . & . & . & . & \mathbf{B}_{13}^{(2N_\beta)} \\ . & . & . & . & . & . & . & . \\ . & . & . & . & . & . & . & . \\ . & . & . & . & . & . & . & . \\ . & . & . & . & . & . & . & . \\ . & . & . & . & . & . & . & . \\ \mathbf{B}_{13}^{(N_\gamma 1)} & \mathbf{B}_{13}^{(N_\gamma 2)} & . & . & . & . & . & \mathbf{B}_{13}^{(N_\gamma N_\beta)} \end{bmatrix}$$

where the size of $\mathbf{K}_{13}$ is $[N_\gamma(N_\beta+1) \times N_\beta(N_\gamma+1)]$. The structure of the submatrices $\mathbf{B}_{13}^{(\gamma\beta)}$ is shown in the appendix. The structure of the remaining coupling matrices is similar to $\mathbf{K}_{13}$.

4 Mesh-Sensitivity and Validation Studies

The two-dimensional formulation of the original higher-order theory was discussed briefly in Section 2. In Section 3, an efficient reformulation of the higher-order theory was developed and discussed in detail. The procedure for determining the various field quantities using the reformulated higher-order theory was also outlined in Section 3. The next step is to verify the efficiency and accuracy of this reformulated version for various thermal, mechanical, and thermomechanical problems. In this section, we investigate the convergence of thermal and mechanical field quantities with mesh refinement and also verify their accuracy upon comparison with analytical and finite-element solutions.

4.1 Mesh Sensitivity: Thermal Problem

In this subsection, the convergence of temperature field with mesh refinement is investigated and the results are compared with an analytical solution. The problem definition, investigated geometry and meshing are shown in Fig. 7. As shown in Fig. 7 (a), the cross-section of the block has unit dimensions in the x_2-x_3 plane. The dimension of the block is considered infinite in the out-of-plane (x_1) direction which, however, does not play a role in the temperature field analysis. The block is subjected to a temperature of $100°C$, which is held constant, at the left, top and bottom faces and a temperature of $200°C$ at the right face. As shown in Figs. 7 (b), (c) and (d), the cross-section of the block in the $x_2 - x_3$ plane is discretized into $4 \times 4, 12 \times 12$, and 32×32 subcells, respectively,

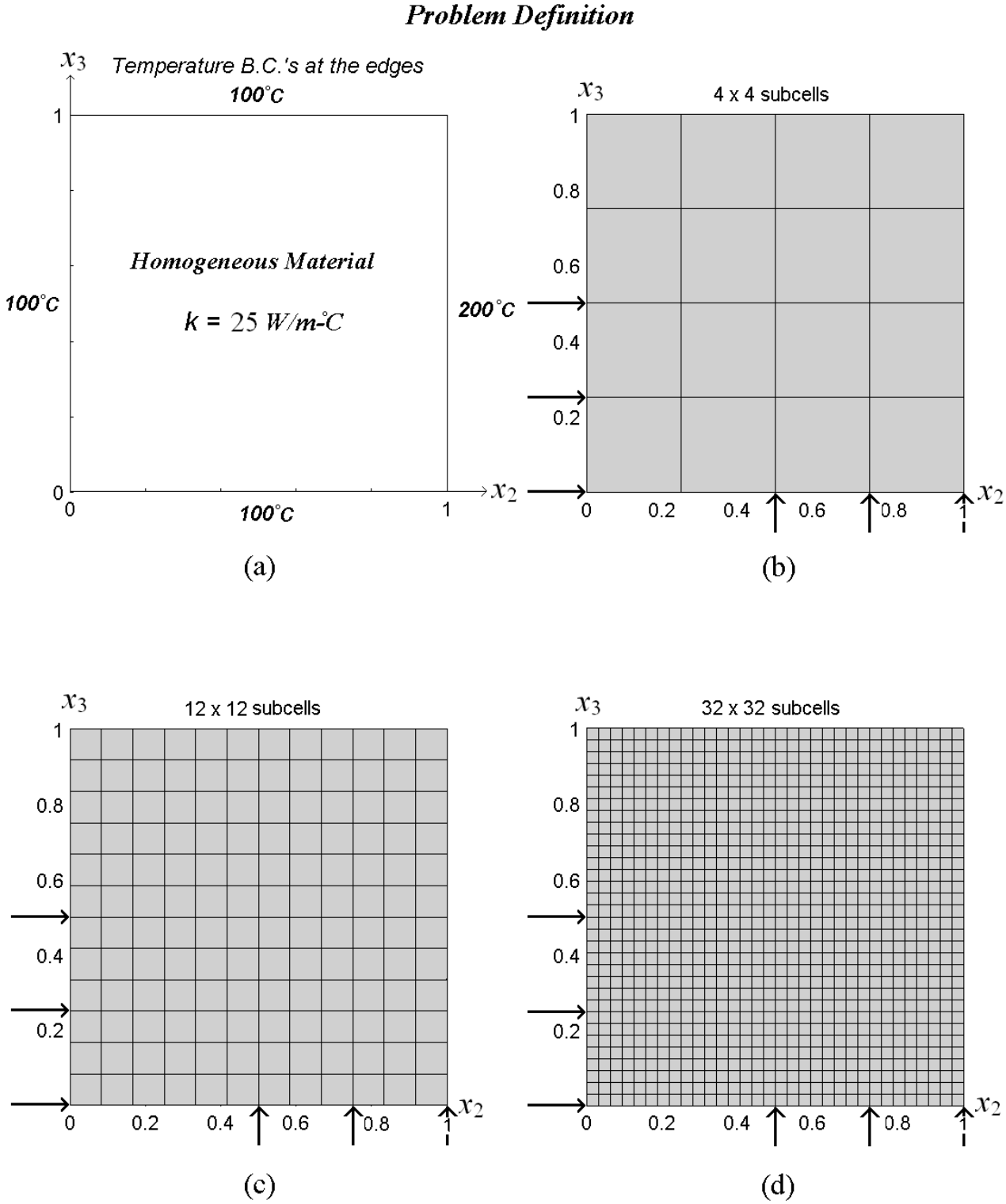

Fig. 7. Problem definition, investigated geometry and discretization used for mesh sensitivity studies: thermal problem.

of uniform size. The material within the block is homogeneous and the thermal conductivity is taken to be 25 $W/m-°C$. However, the analytical solution of the Laplace's equation indicates that the temperature field is independent of the thermal conductivity for the homogeneous case.

For the given boundary conditions, geometry and meshing, the temperature field was generated using the reformulated higher-order theory. Analytical solution for the temperature field was obtained by solving the Laplace equation using the standard Fourier series approach, Zhong (2002). The contour plots of the temperature fields for the $4 \times 4, 12 \times 12$, and 32×32 subcell meshes are shown in Figs. 8 (a), (b) and (c), respectively, and are compared with the analytical solution shown in Fig. 8 (d). As observed from the contour plots, the 4×4 subcell mesh approximates the actual temperature field only in a rough sense. As the mesh is refined to 12×12 subcells, the temperature field becomes almost identical with the actual temperature field except near the $(1, 0)$ and $(1, 1)$ coordinates in the $x_2 - x_3$ plane. These are the points of temperature discontinuity and hence greater mesh refinement is required in order to properly capture the actual temperature near these points. This is achieved with the 32×32 subcell mesh for which the temperature field, Fig. 8 (c), is visually identical to the actual temperature field, Fig. 8 (d), obtained from the analytical solution.

Next, we consider the convergence behavior along several cross-sections. For the 4×4 subcell mesh shown in Fig. 7(b), the cross-section along the line $x_3 = 0.25$ happens to be the interface between the subcells $(1, \gamma)$ and $(2, \gamma)$, and the cross-section along the line $x_3 = 0.5$ is the interface between the subcells $(2, \gamma)$ and $(3, \gamma)$. Similarly, for the 12×12 and 32×32 subcell cases, the cross-sections along the lines $x_3 = 0.25$ and $x_3 = 0.5$ run along the corresponding subcell interfaces. The pointwise temperature distribution (also displacements and stresses) along each interface can be calculated using the microvariables associated with the subcell on either side of the interface. In general, the microvariables belonging to subcells on the opposite sides of the interface are different. Therefore, the pointwise interfacial temperatures calculated using the microvariables on either side will be different since the thermal/heat flux continuity conditions across the interface are applied in a surface-average sense. However, with the refinement in mesh, the interfacial temperatures calculated using the subcell microvariables on either side of the interface should converge. The exception occurs when the interfacial line happens to be the line of symmetry. In that case, the magnitude of the subcell microvariables on the opposite sides of the interface is identical and hence the interfacial temperatures.

Figure 9 shows the temperature distributions along the lines $x_3 = 0.25$ and $x_3 = 0.5$. The symbol $\bar{T}_2$ denotes the common interfacial surface-averaged temperatures which are the basis of the reformulation. The product of the global thermal conductivity with these interfacial surface-averaged temperatures yields the applied thermal/heat flux boundary conditions. T^+ denotes the interfacial temperature obtained using the microvariables of the subcells lying below the interfacial lines. T^- denotes the interfacial temperature obtained using the microvariables of the subcells lying above the interfacial lines. As observed in Fig. 9 (a), the temperature distributions along the line $x_3 = 0.25$ calculated using the subcell microvariables on the opposite sides of the interface are quite different for the 4×4 subcell case. However, the interfacial temperature distributions tend to converge to the same values for the 12×12 subcell case and practically coincide for the 32×32 subcell case, Figs. 9 (c) and (e), respectively. Also, the surface-averaged temperatures ($\bar{T}_2$) tend to converge in a piece-wise uniform manner to the actual temperature distribution with mesh refinement. For the cross-section along the line $x_3 = 0.5$, the temperature distributions, T^+ and T^-, calculated using the subcell microvariables on the opposite sides of the interface are identical even for the 4×4 subcell case, Fig. 9 (b). This is because the line $x_3 = 0.5$ happens to be the line of symmetry for the given boundary conditions and hence the microvariables belonging to the subcells on the opposite side of the interface are identical. This provides an additional verification of the results obtained using the reformulated higher-order theory.

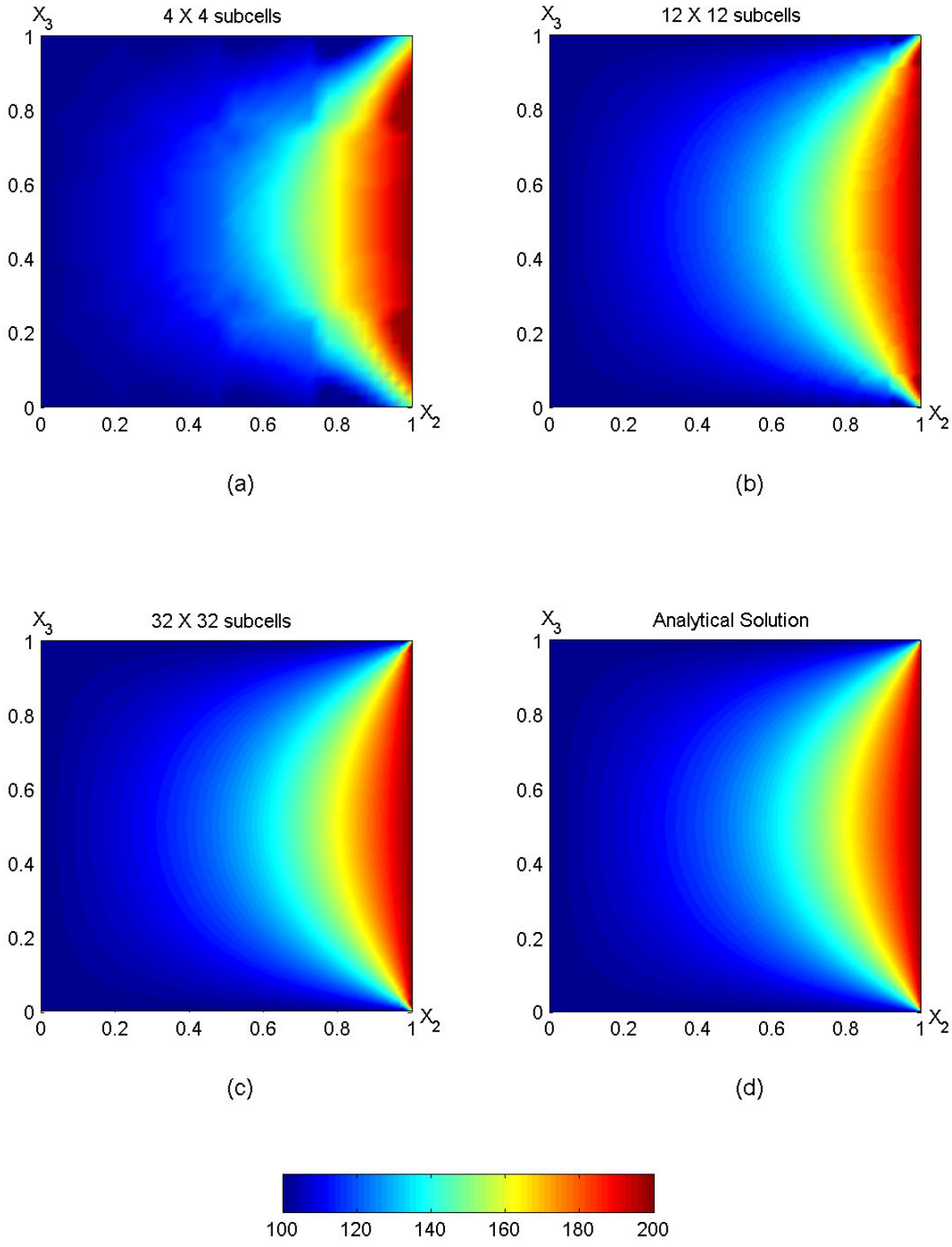

Fig. 8. Temperature field for mesh discretizations and boundary conditions given in Fig. 7 and comparison with analytical solution.

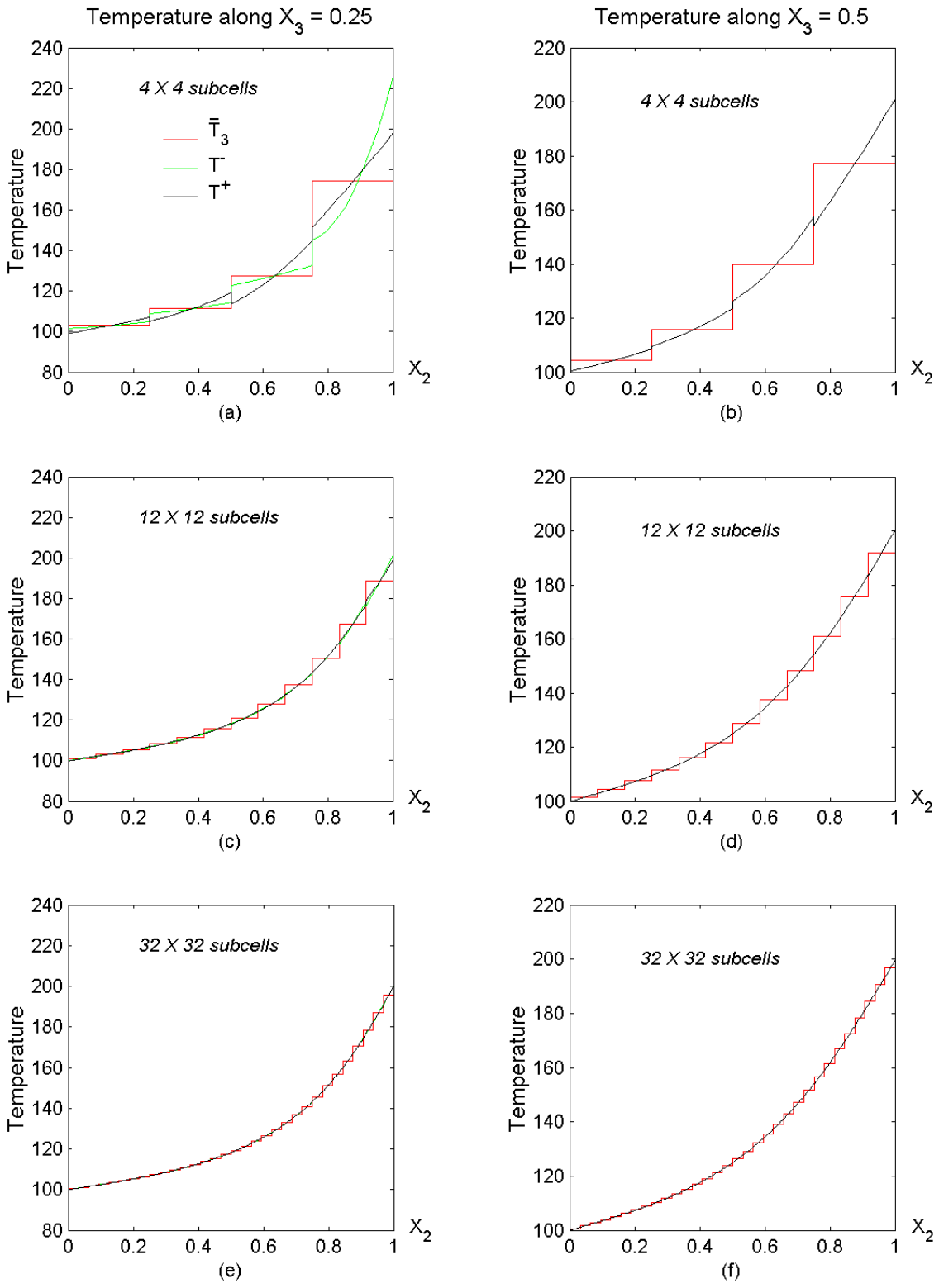

Fig. 9. Convergence studies for temperature distributions along the cross-sections $x_3 = 0.25$, 0.5 shown in Fig. 7.

Figure 10 shows the temperature distributions along the lines $x_2 = 0.5$ and $x_2 = 0.75$. These cross-sections do not lie along the line of symmetry and hence the corresponding interfacial distributions exhibit trends similar to those observed in the cross-section along the line $x_3 = 0.25$ described above. The temperature distributions T^+ and T^- calculated using the subcell microvariables on the left and right sides of the interface, respectively, are quite different for the 4×4 subcell case, Figs. 10 (a) and (b). These interfacial temperature distributions tend to converge to the same values for the 12×12 subcell case, Figs. 10 (c) and (d), and coincide for the 32×32 subcell case, Figs. 10 (e) and (f). Also, the surface-averaged temperatures ($\bar{T}_3$) tend to converge to the actual temperature distribution with mesh refinement.

Figure 11 shows the temperature distributions along the boundaries $x_3 = 0$ and $x_2 = 1$. As observed in the figure, these distributions calculated using the reformulated higher-order theory approach the applied boundary conditions with mesh refinement. However, they do not exactly match the applied boundary conditions due to the presence of the temperature discontinuity at the $(1, 0)$ and $(1, 1)$ coordinates. Virtually, an infinitely dense mesh near these points would be required to exactly match the applied boundary conditions. Even in the case of the analytical solution, a large number of terms in the Fourier series expansion is needed in order to obtain converged solution near the points of temperature discontinuity. At the point of discontinuity, however, only the average value is obtained according to the well-known theorem.

The interfacial temperature distributions calculated using the subcell microvariables on the opposite sides of the interface and averaged at each point across the interface are plotted along the various cross-sections (along the lines $x_3 = 0.25, 0.5$ and $x_2 = 0.5, 0.75$) in Fig. 12. These plots were generated for the different meshes considered above and the results are compared with the analytical solution. As observed in these cross-sectional plots, averaging the temperatures calculated using the subcell microvariables on the opposite sides of the interface produces acceptable results even for the rough mesh as in the 4×4 subcell case considered here. The difference between the analytical solution and the 4×4 subcell mesh is greater in the regions of high temperature gradients. Since the considered cross-sections are removed from the points of temperature discontinuity, the temperature distributions generated using 12×12 and 32×32 subcell meshes coincide with the analytical solution.

4.2 Validation: Thermal Problem

In the case of functionally graded materials, the microstructural gradation is typically varied gradually in a manner that depends on the boundary conditions in order to obtain the required optimized composition profile. This results in continuous or discrete gradation of microstructure as described in Section 1, and therefore continuously or discretely varying properties. In this subsection, a heterogeneous composition with discrete variation of microstructure is considered. In order to generate discretely varying thermal conductivity k, a continuous (exponential) function of spatial coordinates is employed as a basis. The thermal conductivity is then calculated at the center of each subcell according to the given function and is assumed to be constant within the subcell. The results are compared with the finite-element solution obtained using ANSYS, and the effect of thermal conductivity variation on temperature field and its gradients is discussed.

Four different thermal conductivity variations were considered. The problem definition, investigated geometry and meshing are given in Fig. 13. The investigated geometry and meshing are the same for all four cases. The cross-section of the block has unit dimensions in the $x_2 - x_3$ plane and is considered infinitely long in the out-of-plane (x_1) direction. As observed in Subsection 4.1, the temperature field for the homogeneous case converged fairly well with the 12×12 subcell mesh except at the points of temperature discontinuity, and it was identical to the actual solution for the 32×32 subcell mesh. Therefore, in the cases considered here, the cross-section was discretized

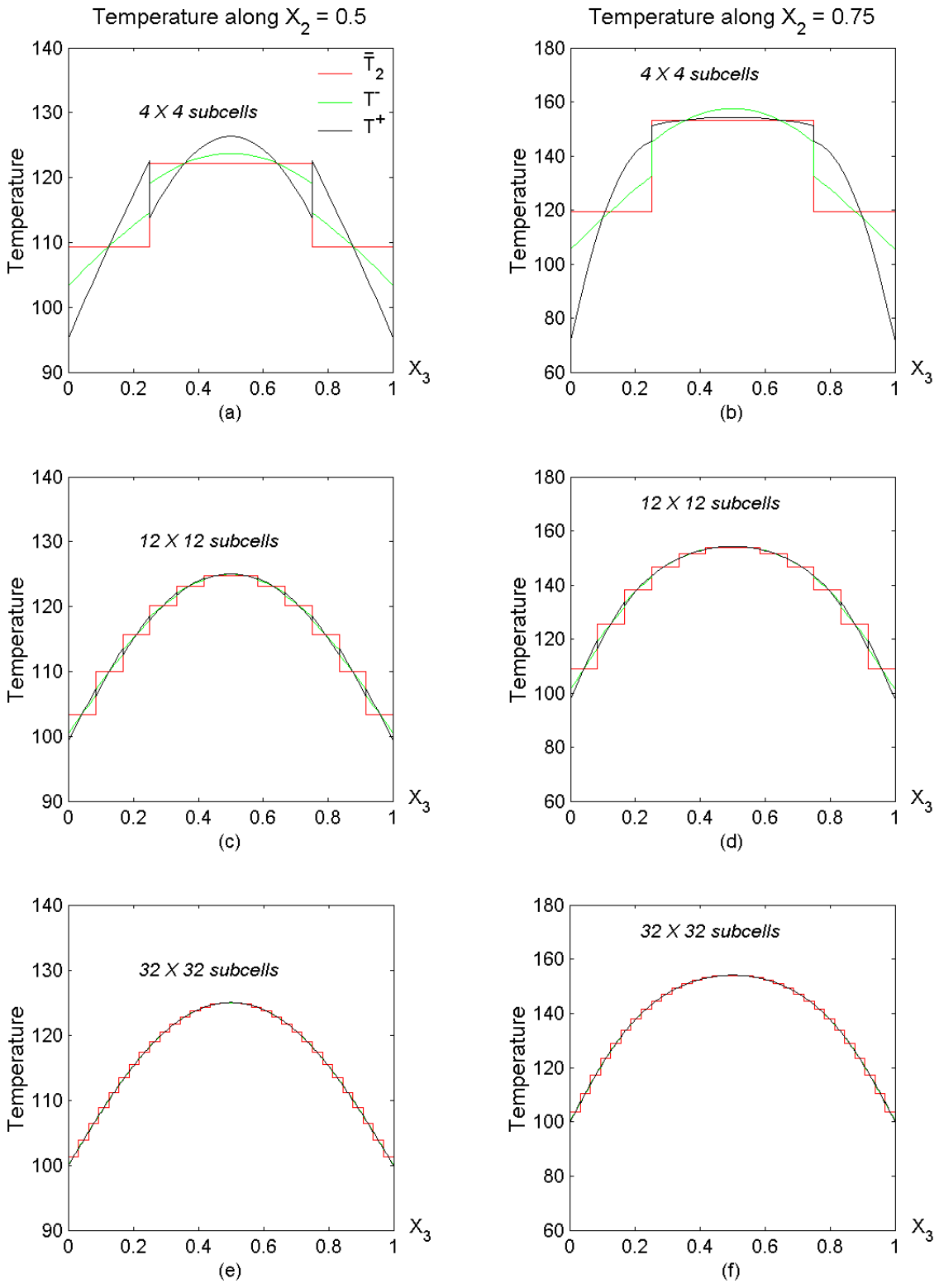

Fig. 10. Convergence studies for temperature distributions along the cross-sections $x_2 = 0.5, 0.75$ shown in Fig. 7.

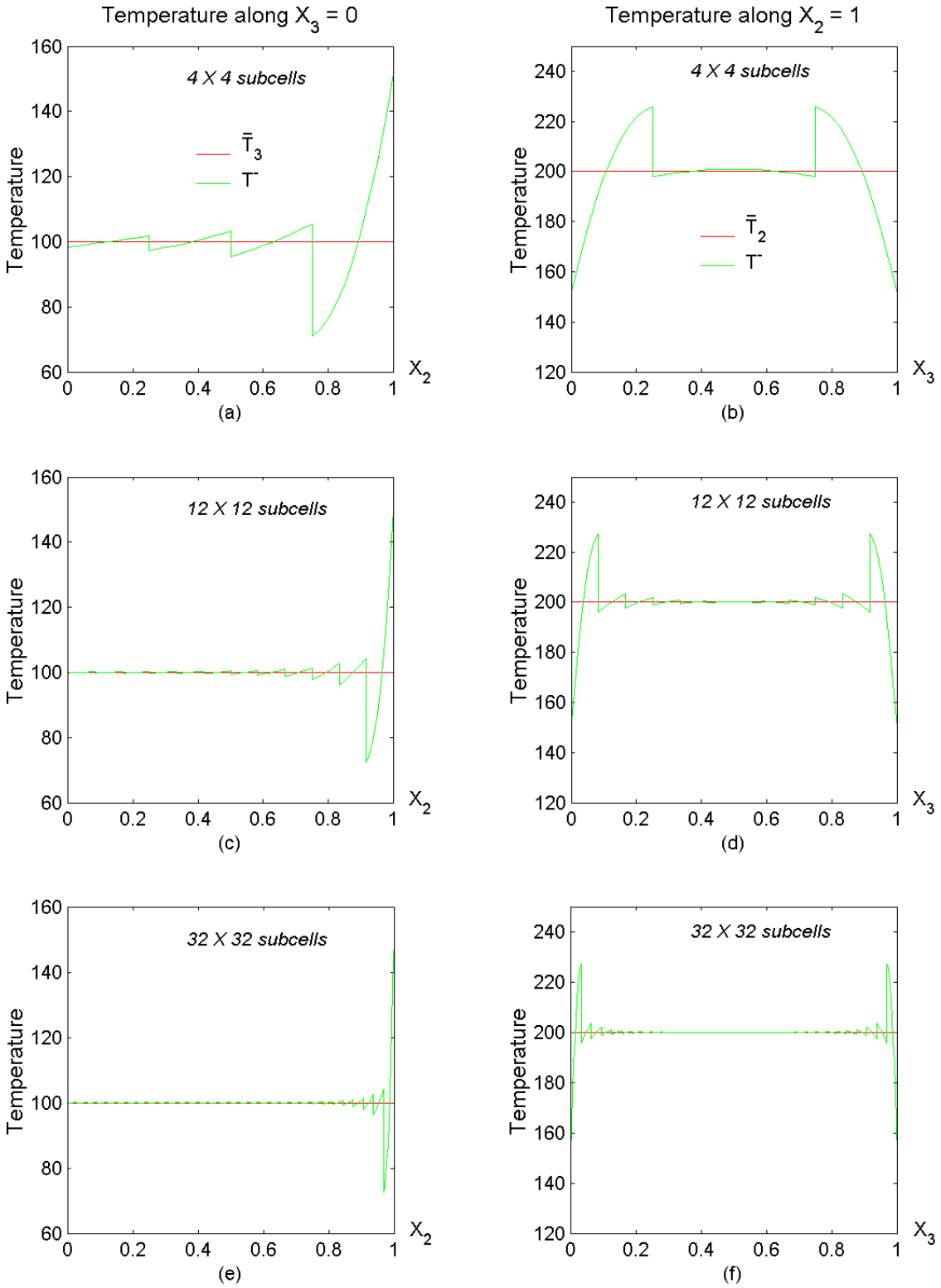

Fig. 11. Convergence studies for temperature distributions along the edges $x_3 = 0$ and $x_2 = 1$ shown in Fig. 7.

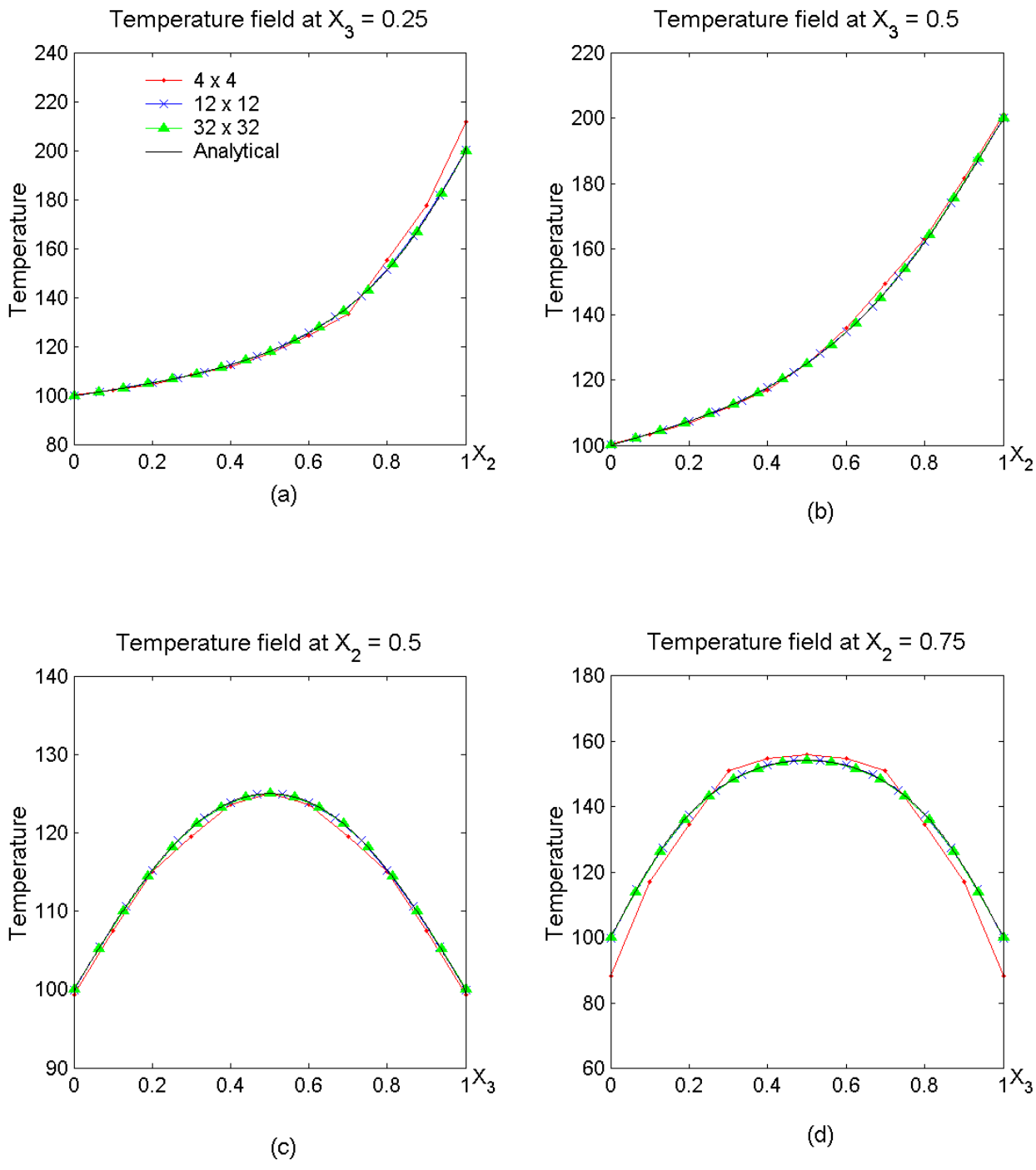

Fig. 12. Convergence studies for averaged interfacial temperature distributions along the cross-sections shown in Fig. 7, and comparison with analytical solutions.

into 25×25 subcells of uniform size. In the first case, Fig. 13 (a), the block is subjected to a temperature of $100°C$, which is held constant, at the left, top and bottom faces and a temperature of $200°C$ at the right face. The thermal conductivity k $(W/m-°C)$ is assumed to be exponentially increasing in the x_2 direction according to the function

$$k(x_2) = \frac{1}{2}e^{5x_2} \tag{203}$$

In the second case, Fig. 13 (b), the applied temperature boundary conditions remain the same but the thermal conductivity k is assumed to be exponentially decreasing in the x_2 direction according to the function

$$k(x_2) = 60e^{-5x_2} \tag{204}$$

In the third and fourth cases, the block is subjected to a temperature of $100°C$, which is held constant, at the left and top faces, and a temperature of $200°C$ at the right and bottom faces. The thermal conductivity k is assumed to be vary exponentially in both the x_2 and x_3 directions according to the functions

$$k(x_2, x_3) = 10e^{-2x_2+2x_3} \tag{205}$$

and

$$k(x_2, x_3) = 10e^{2x_2-2x_3} \tag{206}$$

4.2.1 Reformulated HOTFGM and finite-element comparison

The temperature field calculated using the reformulated version of the higher-order theory is compared with the finite-element solution. The finite-element solution was obtained by simulating the above cases in ANSYS using 8-node thermal elements called Plane77. The mesh discretization used in the finite-element analysis is the same as that used in the reformulated higher-order theory. Also, the Plane77 element in ANSYS has the same order (quadratic) of temperature field approximation as in the reformulated higher-order theory. For the first case, Fig. 13 (a), the temperature field contour plots obtained using the reformulated higher-order theory and ANSYS are shown in Figs. 14 (a) and (b), respectively. For the second case, Fig. 13 (b), the temperature field contour plots obtained using the reformulated higher-order theory and ANSYS are shown in Figs. 14 (c) and (d), respectively. For the third case, Fig. 13 (c), the temperature field contour plots obtained using the reformulated higher-order theory and ANSYS are shown in Figs. 15 (a) and (b), respectively. Finally, for the fourth case, Fig. 13 (d), the temperature field contour plots obtained using the reformulated higher-order theory and ANSYS are shown in Figs. 15 (c) and (d), respectively.

As observed in the contour plots, the temperature fields obtained from the reformulated higher-order theory and the finite-element analysis match very closely. However, at the points with the coordinates $(1, 0)$ and $(1, 1)$, which are the points of temperature discontinuity, the temperature field obtained from reformulated higher-order theory shows better convergence than the finite-element solution. This is because the boundary conditions in the higher-order theory are applied in a surface-average sense, whereas in the finite-elements the boundary conditions are applied at the nodes. Therefore, higher mesh refinement is required at the points of temperature discontinuity in the finite-element case for this particular choice of element.

4.2.2 Effect of thermal conductivity variation

According to the Fourier's law of heat conduction, the heat flux is in the direction of the negative temperature gradient. Moreover, the temperature field is modulated by the variation in thermal

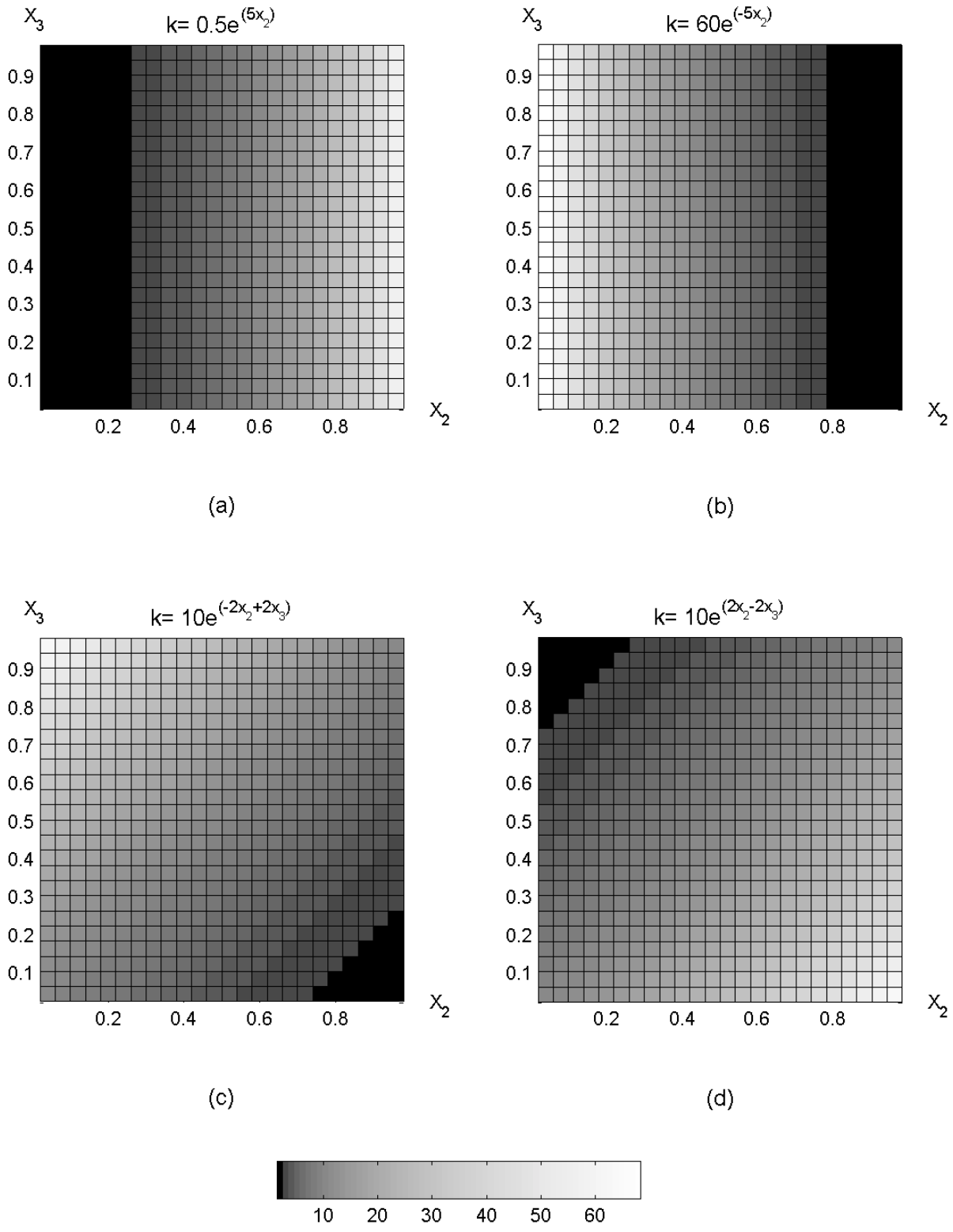

Fig. 13. Different thermal conductivity variations and mesh discretizations used for validation studies: thermal problem.

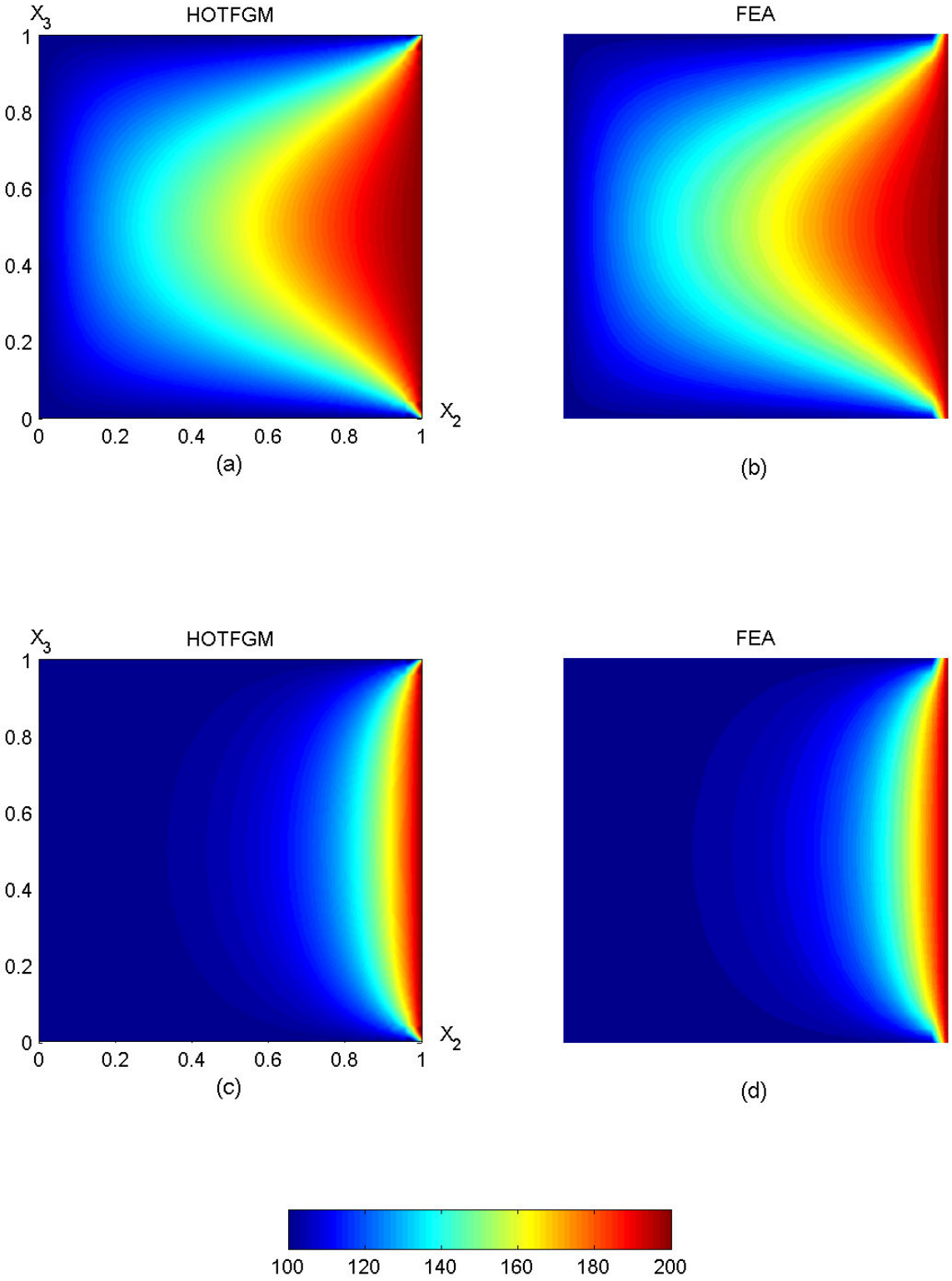

Fig. 14. Temperature field comparison obtained using HOTFGM and FEA for thermal conductivity variations in x_2 direction.

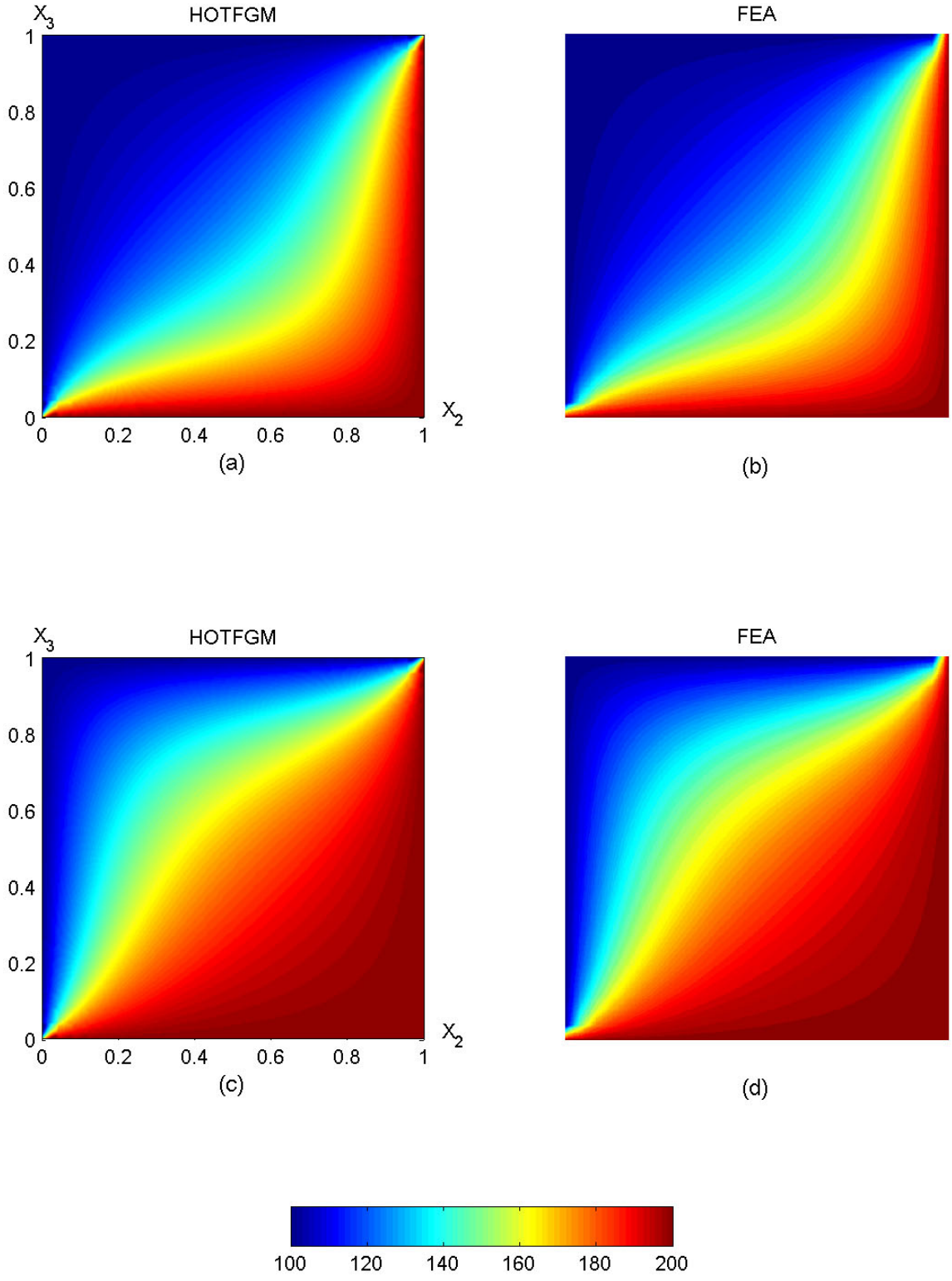

Fig. 15. Temperature field comparison obtained using HOTFGM and FEA for thermal conductivity variations in both x_2 and x_3 direction.

conductivity. Increasing the thermal conductivity in a particular direction shifts the temperature field towards the opposite direction, thereby decreasing the temperature gradient and vice-versa.

The temperature field for the same geometry and boundary conditions as in the first and the second case discussed in this subsection, but for the homogeneous material, was presented in Fig. 8 (d). In the first case, increasing the thermal conductivity in the x_2 direction shifts the temperature field in the negative x_2 direction, Fig. 14 (a), relative to the homogeneous case. In the second case, on the other hand, decreasing the thermal conductivity in the x_2 direction shifts the temperature field in the positive x_2 direction, thereby increasing the temperature gradient near the right face of the block, Fig. 14 (c). Similar behavior is observed for the two-dimensional variation of thermal conductivity shown in Figs. 15 (a) and (c).

4.3 Validation: Mechanical Problem

In Subsections 4.1 and 4.2, mesh sensitivity and validation studies were conducted for thermal cases with both homogeneous and heterogenous materials. In this subsection, the classical Eshelby problem for the pure mechanical loading is considered. This problem involves an elliptical fiber inclusion in an infinite matrix with uniform surface tractions applied over the boundaries at infinity.

Here, for the purpose of comparison, a circular inclusion is considered instead of an elliptical one and plane strain analysis is carried out. The matrix is assumed to be made up of epoxy and its cross-section has unit dimensions in the $x_2 - x_3$ plane. A very small glass fiber is embedded in the matrix so that the matrix practically behaves as infinite and the effects of the fiber inclusion's presence on stresses are not felt near the edges. The material properties of glass and epoxy used in the analysis are listed in Table 1. The matrix is subjected to normal surface tractions of unit magnitude in the x_2 direction at the outer faces as shown in Fig. 16 (a).

Material	$E\ (GPa)$	ν
Glass fiber	69.0	0.2
Epoxy matrix	4.8	0.34

Table 1. Material properties of constituent fiber and matrix phases.

Because of the type of boundary conditions and the investigated geometry, the problem is symmetric about the cross-sections along the lines $x_2 = 0.5$ and $x_3 = 0.5$. The mid-points along the lines $x_2 = 0, 1$ and $x_3 = 0, 1$ are not expected to move in the x_3 and x_2 directions, respectively. Therefore, in order to prevent rigid body motion, the middle two subcells along the lines $x_2 = 0$ and $x_3 = 0$ were constrained from moving in the x_3 and x_2 direction, respectively.

The full mesh used in the reformulated higher-order theory is shown in Fig. 16 (a). In order to capture the high stress gradients near the interface of the glass fiber and epoxy matrix, which occur due to the large material property mismatch between the two materials, very refined mesh was used in the interface's vicinity. In order to clearly see the refined mesh near the inclusion, the magnified mesh discretization is shown in Fig. 16 (b).

Stress contours obtained using the reformulated higher-order theory are shown in Figs. 17 (a), (c) and (e) and compared with the analytical solution (cf., Dugdale and Ruiz (1971)) in Figs. 17 (b), (d) and (f), respectively. As observed from the contour plots, the reformulated higher-order theory results match the exact analytical results very closely, both qualitatively and quantitatively. The normal stress contour plots obtained from the reformulated higher-order theory are perfectly symmetric about the horizontal and the vertical lines passing through the center of

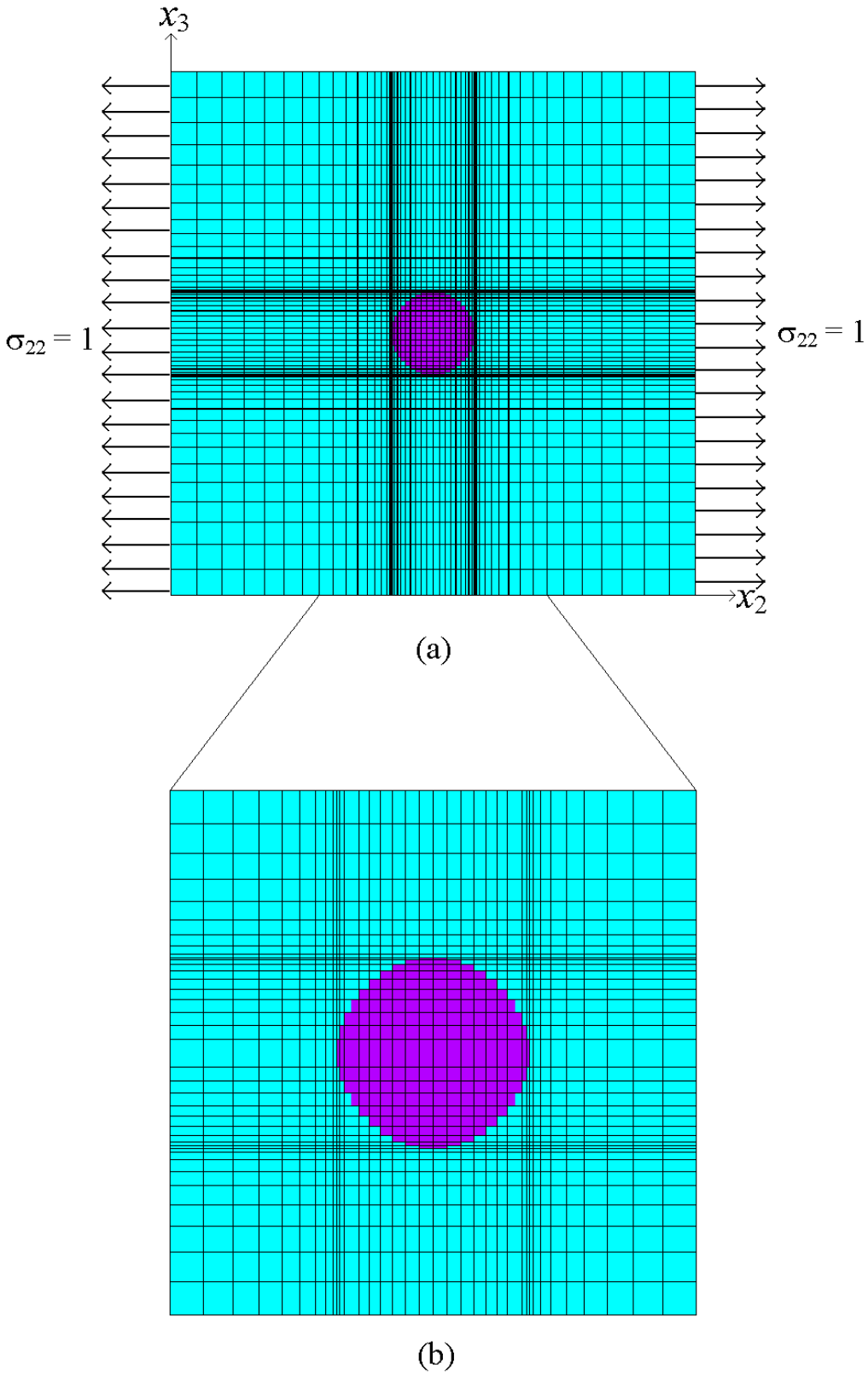

Fig. 16. Boundary conditions and mesh discretization for the Eshelby problem.

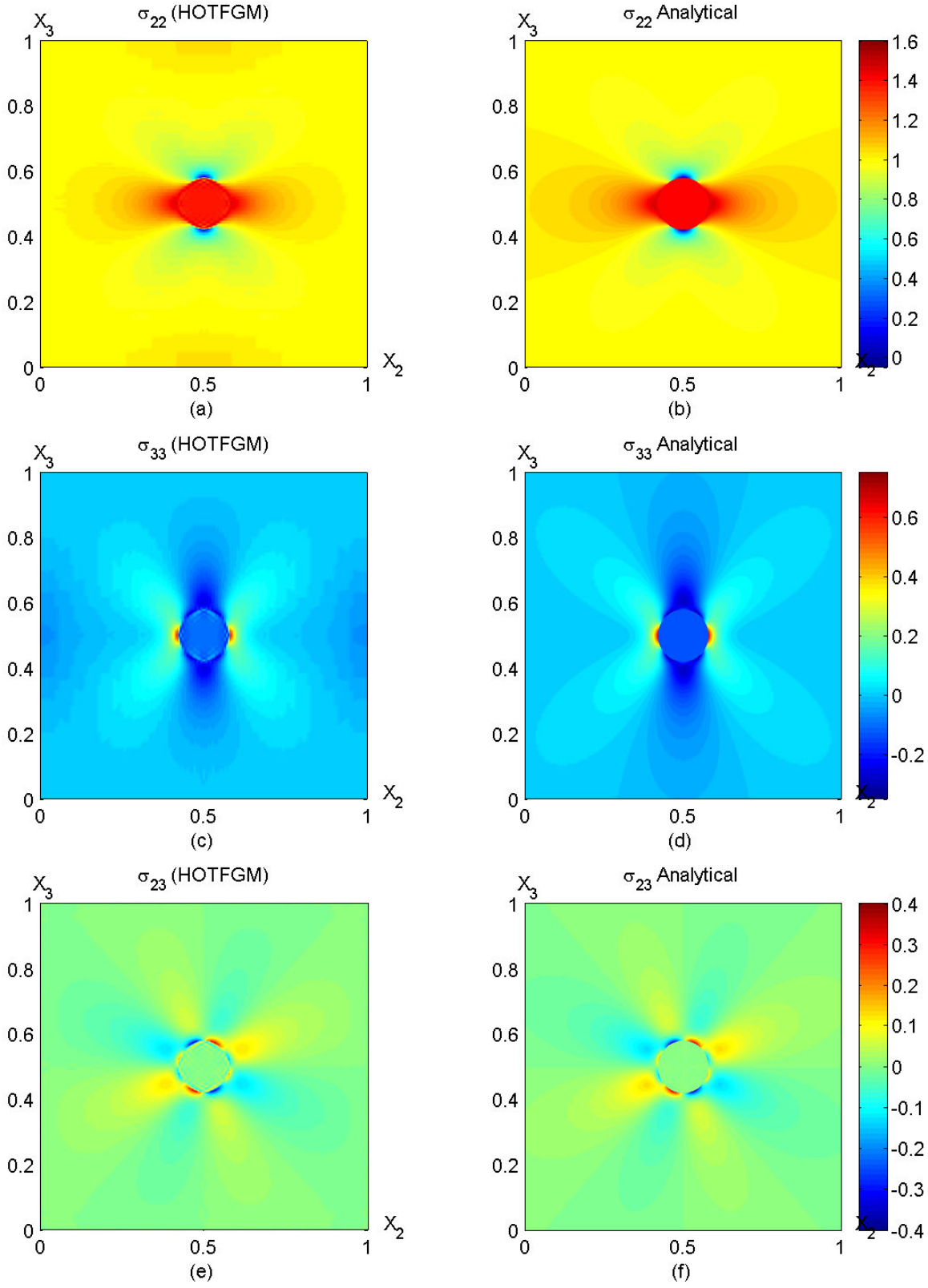

Fig. 17. Comparison of stress fields obtained using HOTFGM and analytical solutions.

the fiber inclusion as they ought to be due to the symmetry of the problem about these lines. Also, the normal stresses are nearly uniform in the fiber and the shear stress is nearly zero. The stress fields in the vicinity of the fiber are almost the same as those of the exact analytical solution.

The higher-order theory is sometimes confused with the finite-element technique. To demonstrate that the two approaches are fundamentally different, a finite-element solution was developed for the above problem. The same mesh was generated in ANSYS using 2-D structural 4-node (Plane182) and 2-D structural 8-node (Plane183) elements with unit negative pressure applied along $x_2 = 0, 1$. Plane182 elements use a bilinear approximation of the displacement field while Plane183 elements have the same order (quadratic) displacement field approximation as in the reformulated higher-order theory. The middle nodes along $x_2 = 0, 1$ and $x_3 = 0, 1$ were constrained from moving in the x_3 and x_2 directions, respectively, in order to prevent rigid body motion. Stress contour plots generated using the reformulated higher-order theory and finite-element analysis based on the 8-noded elements are compared in Fig. 18. The results are plotted using the same color scale and are magnified by 250 percent in order to compare the stresses in the vicinity of the fiber inclusion more closely. As observed in these plots, the finite-element solution picks up local stress concentrations at the interfacial subcell corners while, as seen in Fig. 17, the reformulated higher-order theory does not pick these stress concentrations and compares well with the actual solution. Further, the traction quantities are not continuous along the element interfaces in the finite-element case while they are continuous along the subcell interfaces in the reformulated higher-order theory. Finally, the stress components are not fully uniform within the fiber in the finite-element case. Table 2 lists the maximum and the minimum stresses obtained from the analytical, reformulated higher-order theory and the finite-element solutions. As observed in Table 2, the stress concentrations picked in the finite-element analysis based on the 4-noded elements are smaller than the ones picked up by the 8-noded elements and hence closer to the actual solution. However, the 4 -noded element assumes a bilinear variation of displacement field while the 8-noded element assumes a quadratic variation. Hence, the results from the 8-noded element based analysis should be compared with the actual solution because of the higher-order field approximation. In the finite-element case, these stress concentrations are picked up because the circular inclusion has been approximated by a stair-case pattern shown in Fig. 16 (b).

(MPa)	Analytical	HOTFGM	FEA (4-node)	FEA (8-node)
$\sigma_{22}^{\max}$	1.49	1.58	2.52	2.94
$\sigma_{22}^{\min}$	0.05	-0.027	0.02	0.08
$\sigma_{33}^{\max}$	0.68	0.72	0.68	0.64
$\sigma_{33}^{\min}$	-0.35	-0.3	-0.63	-1.65
$\sigma_{23}^{\max}$	0.37	0.36	0.25	0.72
$\sigma_{23}^{\min}$	-0.37	-0.36	-0.25	-0.72

Table 2. Comparison of maximum and minimum stresses obtained using analytical, HOTFGM and FEA approaches.

Further, in the finite-element case, the continuity of displacements is satisfied in a point-wise manner (at the nodes) and therefore, the exact details of the geometry are important in order to obtain converged results. This was demonstrated by generating the exact circular inclusion shape

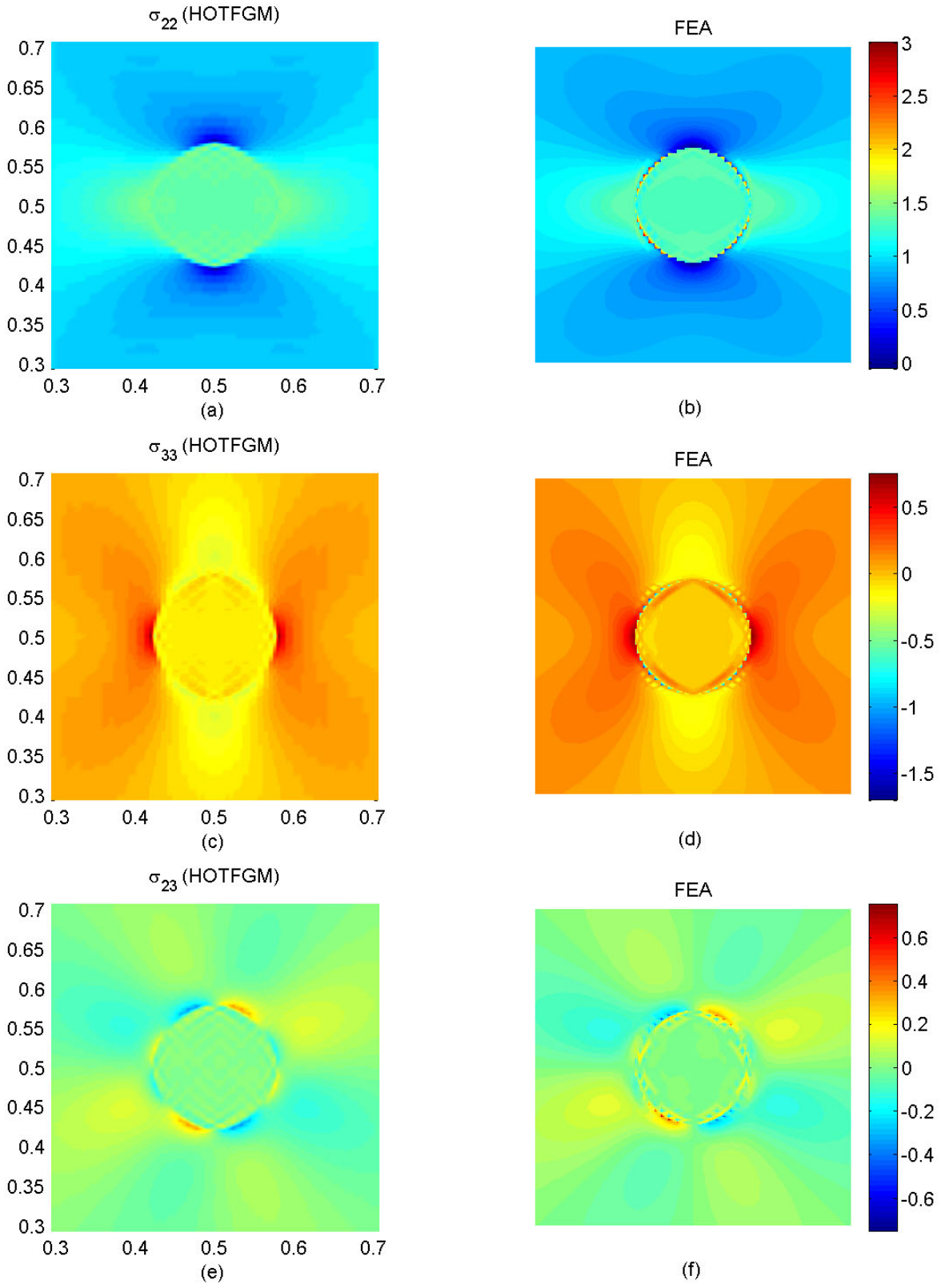

Fig. 18. Comparison of stress fields obtained using HOTFGM and FEA.

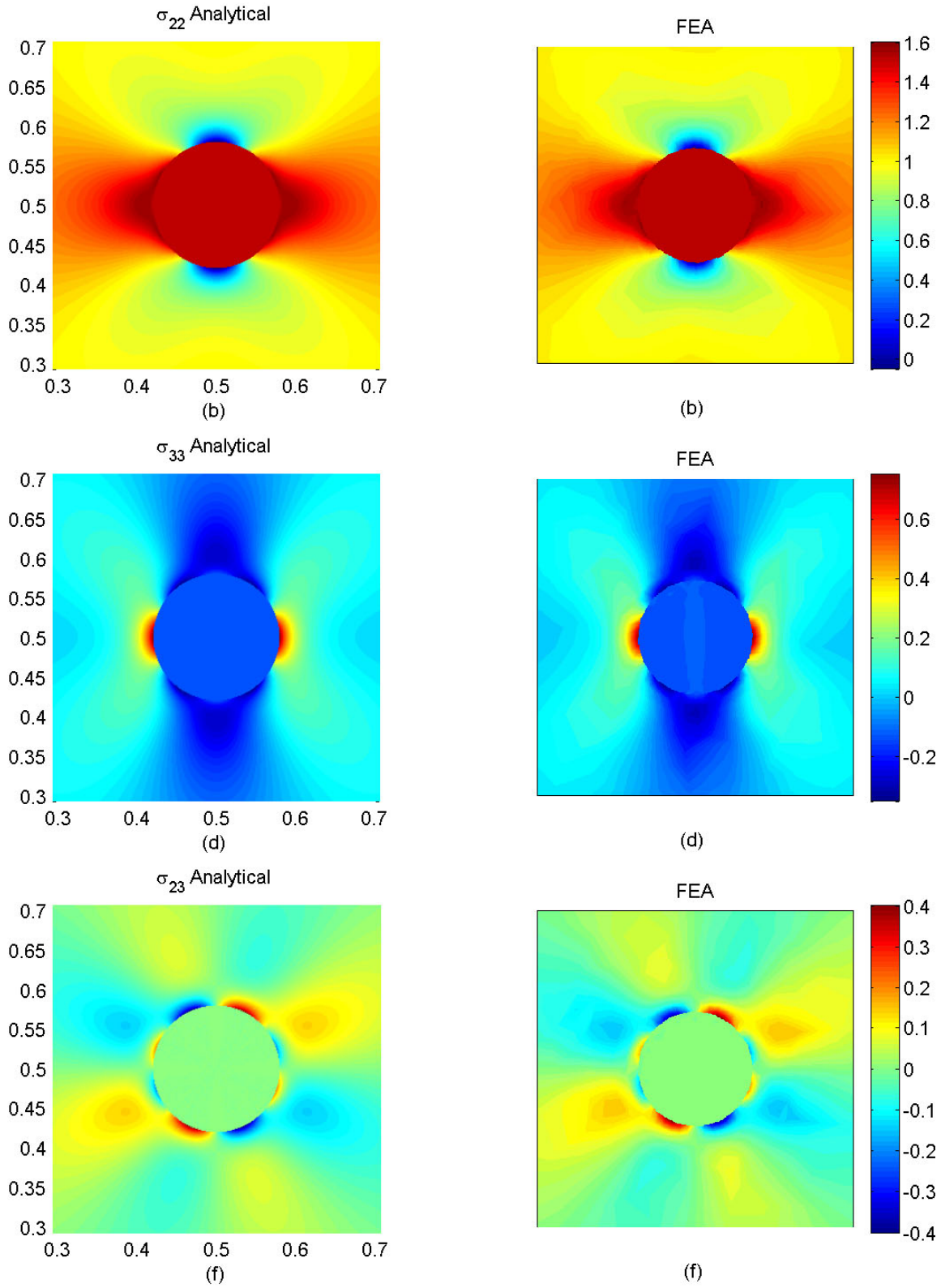

Fig. 19. Comparison of stress fields obtained using FEA with exact circular inclusion and analytical solutions.

using 8-noded (Plane183) elements in ANSYS. A total of 1045 elements was used in the analysis. The results obtained for this case are plotted in Fig. 19 and compared with the analytical results. As seen in Fig. 19, the results obtained using the finite-element analysis for the exact inclusion geometry match the actual analytical results both qualitatively and quantitatively. In the reformulated higher-order theory, the displacement/traction continuity conditions are applied in a surface-averaged sense and therefore the various field quantities are blurred acrss the interfaces. An approximation of the inclusion geometry produces good results. This is very useful in analyzing practical problems where modeling the exact geometry can be very demanding.

4.4 Validation: Combined Thermomechanical Case

In this subsection, a combined thermomechanical case is considered. The effect of temperature increase on a constrained geometry is studied and the results obtained from the reformulated higher-order theory are compared with finite-element analysis. The investigated geometry and the thermal boundary conditions are the same as those considered in Subsection 4.1 and are shown again in Fig. 20 (a) for convenience. The block is considered to be made up of aluminium and the material properties used for the analysis are listed in Table 3. The mechanical constraints imposed are the fixidity of the left and the right face of the block.

Material	$k\ (W/m-{}^\circ C)$	$E\ (GPa)$	ν	$\alpha\ \times 10^{-6}\ (/{}^\circ C)$
Aluminum	220	72.4	0.33	22.5

Table 3. Material properties used for the combined thermomechanical analysis.

The cross-section of the block in the $x_2 - x_3$ plane was initially discretized into 32×32 subcells of uniform size as shown in Fig. 20 (b). This discretization was shown to be satisfactory in dealing with the thermal problem in Subsection 4.1. As the gradients of various mechanical field quantities are expected to be higher around the corners, the mesh should be more refined in the regions of higher gradients. Therefore, another discretization with the same number of subcells but with the mesh refined around the corners was also considered as shown in Fig. 20 (c). In order to compare with finite-element results, the same mesh (32×32, non-uniform, Fig. 20 (d)) was created in ANSYS.

The temperature, displacement and stress field contour plots obtained using the reformulated higher-order theory and finite-element analysis for the graded (refined around the corners) mesh are shown in Figs. 21 and 22. As observed from the contour plots, the temperature and the displacement field obtained using the two approaches are visually indistinguishable. The stress field contour plots generated using the two methods also match very closely except at the corners. The maximum and minimum stresses are obtained at the corners and their magnitudes predicted by the reformulated higher-order theory and the finite-element analysis are different as shown in Table 4. No consistent trend is observed from these magnitudes. The normal stresses predicted by finite-element analysis are higher than the higher-order theory results, while the shear stress predicted by the higher-order theory is higher than the finite-element result. A thorough ANSYS analysis showed that these stress magnitudes (at the corners) do not converge with any amount of mesh refinement but continue to increase as the mesh is refined further and further. This is most likely due to the singular behavior at the corners which occurs because of the applied mechanical boundary conditions.

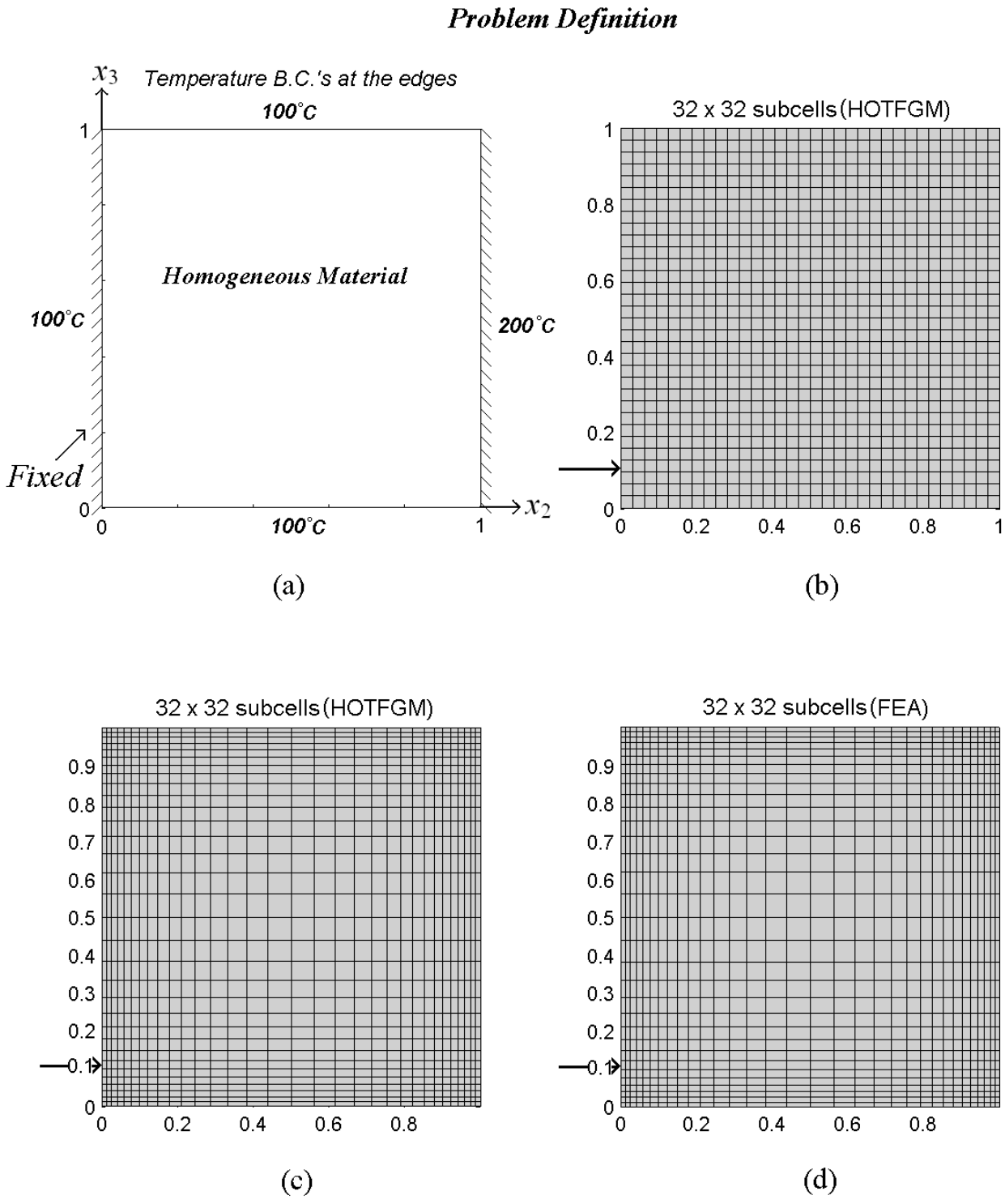

Fig. 20. Problem definition, investigated geometry and discretization used for validation studies: thermomechanical problem.

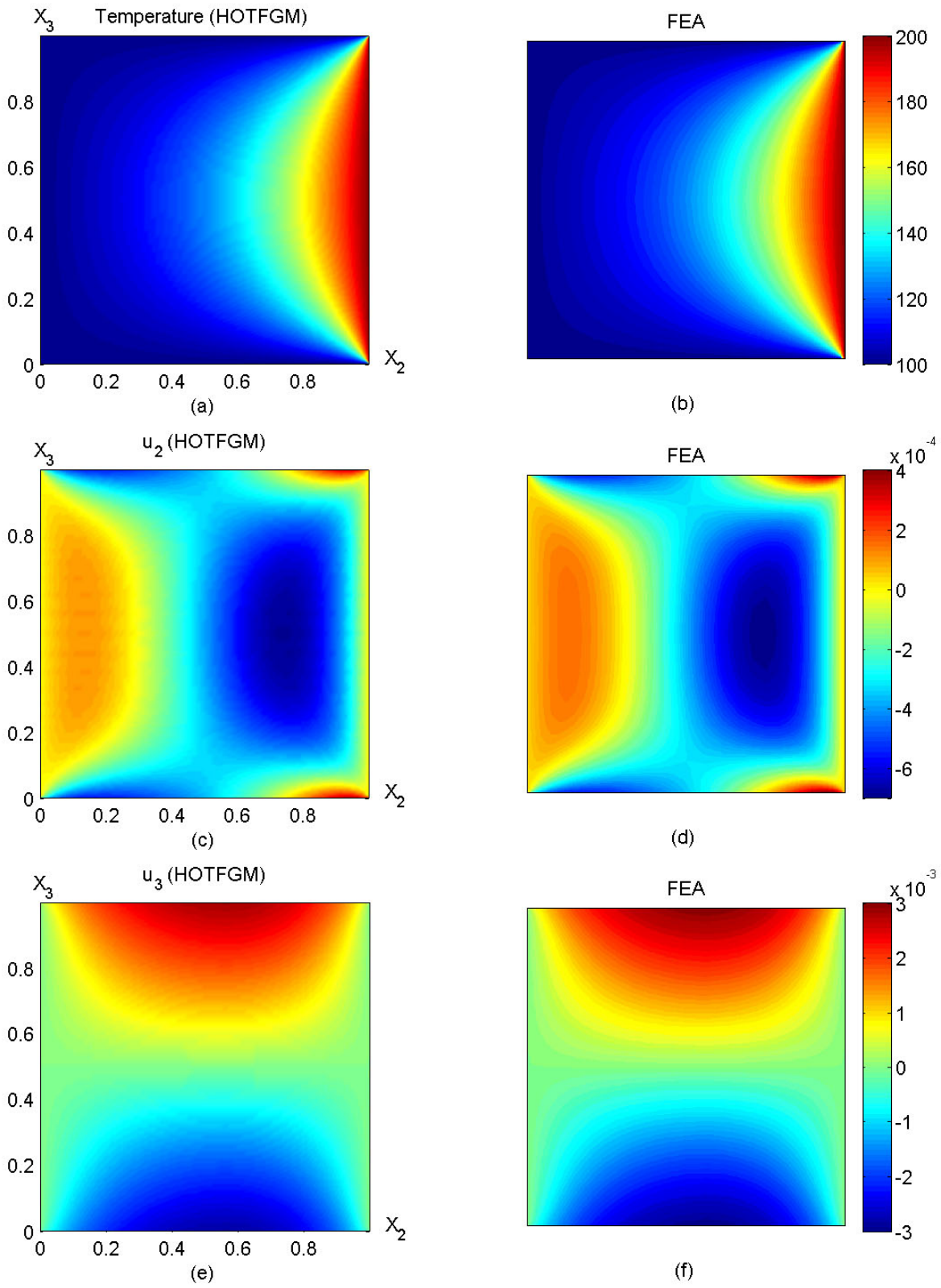

Fig. 21. Temperature and displacement field comparison obtained using HOTFGM and FEA for the homogeneous plate with fixed boundary conditions.

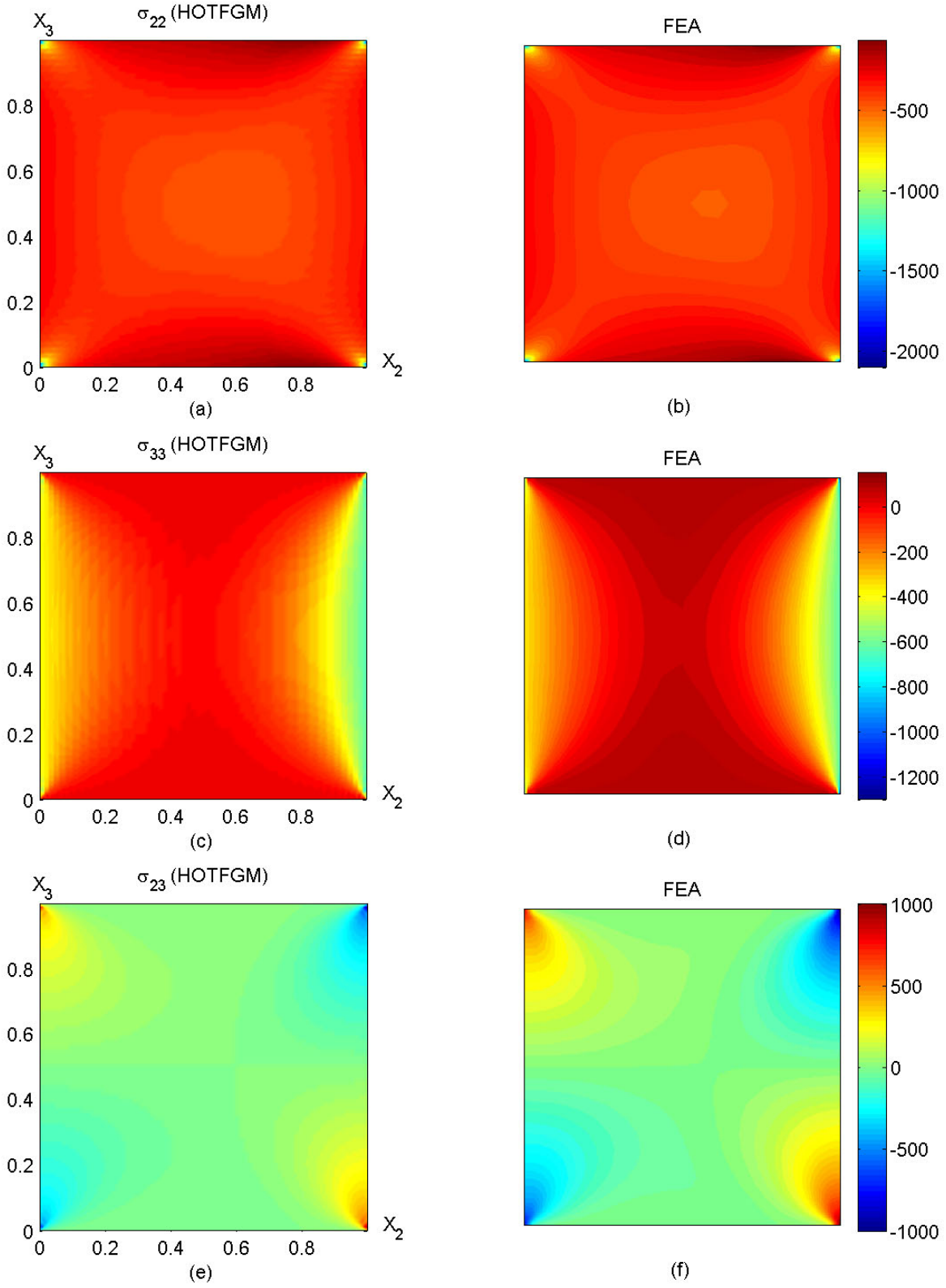

Fig. 22. Stress field comparison obtained using HOTFGM and FEA for the homogeneous plate with fixed boundary conditions.

(MPa)	HOTFGM	FEA
$\sigma_{22}^{\max}$	-83	-70
$\sigma_{22}^{\min}$	-1871	-2063
$\sigma_{33}^{\max}$	152	59
$\sigma_{33}^{\min}$	-715	-1253
$\sigma_{23}^{\max}$	963	608
$\sigma_{23}^{\min}$	-963	-608

Table 4. Comparison of maximum and minimum stresses obtained using HOTFGM and FEA approaches.

The various field quantities (temperature, displacements u_2 and u_3, and stresses σ_{22}, σ_{33}, and σ_{23}) were also plotted along the cross-section $x_3 = 0.1$ in order to demonstrate the advantages of refining the mesh in the regions of high gradients. The effect of uniform and non-uniform mesh is studied and the results are compared with the finite-element results in Fig. 23. From these cross-sectional plots, it is observed that the temperature and displacements converge with 32×32 subcells even for the uniform mesh case. However, the stresses are different for the uniform mesh case, especially near the corners. This is because of the higher gradients in these regions. The stresses are related to the derivatives of the displacement field and, therefore, the error in the stress field is expected to be higher than in the displacement field. The non-uniform mesh with 32×32 subcells converges better then the uniform 32×32 subcell mesh. This shows the advantages of effectively graded meshes. Therefore, an effective mesh should be created with relatively more subcells in the regions of high field gradients. As observed from the above cross-sectional plots, comparable results are obtained from the finite-elements and the reformulated higher-order theory for the graded mesh.

5 Application: Thermal Barrier Coatings

As described in Section 1, one of the most important applications of functionally graded materials is in the thermal protection systems such as thermal barrier coatings. In many practical applications such as aerospace engines, electronic circuit boards, packaging of chips, etc., the structures are subjected to very high thermal gradient loading. The metallic part in these structures yields when subjected to very high temperatures. In order to prevent this yielding, the metallic substrate is coated with a low conductivity ceramic layer to reduce the temperature to which the metal is exposed. These ceramic coatings of metallic substrates with an adhesive layer between the metal and ceramic regions, or the bond coat, are called thermal barrier coatings or TBCs.

Layers of bond coat and ceramic with sharp interfaces produce high interlaminar stresses at the edges which may lead to separation of these layers. Therefore, in order to prevent these free-edge interlaminar stresses, which occur due to large material property mismatch, the microstructure is gradually varied. There are various spray techniques such as plasma spray, flame spray, arc spray, etc., which are used in different industries for fabricating thermal barrier coatings. The metallic substrate is first sprayed with an adhesive which acts as a bond coat between the metal and the ceramic material, followed by the coating itself. These spray techniques can be very efficient in producing functionally graded microstructures for thermal barrier coatings.

Thermal barrier coatings can be analyzed by using either the uncoupled or the coupled approach as described in Section 1. In the uncoupled approach, the gradually varying microstructure is either

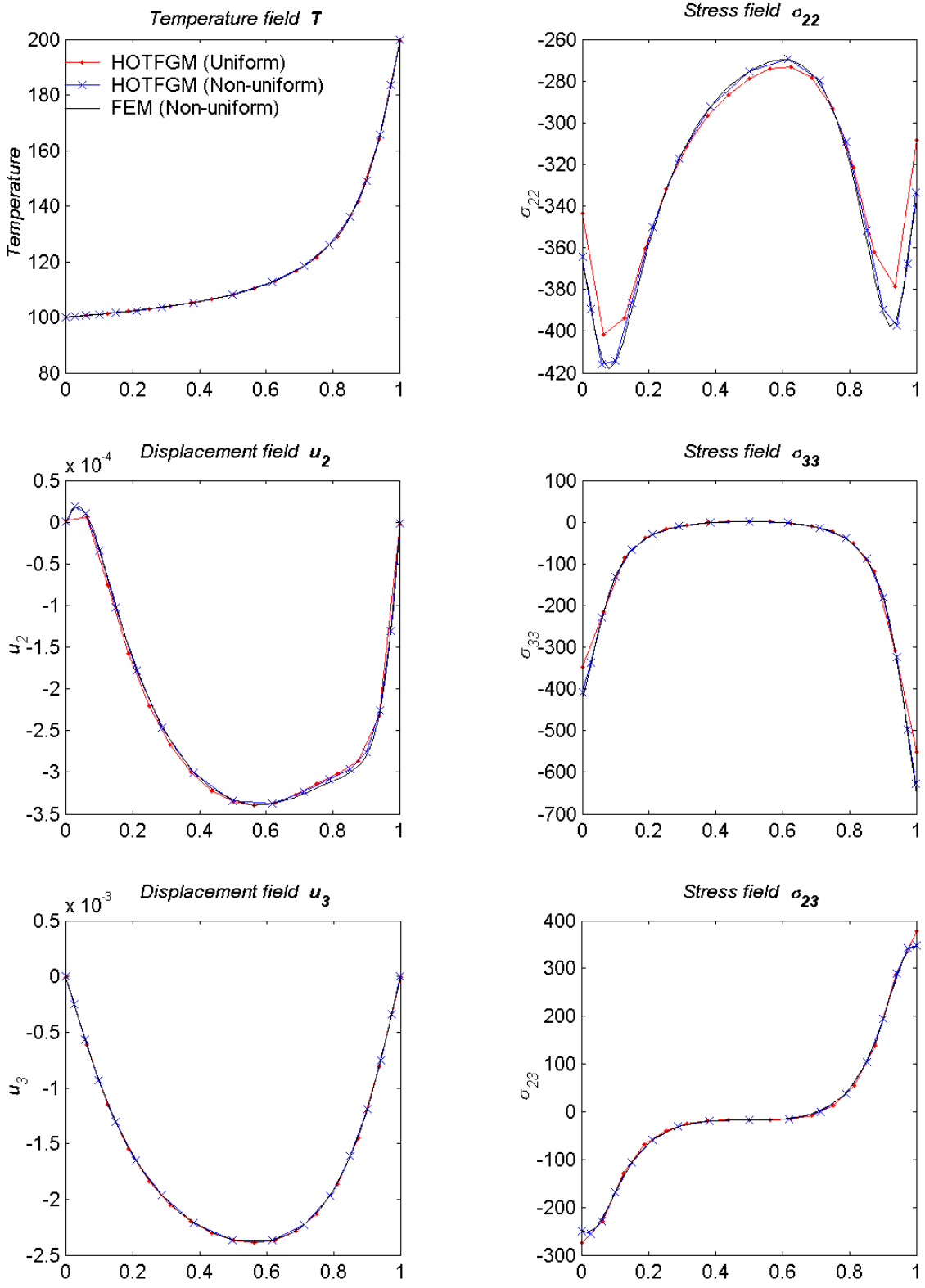

Fig. 23. Comparison of temperature displacement and stress distributions along $x_3 = 0.1$ obtained using HOTFGM and FEA.

assumed to be continuous function of spatial coordinates which best fits the given distribution or approximated by layers with constant homogenized properties. These homogenized properties are calculated using various micromechanical models. However, the uncoupled approach neglects the locally produced effects of microstructural gradation. Using the layered approach with homogenized properties may produce stress concentrations at the interfaces in the vicinity of free edge which would not otherwise occur in the actual microstructure.

In this section, a TBC with continuously varying microstructure is analyzed using the reformulated higher-order theory and the results are compared with finite-element analysis.

5.1 Problem Definition

The investigated geometry, microstructural gradation and the boundary conditions are shown in Fig. 24 (a). The cross-section of the TBC in the $x_2 - x_3$ plane has unit dimension in the x_3 direction and is twice as long in the x_2 direction. The cross-section is discretized into 120×60 subcells such that each subcell has an aspect ratio of one. The dimension of the block is considered infinite in the out of plane (x_1) direction and plane strain analysis is carried out. The thermal barrier coating is subjected to zero temperature at the bottom face and a concentrated temperature at the top. The left and the right faces are insulated against conduction (zero heat flux). At the top face, the temperature is assumed to vary with the x_2 coordinate according to the exponential function

$$T(x_2, 1) = 1325 \left(\cos |x_2 - 1|\right)^{20} + 25 \tag{207}$$

as shown in Fig. 24 (a). The temperature is calculated at the right corner of the top edge of each subcell and that constant value is applied at the top face of the subcell. The bottom face of the TBC is placed on rollers and the middle two subcells at the bottom are fixed in order to prevent rigid body motion. The bottom 12 rows of subcells ($\beta = 1, 2, .., 12,\ \gamma = 1, 2, ..., 120$) are assigned the properties of steel which is the substrate. The next 8 rows of subcells ($\beta = 13, 14, .., 20,\ \gamma = 1, 2, ..., 120$) are assigned the properties of the alloy CoCrAlY which acts as the bond coat adhesive. In the remaining 40 rows of subcells ($\beta = 21, 22, .., 60,\ \gamma = 1, 2, ..., 120$), the material properties are assigned such that the adhesive (CoCrAlY) lies at the bottom and the ceramic (zirconia) at the top with gradual variation from the bond coat to the ceramic top coat. The material properties used in the analysis are listed in Table 5. The volume fraction of the CoCrAlY bond coat is plotted as a function of x_3 in Fig 24 (b), showing the gradually changing microstructure.

Material	$k\ (W/m - °C)$	$E\ (GPa)$	ν	$\alpha\ \times 10^{-6}\ (/°C)$
Steel	60.5	207	0.33	15
CoCrAlY	2.42	197	0.25	11
Zirconia	0.5	36	0.2	8

Table 5. Material properties used for the thermal barrier coating application.

5.2 HOTFGM and Finite-Element Comparison

For the given geometry, microstructure and boundary conditions, the various field quantities (temperature, displacements u_2 and u_3, stresses σ_{22}, σ_{33} and σ_{23}) were generated using the reformulated higher-order theory and are shown in Figs. 25 (a) - 30 (a). The various field quantities were also calculated using the finite-element method in order to compare the reformulated higher-order theory results. The finite-element solution was obtained by generating the same mesh and microstructure

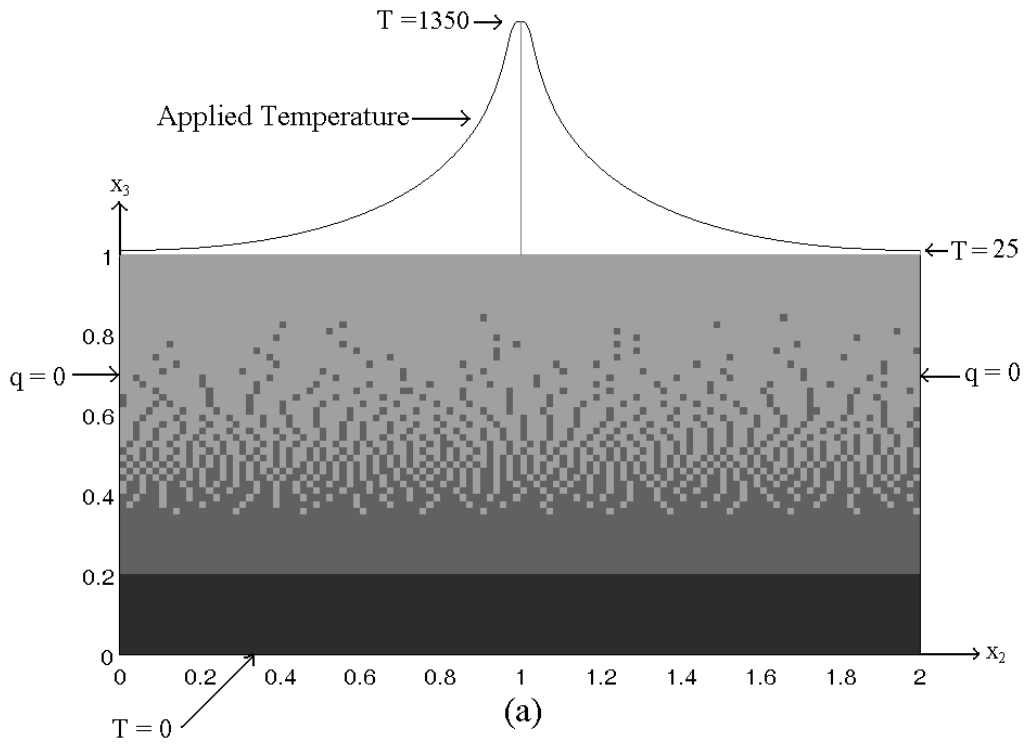

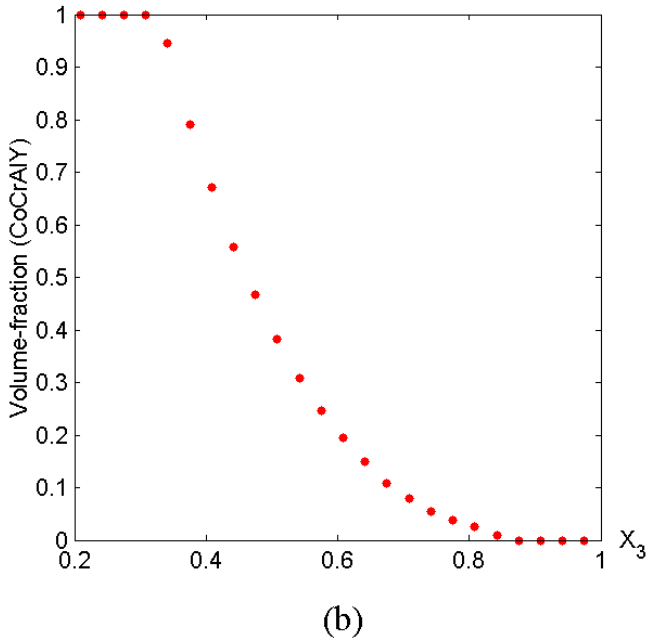

Fig. 24. Problem defintion, investigated geometry and material gradation used for TBC application.

in ANSYS using 2-D coupled field, 4-node (Plane13) elements. In the finite-element case, the temperature applied at the top face is calculated at the nodes using the assumed exponential function. The bottom face is constrained to move in the x_3 direction and the middle node at the bottom is fixed in order to prevent rigid body motion. The generated contour plots for the various field quantities are shown in Figs. 25 (b) - 30 (b). Also, the maximum and the minimum values of the various field quantities are listed in Table 6.

	Maximum		Minimum	
	HOTFGM	FEA	HOTFGM	FEA
u_2	0.0023	0.0022	-0.0023	-0.0022
u_3	0.0035	0.0034	0	0
σ_{22}	103.7	107.9	-140.8	-225.6
σ_{33}	71.5	105.4	-186.6	-217.2
σ_{23}	70.1	86.7	-70.9	-84.7

Table 6. Comparison of maximum and minimum displacements and stresses obtained using HOTFGM and FEA approaches.

As observed in the contour plots, Figs. 25 - 27, and also in Table 6, the temperature and displacement fields obtained from the reformulated higher-order theory and the finite-element analysis match very closely. However, the stress values obtained using the two approaches are considerably different in the graded region, eventhough the general distributions are similar. In the finite-element case, the stresses across the interfaces of the elements vary considerably as observed from the contour plots in Figs. 28 (b) - 30 (b). The σ_{22} and σ_{23} stress components are the traction components along the vertical interfaces of the subcells and σ_{23} and σ_{33} are the traction components along the horizontal interfaces of the subcells. These traction quantities are expected to be approximately continuous from one subcell or element to another. In the reformulated higher-order theory, the traction quantities are continuous across the subcell interfaces. In the finite-element case, on the other hand, the difference in these tractions across the interfaces of the elements, particularly in the graded region, is very high, which demonstrates that the stress field has not converged. This is partly due to the continuity of tractions/displacements which is explicitly applied (in a surface-average sense) across the subcell interfaces in the reformulated higher-order theory. In the finite-element case, continuity of displacements is explicitly applied in a pointwise manner (at the nodes) and then the potential energy is minimized in order to obtain the displacement and stress fields. Therefore, in the finite-element case, a more refined mesh is required in order to get converged solution for the stresses. Also, as observed in the stress contour plots, the boundary conditions are somewhat better satisfied by the reformulated higher-order theory.

6 Conclusions and Future Work

6.1 Conclusions

An efficient reformulation of the higher-order theory for functionally graded materials for two-dimensional thermoelastic problems has been successfully developed. The subcell microvariables, which were the basic unknowns in the original higher-order theory, were expressed in terms of the interfacial surface-averaged quantities (temperatures and displacements) and these interfacial surface-averaged quantities were considered to be the basic unknown quantities in the reformulation. The

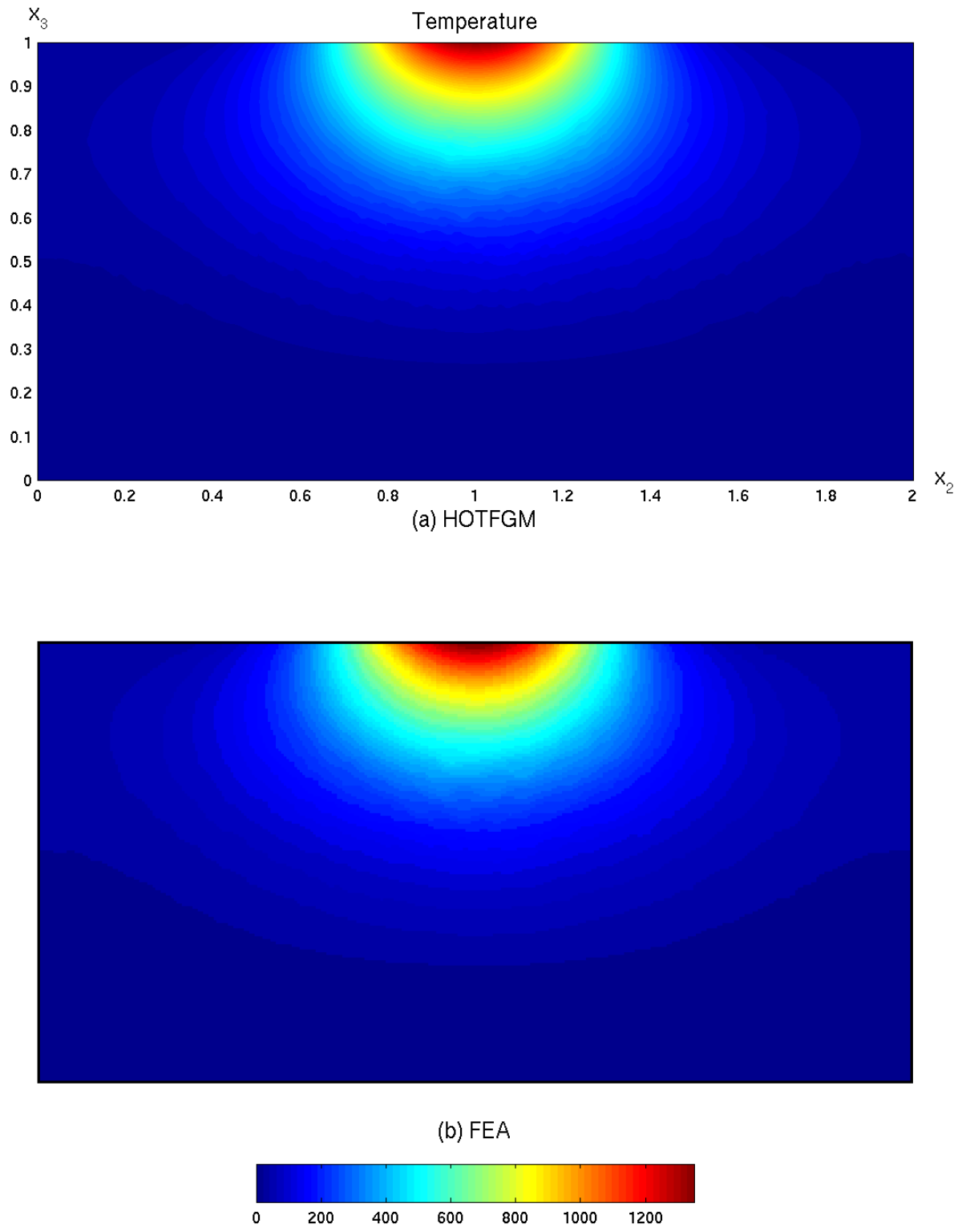

Fig. 25. Temperature field for TBC application obtained using HOTFGM and FEA.

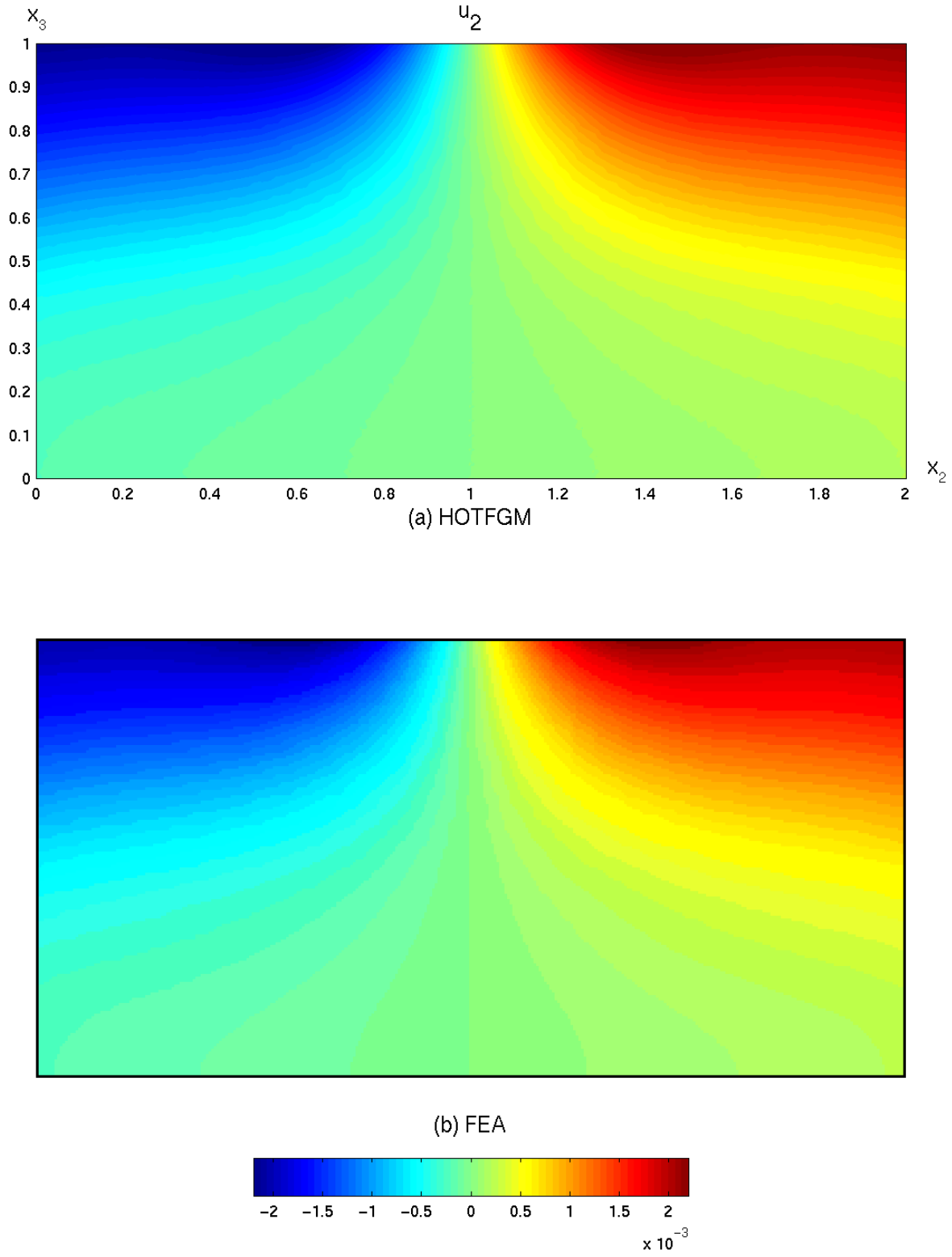

Fig. 26. Displacement field u_2 for TBC application obtained using HOTFGM and FEA.

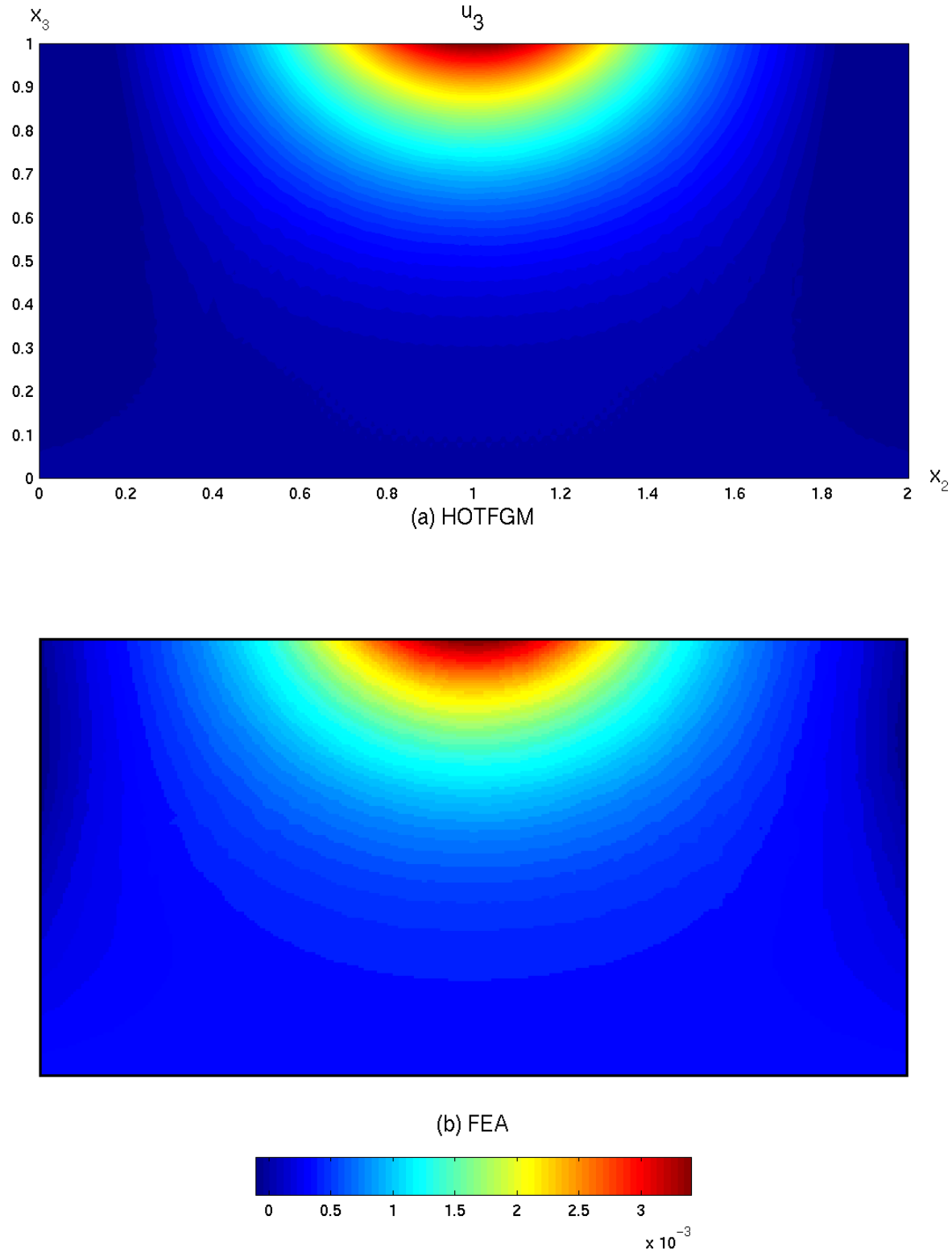

Fig. 27. Displacement field u_3 for TBC application obtained using HOTFGM and FEA.

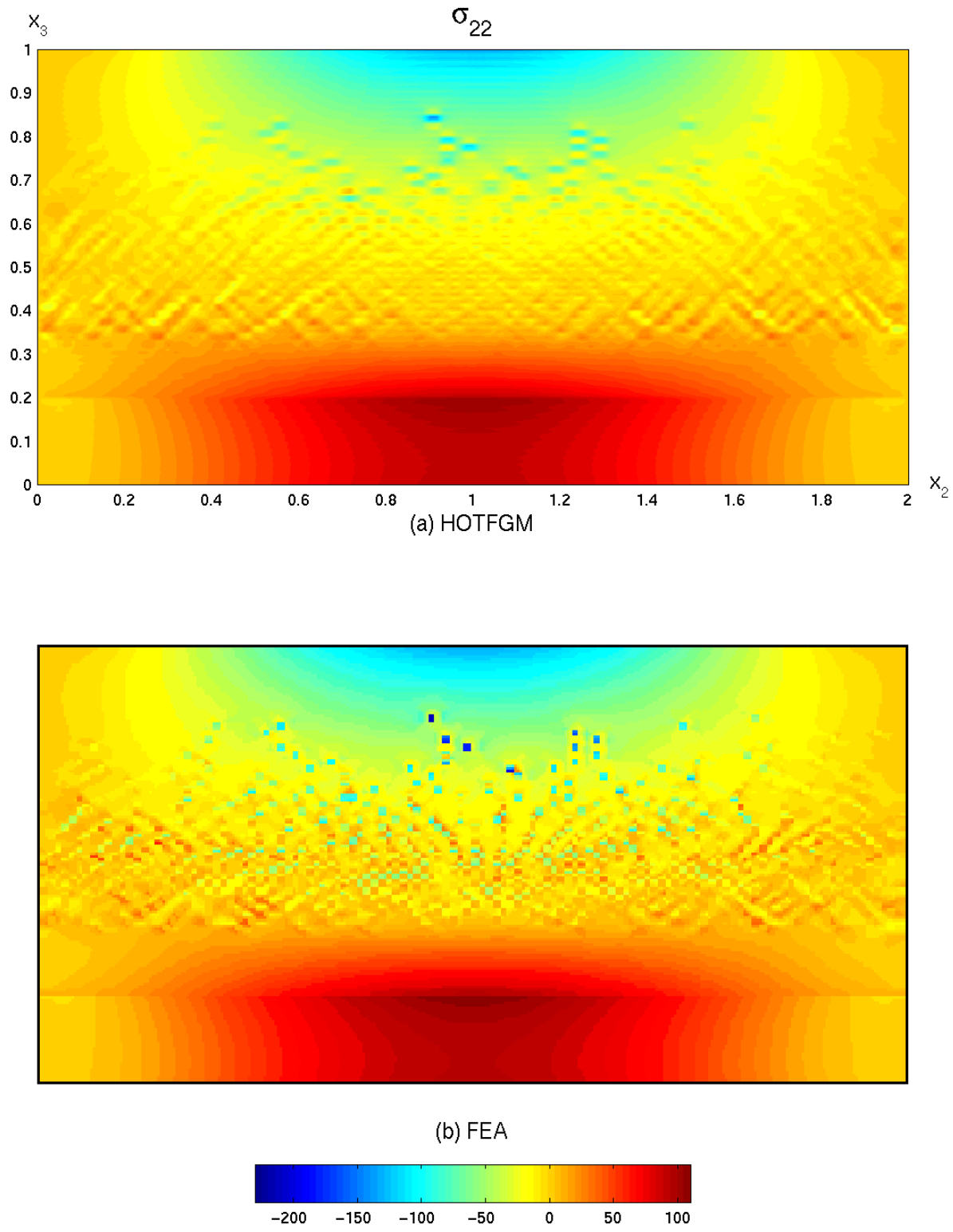

Fig. 28. Stress field σ_{22} for TBC application obtained using HOTFGM and FEA.

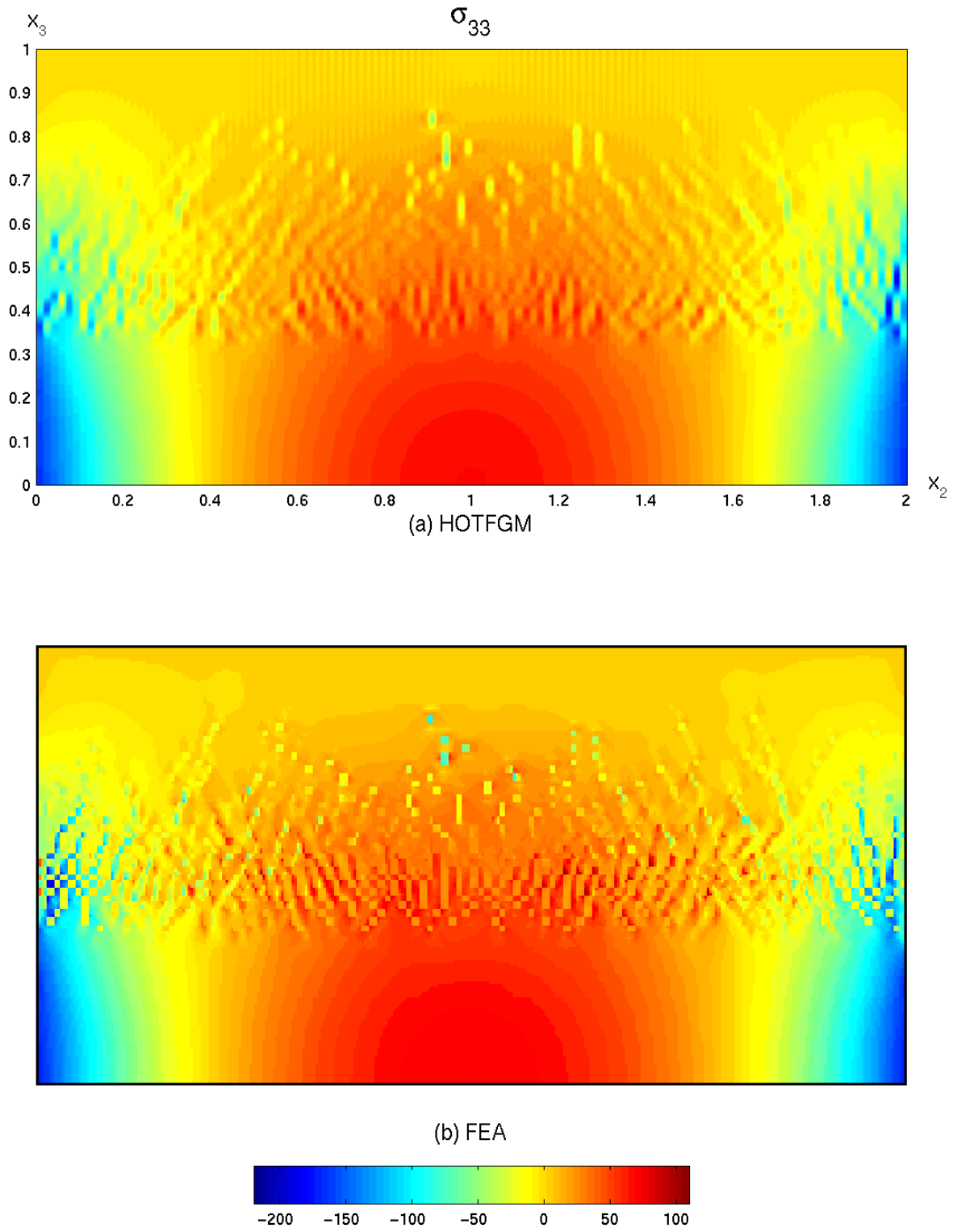

Fig. 29. Stress field σ_{33} for TBC application obtained using HOTFGM and FEA.

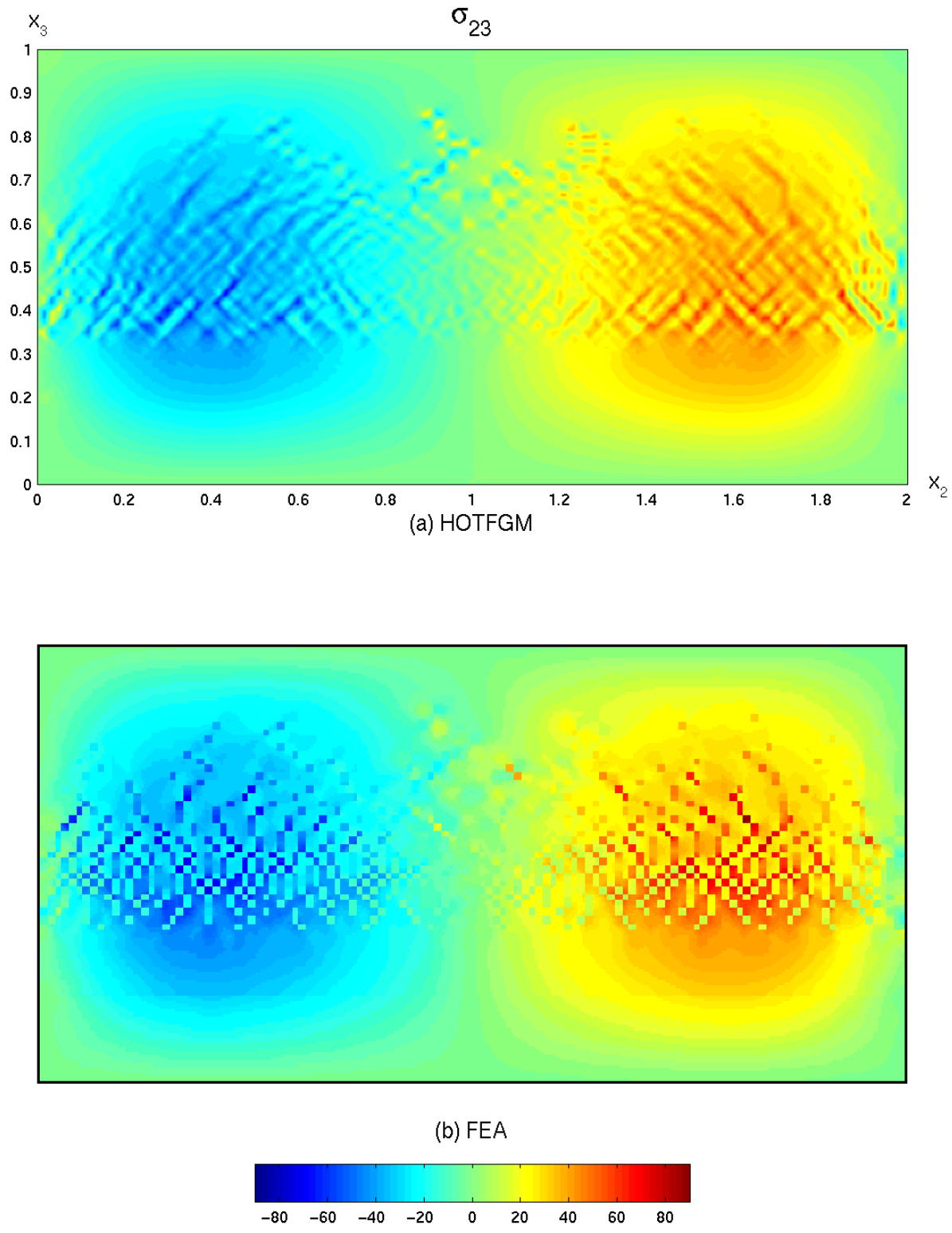

Fig. 30. Stress field σ_{23} for TBC application obtained using HOTFGM and FEA.

local-global conductivity and local-global stiffness matrix approach was used in order to eliminate redundant equations. This resulted in the reduction of the size of the global conductivity and stiffness matrices by approximately sixty percent. The reduction in the number of equations has enhanced the theory's capability to analyze computationally intensive and demanding cases. Problems requiring greater mesh discretization (large number of subcells) which could not be analyzed using the original higher-order theory because of the large number of equations involved are now solvable with the reformulated higher-order theory.

Mesh sensitivity and validation studies were carried out for various thermal, mechanical and combined thermomechanical cases. A practical application of the thermal barrier coating was also analyzed. The results were compared to analytical and finite-element solutions for the various cases.

From the mesh sensitivity studies, it was observed that the temperature field converges very quickly with mesh refinement and the temperature distribution can be accurately captured using a relatively coarse mesh, especially for problems involving homogeneous materials. Also, averaging the temperature across subcell interfacial lines calculated using subcell microvariables on each side of the interface produces better results.

A functionally graded case with thermal conductivity varying according to an exponential function was considered and thermal analysis was carried out. The results obtained from the higher-order theory matched the finite-element analysis very closely. However, in the finite-element case the temperature field did not converge to the actual temperature field at the points of temperature discontinuity. A more refined mesh is required at these points in the finite-element case. On the other hand, the results obtained from the reformulated higher-order theory exhibited better convergence at these points.

In many practical problems, the mesh discretization required to simulate exact inclusion shapes can be very demanding. The Eshelby problem demonstrated the efficiency of higher-order theory in terms of mesh discretization approximation of the inclusion phase. It was observed that a decent approximation of the circular inclusion using a rectangular grid produced results which were comparable with the actual analytical solution. However, in the finite-element case, approximating an inclusion shape using the same mesh discretization picks up stress concentrations at the sharp edges which are not present in the actual solution. Therefore, a more refined mesh is required in order to properly approximate the shape of inclusions in the finite-element case.

A thermomechanical case involving a homogeneous plate was also analyzed. The results from the higher-order theory and the finite-elements matched very closely. The efficiency of using a locally refined mesh in the regions of high temperature and stress gradients was demonstrated.

In the thermal barrier coating application, it was observed that the temperature and displacement fields obtained using the reformulated higher-order theory and the finite-element approach were visually indistinguishable, in contrast to the stress fields. In the finite-element case, the tractions were not continuous across the element interfaces, especially in the graded region, and the boundary conditions were not as well satisfied. In the reformulated higher-order theory, on the other hand, the tractions were approximately continuous across the subcell interfaces and the boundary conditions were better satisfied. This demonstrated the efficiency of the higher-order theory in analyzing functionally graded microstructures. In the case of functionally graded materials analyzed using the finite-element approach, mesh discretization required for converged results can be computationally very demanding if the actual microstructural details are explicitly taken into account. In the finite-element case, displacement continuity is satisfied in a point wise manner and hence stress concentrations are picked up at the points of material discontinuity at sharp edges. However, in the higher-order theory, the continuity of tractions/displacements is applied in a surface-average sense. This smoothing operation produces sufficiently accurate solutions with relatively coarse meshes and approximate inclusion shapes.

6.2 Future work

The completed two-dimensional thermoelastic reformulation of the higher-order theory is useful for plane strain and generalized plane strain problems. In many practical applications, the type of problems encountered are not limited to two dimensions, however. Many cases involve out-of-plane loading conditions. Therefore, the next step is to extend the reformulation to three dimensions in order to analyze more general problems. Also, in cases involving traditional composites, the material is locally heterogeneous but globally periodic. Structural problems involving composites can be analyzed by homogenizing the material using the concept of a representative volume element or RVE. The effective properties of the locally heterogeneous RVE can be found using the homogenized version of the reformulated higher-order theory by applying periodic boundary conditions, and then the structure can be analyzed globally using the reformulated higher-order theory or other techniques. The second step, therefore, is to incorporate periodic boundary conditions and out-of-plane loading capabilities.

Generally, in practical problems encountered in the industry, deformations enter into the inelastic range at the point where the structure can still withstand considerably higher loads. Also, the loading history affects stresses and deformations to an extent that depends on the type of material. In order to carry out an optimum design of a structure, it is necessary to include these plastic and viscoelastic or viscoplastic effects and analyze the design taking into account such behavior. Therefore, viscoelastic, viscoplastic and plastic capabilities should be included in the reformulated higher-order theory.

Presently, material properties are considered to be constant within a subcell. The material properties can be assumed to be linear or higher-order in local coordinates depending on the actual gradation of the microstructure. This may potentially lead to further reductions in mesh discretization required to obtain converged solutions. The capability of having linearly varying material properties within a subcell has been incorporated by Zhong (2002) into the thermal portion of the reformulated higher-order theory. This will be extended to the mechanical portion.

The stringent environment and loading conditions to which structures are subjected may lead to the initiation of cracks. Another long-term goal is to include fracture mechanics capabilities in the reformulated higher-order theory in order to be able to analyze crack problems.

7 Appendix

The submatrix $A_2^{(\gamma)}$ used in the global thermal conductivity matrix assembly

$$\mathbf{A}_2^{(\gamma)} = \begin{bmatrix} \kappa_{22}^{(1,\gamma)} & \kappa_{21}^{(1,\gamma)} & 0 & 0 & . & 0 & 0 & 0 \\ \kappa_{12}^{(1,\gamma)} & \kappa_{11}^{(1,\gamma)} + \kappa_{22}^{(2,\gamma)} & \kappa_{21}^{(2,\gamma)} & 0 & . & 0 & 0 & 0 \\ 0 & \kappa_{12}^{(2,\gamma)} & \kappa_{11}^{(2,\gamma)} + \kappa_{22}^{(3,\gamma)} & \kappa_{21}^{(3,\gamma)} & . & 0 & 0 & 0 \\ 0 & 0 & . & . & . & 0 & 0 & 0 \\ 0 & 0 & 0 & . & . & . & 0 & 0 \\ 0 & 0 & 0 & 0 & . & . & . & 0 \\ 0 & 0 & 0 & 0 & . & \kappa_{12}^{(N_\beta-1,\gamma)} & \kappa_{11}^{(N_\beta-1,\gamma)} + \kappa_{22}^{(N_\beta,\gamma)} & \kappa_{21}^{(N_\beta,\gamma)} \\ 0 & 0 & 0 & 0 & . & 0 & \kappa_{12}^{(N_\beta,\gamma)} & \kappa_{11}^{(N_\beta,\gamma)} \end{bmatrix}$$

$$\gamma = 1, 2, ..., N_\gamma$$

The submatrix $\mathbf{B}_2^{(\gamma\beta)}$ used in the global thermal conductivity matrix assembly

$$\mathbf{B}_2^{(\gamma\beta)} = \begin{bmatrix} & \boldsymbol{\gamma} \rightarrow & \mathbf{1} & \mathbf{2} & . & . & \boldsymbol{\gamma}^{th}\mathbf{col.} & (\boldsymbol{\gamma}+\mathbf{1})^{th}\mathbf{col.} & . & . & \mathbf{N}_\gamma\mathbf{+1} \\ \boldsymbol{\beta} \downarrow & & & & & & & & & & \\ \mathbf{1} & & 0 & 0 & . & . & 0 & 0 & . & . & 0 \\ \mathbf{2} & & 0 & 0 & . & . & 0 & 0 & . & . & 0 \\ . & & . & . & . & . & . & . & . & . & . \\ . & & . & . & . & . & . & . & . & . & . \\ \boldsymbol{\beta}^{th}\mathbf{row} & & 0 & 0 & . & . & \kappa_{24}^{(\beta,\gamma)} & \kappa_{23}^{(\beta,\gamma)} & . & . & 0 \\ (\boldsymbol{\beta}+\mathbf{1})^{th}\mathbf{row} & & 0 & 0 & . & . & \kappa_{14}^{(\beta,\gamma)} & \kappa_{13}^{(\beta,\gamma)} & . & . & 0 \\ . & & . & . & . & . & . & . & . & . & . \\ . & & . & . & . & . & . & . & . & . & . \\ \mathbf{N}_\beta\mathbf{+1} & & 0 & 0 & . & . & 0 & 0 & . & . & 0 \end{bmatrix}$$

The submatrix $\mathbf{A}_{11}^{(\gamma)}$ used in the global stiffness matrix assembly

$$\mathbf{A}_{11}^{(\gamma)} = \begin{bmatrix} K_{22}^{(1,\gamma)} & 0 & 0 & 0 & . & 0 & 0 & 0 \\ K_{12}^{(1,\gamma)} & K_{11}^{(1,\gamma)} + K_{22}^{(2,\gamma)} & K_{21}^{(2,\gamma)} & 0 & . & 0 & 0 & 0 \\ 0 & K_{12}^{(2,\gamma)} & K_{11}^{(2,\gamma)} + K_{22}^{(3,\gamma)} & K_{21}^{(3,\gamma)} & . & 0 & 0 & 0 \\ 0 & 0 & . & . & . & 0 & 0 & 0 \\ 0 & 0 & 0 & . & . & . & 0 & 0 \\ 0 & 0 & 0 & 0 & . & . & . & 0 \\ 0 & 0 & 0 & 0 & . & K_{12}^{(N_\beta-1,\gamma)} & K_{11}^{(N_\beta-1,\gamma)} + K_{22}^{(N_\beta,\gamma)} & K_{21}^{(N_\beta,\gamma)} \\ 0 & 0 & 0 & 0 & . & 0 & K_{12}^{(N_\beta,\gamma)} & K_{11}^{(N_\beta,\gamma)} \end{bmatrix}$$

$$\gamma = 1, 2, ..., N_\gamma$$

The submatrix $\mathbf{B}_{13}^{(\gamma\beta)}$ used in the global stiffness matrix assembly

$$\mathbf{B}_{13}^{(\gamma\beta)} = \begin{bmatrix} & \boldsymbol{\gamma} \rightarrow & \mathbf{1} & \mathbf{2} & . & . & \boldsymbol{\gamma}^{th}\mathbf{col.} & (\boldsymbol{\gamma}+\mathbf{1})^{th}\mathbf{col.} & . & . & \mathbf{N}_\gamma\mathbf{+1} \\ \boldsymbol{\beta} \downarrow & & & & & & & & & & \\ \mathbf{1} & & 0 & 0 & . & . & 0 & 0 & . & . & 0 \\ \mathbf{2} & & 0 & 0 & . & . & 0 & 0 & . & . & 0 \\ . & & . & . & . & . & . & . & . & . & . \\ . & & . & . & . & . & . & . & . & . & . \\ \boldsymbol{\beta}^{th}\mathbf{row} & & 0 & 0 & . & . & K_{26}^{(\beta,\gamma)} & K_{25}^{(\beta,\gamma)} & . & . & 0 \\ (\boldsymbol{\beta}+\mathbf{1})^{th}\mathbf{row} & & 0 & 0 & . & . & K_{16}^{(\beta,\gamma)} & K_{15}^{(\beta,\gamma)} & . & . & 0 \\ . & & . & . & . & . & . & . & . & . & . \\ . & & . & . & . & . & . & . & . & . & . \\ \mathbf{N}_\beta\mathbf{+1} & & 0 & 0 & . & . & 0 & 0 & . & . & 0 \end{bmatrix}$$

8 References

Aboudi, J., (1991). Mechanics of Composite Materials: A Unified Micromechanical Approach, Elsevier, Amsterdam.

Aboudi, J., Pindera, M-J., and Arnold, S. M., (1993). Thermoelastic Response of Large-Diameter Fiber Metal Matrix Composites to Thermal Gradients, *NASA TM 106344*, NASA-Lewis Research Center, Cleveland, OH.

Aboudi, J., Pindera, M-J., and Arnold, S. M., (1996). Thermoelastic Theory For the Response of Materials Functionally Graded in Two Directions, *International Journal of Solids and Structures*, Vol. 33, No. 7, pp. 931-966.

Aboudi, J., Pindera, M-J., and Arnold, S. M., (1999). Higher-Order Theory for Functionally Graded Materials, *Composites Part B: Engineering*, Vol. 30, No. 8, pp. 777-832.

Delale, F. and Erdogan, F., (1983). The Crack Problem for a Non-Homogeneous Plane, ASME Journal of Applied Mechanics, Vol. 50, pp. 609-614.

Delfosse, D., Cherradi, N., and Ilschner, B., (1997). Numerical and Experimental Determination of Residual Stresses in Graded Materials, *Composites Part B: Engineering*, Vol. 28, No. 1-2, pp. 127-141.

Drake, J. T., Williamson, R. L., and Robin, B. H., (1993). Finite Element Analysis of Thermal Residual Stresses at Graded Ceramic-Metal Interfaces, *Journal of Applied Physics*, Vol. 74, No. 2, pp. 1321-1326.

Dugdale, D. S. and Ruiz, C., (1971). Elasticity for Engineers, McGraw-Hill, London.

Erdogan, F., (1985). The Crack Problem for Bonded Non-Homogeneous Materials under Anti-Plane Shear Loading, *Journal of Applied Mechanics*, Vol. 52, pp. 823-828.

Erdogan, F., Kaya, A. C., and Joseph, P. F., (1991). The Crack Problem in Bonded Non-Homogeneous Materials, *Journal of Applied Mechanics*, Vol. 58, No. 2, pp. 410-418.

Erdogan, F., (1995). Fracture Mechanics of Functionally Graded Materials, *Composites Engineering*, Vol. 5, No. 7, pp. 753-770.

Erdogan, F. and Wu, B. H., (1996). Crack Problems in FGM Layers under Thermal Stresses, *Journal of Thermal Stresses*, Vol. 19, No. 3, pp. 237-265.

Horgan, C. O. and Chan, A. M., (1998). Torsion of Functionally Graded Isotropic Linearly Elastic Bars, *Journal of Elasticity*, Vol. 52, No. 2, pp. 181-199.

Horgan, C. O. and Chan, A. M., (1999). The Pressurized Hollow Cylinder or Disk Problem for Functionally Graded Isotropic Linearly Elastic Materials, *Journal of Elasticity*, Vol. 55, No. 1, pp. 43-59.

Horgan, C. O. and Chan, A. M., (1999). The Stress Response of Functionally Graded Isotropic Linearly Elastic Rotating Disks, *Journal of Elasticity*, Vol. 55, No. 3, pp. 219-230.

IIschner, B. and Cherradi, N., (1994). Proceedings of the 3^{rd} International Symposium on Structural and Functional Gradient Materials*, Presses Polytechniques et Universitaires Romandes.*

Jeon, S. P., Tanigawa, Y., and Sone, D., (1997). Analytical Treatment of Axisymmetrical Thermoelastic Field with Kassir's Non-Homogeneous Material Properties and its Adaptation to Boundary Value Problem of Slab Under Steady Temperature Field, *Journal of Thermal Stresses*, Vol. 20, No. 3-4, pp. 325-343.

Jian, C. Y., Hashida, T., Takahashi, H., and Saito, M., (1995). Thermal Shock and Fatigue Resistance Evaluation of Functionally Graded Coating for Gas Turbine Blades by Laser Heating Method, *Composites Engineering*, Vol. 5, No. 7, pp. 879-889.

Jin, Z. H. and Paulino, G. H., (2001). Transient Thermal Stress Analysis of an Edge Crack in a Functionally Graded Material, *International Journal of Fracture*, Vol. 107, No. 1, pp. 73-98.

Kadioglu, S. and Erdogan, F., (1995). The Free-End Interface Crack Problem for Bonded Orthotropic Layers, *International Journal of Engineering Science*, Vol. 33, No. 8, pp. 1105-1120.

Kokini, K. and Choules, B. B., (1995). Surface Thermal Fracture of Functionally Graded Ceramic Coatings-Effect of Architecture and Materials, *Composites Engineering*, Vol. 5, No. 7, pp. 865-877.

Lee, Y-D. and Erdogan, F., (1998). Interface Cracking of FGM Coatings Under Steady-State Heat Flow, *Engineering Fracture Mechanics*, Vol. 59, No. 3, pp. 361-380.

Nadeau, J. C. and Ferrari, M., (1999). Microstructural Optimization of a Functionally Graded Transversely Isotropic Layer, *Mechanics of Materials*, Vol. 31, No. 10, pp. 637-651.

Needleman, A. and Suresh S. (1996). Mechanics and Physics of Layered and Graded Materials, *Journal of the Mechanics and Physics of Solids*, Vol. 44, No. 5, pp. 647-821.

Noda, N., (1999). Thermal Stresses in Functionally Graded Materials, *Journal of Thermal Stresses*, Vol. 24, No. 4-5, pp. 477-512.

Noda, N. and Jin, Z. H., (1993). Thermal-Stress Intensity Factors for a Crack in a Strip of a Functionally Gradient Material, *International Journal of Solids and Structures*, Vol. 30, No. 8, pp. 1039-1056.

Ootao, Y., Tanigawa, Y., and Nakamura, T., (1998). Optimization of Material Composition of FGM Hollow Circular Cylinder under Thermal Loading: A Neural Network Approach, *Composites Part B: Engineering*, Vol. 30, No. 4, pp. 415-422.

Paulino, G. H. and Jin, Z. H., (2001). Viscoelastic Functionally Graded Materials Subjected to Antiplane Shear Fracture, *Journal of Applied Mechanics*, Vol. 68, No. 2, pp. 284-293.

Pindera, M-J., (1991). Local/Global Stiffness Matrix Formulation for Composite Materials and Structures, *Composites Engineering*, Vol. 1, No. 2, pp. 69-83.

Pindera, M-J., Freed, A. D., and Arnold, S. M., (1993). Effects of Fiber and Interfacial Layer Morphologies on the Thermoplastic Response of Metal Matrix Composites, *International Journal of Solids and Structures*, Vol. 30, No. 9, pp. 1213-1238.

Pindera, M-J., Arnold, S. M., Aboudi, J., and Hui, D. (Eds.), (1994a). Use of Composites Functionally Graded Materials, *Composites Engineering*, Vol. 4, No. 1, pp. 1-145.

Pindera, M-J., Aboudi, J., and Arnold, S. M., (1994b). Thermo-Inelastic Analysis of Functionally Graded Materials: Inapplicability of the Classical Micromechancis Approach, *Inelasticity and Micromechanics of Metal Matrix Composites,* G. Z. Voyiadjis and J. W. Ju (Eds.), pp. 273-305, Elsevier Science Publishers B. V., The Netherlands.

Pindera, M-J., Aboudi, J., Arnold, S. M., and Jones, W. F. (Eds.), (1995a). Use of Composites in Multi-Phased and Functionally Graded Materials, *Composites Engineering*, Vol. 5, No. 7, pp. 743-974.

Pindera, M-J., Aboudi, J., and Arnold, S. M., (1995b). Recent Advances in the Mechanics of Functionally Graded Composites, *Aerospace Thermal Structures and Materials for a New Era*, (Progress in Astronautics and AeroNautics, Vol. 168), E. A. Thornton (Ed.), pp. 181-203, American Institute of Aeronautics and Astronautics, Inc., Washington, DC.

Pindera, M-J., Aboudi, J., and Arnold, S. M., (1995c). Limitations of the Uncoupled, RVE-based Micromechanical Approach in the Analysis of Functionally Graded Composites, *Mechanics of Materials*, Vol. 20, No. 1, pp. 77-94.

Pindera, M-J., Aboudi, J., Glaeser, A. M., and Arnold, S. M. (Eds.), (1997). Use of Composites in Multi-Phased and Functionally Graded Materials, *Composites Part B: Engineering*, Vol. 28, No. 1/2, pp. 1-175.

Pindera, M-J. and Dunn, P., (1997). Evaluation of the Higher-Order Theory for Functionally Graded Materials via the Finite-Element Method, *Composites Part B: Engineering*, Vol. 28, No. 1/2, pp. 109-119.

Pindera, M-J., Aboudi, J., and Arnold, S. M., (1998). Higher-Order Theory for the Analysis of Functionally Graded Materials, *Advanced Multilayered and Fiber-Reinforced Composites*, Y. M. Haddad (Ed.), pp. 111-132, Kluwer Academic Publishers, The Netherlands.

Pindera, M-J. and Aboudi, J., (2000). A Coupled Higher-Order Theory for Cylindrical Structural Components with Bi-Directionally Graded Microstructures, *NASA Contractor Report 210350*, NASA-Glenn Research Center, Cleveland, OH.

Salzar, R. S. and Barton, F. W., (1994). Residual Stress Optimization in Metal-Matrix Composites using Discretely Graded Interfaces, *Composites Engineering*, Vol. 4, No. 1, pp. 115–128.

Schulze, G. W. and Erdogan, F., (1998). Periodic Cracking of Elastic Coatings, *International Journal of Solids and Structures*, Vol. 35, No. 28-29, pp. 3615-3634.

Shiota, I. and Miyamoto, Y. (Eds.), (1997). Functionally Graded Materials 1996 (Proceedings of the 4^{th} International Symposium on Functionally Graded Materials), Elsevier, Amsterdam.

Suresh, S., Giannakopoulos, A. E., and Olsson, M. (1994). Elastoplastic Analysis of Thermal Cycling-Layered Materials with Sharp Interfaces, *Journal of the Mechanics and Physics of Solids*, Vol. 42, No. 6, pp. 979-1018.

Suresh, S. and Mortensen A., (1998). Fundamentals of Functionally Graded Materials, *2^{nd} edition*, Cambridge University Press.

Suresh, S., (2001). Graded Materials for Resistance to Contact Deformation and Damage, *Science 292*, pp. 2447-2451.

Sutradhar, A., Paulino, G. H., and Gray, L. J., (2001). Transient Heat Conduction in Homogeneous and Non-Homogeneous Materials by the Laplace Transform Galerkin Boundary Element Method, *Engineering Analysis with Boundary Elements*, Vol. 26, No. 2, pp. 119-132.

Williamson, R. L., Rabin, B. H., and Drake, J. T., (1993). Finite Element Analysis of Thermal Residual Stresses at Graded Ceramic-Metal Interfaces. Part 1. Model Description and Geometrical Effects, *Journal of Applied Physics*, Vol. 74, No. 2, pp. 1310-1320.

Zhong, Yi., (2002). Efficient Reformulation of HOTFGM-Heat Conduction Case with Variable Thermal Conductivity, *M. S. Thesis, University of Virginia,* Charlottesville, Virginia.

REPORT DOCUMENTATION PAGE

Form Approved
OMB No. 0704-0188

1. AGENCY USE ONLY (*Leave blank*)	2. REPORT DATE	3. REPORT TYPE AND DATES COVERED
	November 2002	Final Contractor Report

4. TITLE AND SUBTITLE

Efficient Reformulation of the Thermoelastic Higher-Order Theory for FGMs

5. FUNDING NUMBERS

WU–708–73–35–00
NAG3–2524

6. AUTHOR(S)

Yogesh Bansal and Marek-Jerzy Pindera

7. PERFORMING ORGANIZATION NAME(S) AND ADDRESS(ES)

University of Virginia
0 Mccormick Road
Charlottesville, Virginia 22904–2000

8. PERFORMING ORGANIZATION REPORT NUMBER

E–13599

9. SPONSORING/MONITORING AGENCY NAME(S) AND ADDRESS(ES)

National Aeronautics and Space Administration
Washington, DC 20546–0001

10. SPONSORING/MONITORING AGENCY REPORT NUMBER

NASA CR—2002-211909

11. SUPPLEMENTARY NOTES

Yogesh Bansal and Marek-Jerzy Pindera, University of Virginia, 0 Mccormick Road, Charlottesville, Virginia 22904–2000. Project Manager, Steven M. Arnold, Structures and Acoustics Division, NASA Glenn Research Center, organization code 5920, 216–433–3334.

12a. DISTRIBUTION/AVAILABILITY STATEMENT

Unclassified - Unlimited
Subject Categories: 24 and 39 Distribution: Nonstandard

Available electronically at http://gltrs.grc.nasa.gov

This publication is available from the NASA Center for AeroSpace Information, 301–621–0390.

12b. DISTRIBUTION CODE

13. ABSTRACT ***(Maximum 200 words)***

Functionally graded materials (FGMs) are characterized by spatially variable microstructures which are introduced to satisfy given performance requirements. The microstructural gradation gives rise to continuously or discretely changing material properties which complicate FGM analysis. Various techniques have been developed during the past several decades for analyzing traditional composites and many of these have been adapted for the analysis of FGMs. The higher-order theory for functionally graded materials (HOTFGM) is a coupled approach which takes the effect of microstructural gradation into consideration and does not ignore the local-global interaction of the spatially variable inclusion phase(s) as do traditional uncoupled approaches. Despite its demonstrated utility, however, the original formulation of the higher-order theory is computationally intensive. Herein, an efficient reformulation of the original higher-order theory for two-dimensional elastic problems is developed and validated. The use of the local-global conductivity and local-global stiffness matrix approach is made in order to reduce the number of equations involved. The reformulation decreases the size of the global conductivity and stiffness matrices by approximately sixty percent. Results illustrate the efficiency of the reformulation and its advantages in analyzing functionally graded materials.

14. SUBJECT TERMS

Micromechanics; Elastic; Thermal; Deformation; Composites; Analaysis

15. NUMBER OF PAGES

83

16. PRICE CODE

17. SECURITY CLASSIFICATION OF REPORT	18. SECURITY CLASSIFICATION OF THIS PAGE	19. SECURITY CLASSIFICATION OF ABSTRACT	20. LIMITATION OF ABSTRACT
Unclassified	Unclassified	Unclassified	